TACTILE AND MULTISPECTRAL BIMODAL IMAGING FOR BREAST CANCER RISK ASSESSMENT

A Dissertation Proposal
Submitted to
the Temple University Graduate Board

---

in Partial Fulfillment
of the Requirements for the Degree of
DOCTOR OF PHILOSOPHY
in ELECTRICAL ENGINEERING

---

by
Vira Oleksyuk
May, 2020

Examining Committee Members:

Dr. Chang-hee Won, Advisory Chair, Electrical and Computer Engineering Department
Dr. Joseph Picone, Electrical and Computer Engineering Department
Dr. Iyad Obeid, Electrical and Computer Engineering Department
Dr. Nancy Pleshko, Bioengineering Department

ABSTRACT

American Cancer Society estimates that in 2020 30% of all new female cancer diagnoses in the United States will be breast cancer. While many women have access to healthcare and cancer screening, women from rural or underdeveloped communities often have limited access. There is a need for an inexpensive and easy-to-use breast cancer identification device, which can be employed in small clinics to provide support to the primary care physicians.

This work aims to develop a method for a breast tumor and tissue characterization using non-invasive tactile and multispectral imaging.

The proposed bimodal imaging system has tactile and multispectral imaging capabilities. Tactile modality characterizes tumors by estimating their size, stiffness, depth, and the tactile imaging index. Multispectral imaging modality identifies the breast tissue color, texture, area, asymmetry, and the multispectral imaging index. The indexes are finally combined into the malignancy risk score for the patient.

In this study, we will describe the development of the bimodal imaging system. We will present the algorithms from tactile and multispectral modalities. We will show the development of Tactile and Multispectral Profile Diagrams as a method to present imaging signals. A Tactile Profile Diagram is a pictorial representation of relative stiffness and size of an imaged tumor. A Multispectral Profile Diagram is a representative pattern image for superficial optical properties of breast tissue. The Convolutional Neural Network will be employed to classify the profile diagrams. We will describe the preliminary results for the experiments conducted using tissue mimicking phantoms, as well as human *in-vivo* experiments. The malignancy risk score will be calculated and analyzed. The preliminary results demonstrate the ability of the method to quantify tumor and tissue properties accurately.

TABLE OF CONTENTS

LIST OF FIGURES

LIST OF TABLES

CHAPTER 1

INTRODUCTION

In the first chapter, we outline the contributions of the proposed dissertation work with the research goal statement. Next, we list the peer-reviewed publications to date. Finally, we present an outline of the dissertation proposal document.

1.1 Contributions

There are eight main contributions of the proposed dissertation work.

- The combination of tactile imaging and multispectral imaging is proposed to aid doctors in breast cancer diagnostic decisions.
- A bimodal breast tissue and tumor phantom design is described. The custom phantom mimics the mechanical and optical properties of breast tissue. The mechanical properties phantom was fabricated and tested. The optical properties phantom is under development.
- A novel method to analyze tactile imaging data by constructing Tactile Profile Diagrams from sets of tactile images is developed.
- Convolutional Neural Network classification models are built to extract information about tumors' depth, size, and stiffness from Tactile Profile Diagrams. The models' improvements have to be implemented.
- A novel method to analyze multispectral imaging data by constructing Multispectral Profile Diagrams from sets of multispectral images is outlined.
- Convolutional Neural Network classification models are proposed to gather information about affected breast tissue color, area, texture, and asymmetry from Multispectral Profile Diagrams. The work on the model development has to be done.

- A method to combine mechanical and optical properties estimations from the dual modality imaging with additional patient's health information into a single individualized Malignancy Risk Score is proposed.

- Preliminary evaluations of the methods completed on a custom made breast tissue mimicking phantom, and in a pilot *in-vivo* study. Additional evaluations have to be completed.

1.2 Research Goal

The primary goal of this research is to develop a bimodal imaging system for quantitative breast tumor and tissue characterization. The two proposed modes of the imaging system are tactile imaging and multispectral imaging. Tactile Imaging Probe's hardware and software, as well as its algorithms, will be developed to measure tactile properties, such as the tumor size, stiffness, and depth within the breast tissue. Multispectral Imaging Probe will be developed to characterize superficial breast tissues properties, such as color, texture, size of the affected area, and asymmetry changes. Finally, we will propose a method for breast tumor classification on malignant or benign using characterization indexes obtained from the two imaging modalities and the patient's health information.

1.3 Peer-reviewed Publications

Here is the list of peer-reviewed publications:

1. V. Oleksyuk, R. Rajan, F. Saleheen, D. Caroline, S. Pascarella and C.-H. Won, "Risk score based pre-screening of breast tumor using compression induced sensing system," *Sensors Journal*, IEEE, Vol.18 (10), pp. 4038-4045, 2018.

2. F. Saleheen, V. Oleksyuk, and C.-H.Won, "Itchy skin region detection using hyperspectral imaging," Proc. SPIE Defense-Commercial Sensing, Paper 10656-7, Baltimore, MD: USA, 2018.

3. V. Oleksyuk, F. Saleheen, D. Caroline, S. Pascarella and C.-H. Won, "Classification of breast masses using tactile imaging system and machine learning algorithms," IEEE Signal Processing in Medicine and Biology Symposium, Philadelphia, PA: USA, Jan 2017.

4. V. Oleksyuk, F. Saleheen, D. Caroline, S. Pascarella, C.-H. Won. "KNN classification of tactile imaging data," 2017 International Symposium on Innovation in Information Technology and Application (ISIITA17), Danang: Vietnam, Jan. 2017.

5. C.-H. Won, J. Goldstein, V. Oleksyuk, D. Caroline, S. Pascarella. "Tumor size and elasticity estimation using smartphone-based compression-induced scope," 39th Annual International Conference of the IEEE Engineering in Medicine and Biology Society (EMBC 17), JeJu Island: S. Korea, July 2017, pp. 4106-4109.

6. F. Saleheen, Z. Wang, W. Moser, V. Oleksyuk, J. Picone, C.-H. Won, "Effectiveness of virtual open laboratory teaching assistant for circuits laboratory," 123rd ASEE Annual Conference, New Orleans, LA: USA, June 2016.

7. V. Oleksyuk, F. Saleheen, W. Moser, and C.-H. Won, "Tactile imaging sensor for mechanical properties quantification of breast tumor," IEEE Biomedical Circuits and Systems Conference (BioCAS), Atlanta, GA: USA, Oct. 2015.

8. A. Sahu, F. Saleheen, V. Oleksyuk, C. McGoverin, N. Pleshko, A. Harati, J. Picone and C.-H. Won, "Characterization of Mammary Tumors Using Noninvasive Tactile and Hyperspectral Imaging Sensors," *Sensors Journal*, IEEE, Vol.14 (10), pp. 3337-3344, 2014.

9. A. Sahu, F. Saleheen, V. Oleksyuk, Y. Chen, and C.-H. Won, "Tactile and hyperspectral imaging sensors for mammary tumor characterization," Sensors, 2013 IEEE, Baltimore, MD: USA, Nov 2013.

10. F. Saleheen, V. Oleksyuk, A. Sahu, and C.-H. Won, "Non-invasive mechanical properties estimation of embedded objects using tactile imaging sensor," Proc. SPIE 8719, Smart Biomedical and Physiological Sensor Technology X, Baltimore, MD: USA, May 2013.

11. F. Saleheen, A. Sahu, V. Oleksyuk, and C.-H. Won, "Normal force estimation using tactile imaging sensor," Bioengineering Conference (NEBEC), 2012 38th Annual Northeast, Philadelphia, PA: USA, Mar. 2012, pp. 119-120.

1.4 Dissertation Proposal Outline

This dissertation proposal consists of ten chapters.

Chapter 2 presents the background information on normal and abnormal breast physiology. The chapter also gives a review of current breast cancer screening techniques and the general overview of tactile and multispectral imaging.

Chapter 3 describes the Tactile Imaging Probe. The hardware design and acquisition software are presented in details. Then we explain size and stiffness estimation algorithms designed to work on sets of tactile images. Following, we present the automatic data pre-processing software. Next, we propose the development of the Tactile Profile Diagrams as a method to capture the dynamic properties of the signal. Finally, algorithms for tumor depth, size, and stiffness estimation using Tactile Profile Diagrams are explained.

Chapter 4 presents the multispectral imaging modality overview. We present the hardware design and the acquisition software. Then, we describe the image pre-processing techniques to improve data quality. Later, we propose the method for the Multispectral Profile Diagram development and the optical properties estimation from the diagrams.

Chapter 5 gives an overview of different types of classification methods. Then, we propose the Convolutional Neural Network model architectures for classification of Tactile and Multispectral Profile Diagrams.

Chapter 6 outlines the method for Malignancy Risk Score calculation based on the tactile index, multispectral index, and the patient's personal data.

Chapter 7 presents the results from the Tactile Imaging Probe experiments conducted using silicone breast tissue mimicking phantom, and during an in-vivo pilot study.

Chapter 8 shows the preliminary results from the Multispectral Imaging Probe experiments. The design of a bimodal tissue mimicking phantom is proposed.

Chapter 9 presents conclusions and future research work.

CHAPTER 2

BACKGROUND

In this chapter, we review human breast physiology, breast diseases, and breast cancer screening techniques and tools to highlight the need for our research work. We also outline the tactile imaging and multispectral imaging in biomedical applications.

2.1 Breast Diseases

There is a broad spectrum of breast diseases, some of which are benign, and some are malignant or cancerous. Depending on the diagnosis, a patient gets a specific procedure and treatment plan to follow (Hellawell, 2008). To understand breast cancer, it is important to know breast anatomy and physiology.

2.1.1 Normal Breast Physiology

The breast consists of multiple tissues with structural and supportive functions (Aydiner et al., 2017). Fig. 2.1 shows the breast composition. The main components of the breast are skin, superficial fascia, and breast parenchyma. Skin is the protective layer that is covering the breast. The deep layer of skin, dermis, merges with the superficial fascia, which in turn transitions to the breast parenchyma. The breast parenchyma consists of several tissues, such as fibrous stroma, glandular epithelium, fat, and supporting structures (Aydiner et al., 2017). The parenchyma is built of segments called lobes in a radial arrangement. The lobes divided onto smaller structures, lobules, and milk collecting ducts converging within the nipple region (Harris et al., 2014; Aydiner et al., 2017). The breast undergoes physiological changes over a lifespan, causing the change in the breast composition. For example, the proportion of glandular tissue to fat tissue decreases with age (Aydiner et al., 2017), and it lowers the density of the breasts.

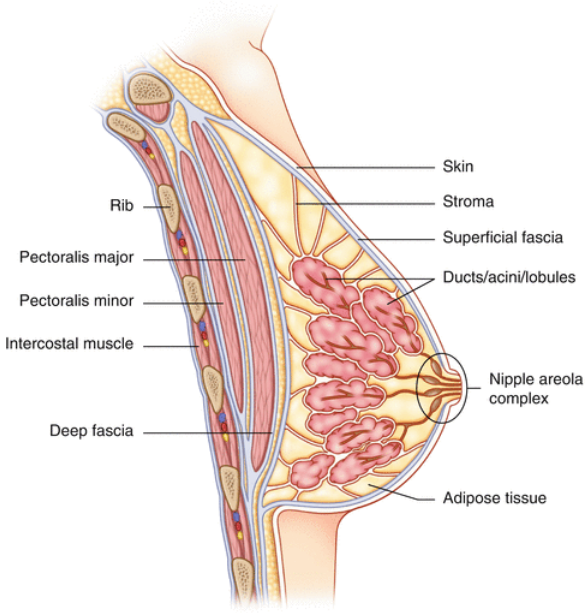

Figure 2.1: Breast anatomy

2.1.2 Benign Breast Diseases

Benign breast diseases are breast diseases that cause pain with or without masses or nipple discharge. The vast majority of women (90%), who require attention from a health care specialist, have benign conditions (GP, 2015).

There are several main causes of benign breast conditions: fibrocystic breast disease, benign breast tumors, and breast inflammation or mastitis (Hellawell, 2008). The benign conditions are not cancerous by definition, yet they may elevate chances for patients to develop breast cancer in the future. Doctors use a detailed patient's health history review and a careful examination to diagnose a breast disease (Hellawell, 2008).

Fibrocystic breast disease caused by hormonal changes. The breast feels lumpy and painful. The lumps are the fluid-filled lobules, which are also called cysts. They are more common in younger women (GP, 2015). More than half of all pre-menopausal women going through Fibrocystic change (Hellawell, 2008).

Benign breast masses are mostly caused by fibroadenoma (Hellawell, 2008). The lumps are composed of fibrous and epithelial tissues and are very mobile during a breast examination (GP, 2015).

Mastitis is an infection of breast tissues, which is common for lactating women, and women with large breasts. Mastitis manifestations are pain, fever, swelling, none, single or multiple breast masses, and an abscess-like inflammation (Aydiner et al., 2017). Doctors should exclude the possibility of inflammatory carcinoma in patients with mastitis-like symptoms (Harris et al., 2014).

2.1.3 Malignant Breast Diseases

Many different malignant or cancerous breast diseases are known. Their ability to invade surrounding tissues differentiates them from benign conditions. The type of cancer and the time of the diagnosis define the disease manifestations for each patient. Possible symptoms of breast cancer include a sudden breast mass development, discharge, breast skin color or texture changes, nipple shape changes, or itch development (Hellawell, 2008).

The most common cancerous breast tumors are invasive ductal and lobular adenocarcinomas, which are cancers of ductal or lobular glandular tissues, respectively (Hellawell, 2008).

Ductal carcinoma in situ and lobular carcinoma in situ are the conditions, where tumors did not cross the inner membranes and invade other surrounding tissues. These conditions carry an increased risk for a patient to develop cancer (Hellawell, 2008).

Inflammatory breast cancer (IBC) is rare (about 2% of breast cancers) but a very aggressive type of cancer. It presents symptoms very similar to mastitis; however, in IBC patients, the area of the affected reddened skin usually involves the entire breast, with no tenderness and fever (Harris et al., 2014).

2.2 Breast Disease Management

Breast masses are the most common breast disease manifestation, where the majority of them being benign (Harris et al., 2014). Breast masses can be detected by patients during self breast examination (SBE), by medical practitioners during a clinical breast examination (CBE), or during a routine screening mammogram (Hellawell, 2008). In modern practice, SBE and CBE are not the primary tools for a cancer diagnosis; however, they are very im-

portant supplemental screening techniques to mammography, ultrasound, or MRI imaging. CBE is used to identify the affected tissues, and even to find 15% of the malignant tumors undetected during mammography (Aydiner et al., 2017).

Regular breast cancer screenings are recommended for asymptotic women (Harris et al., 2014). Women with increased risk for developing breast cancer should follow a more frequent evaluation procedure schedule than the one developed for the regular public (Hellawell, 2008). The patient's health history plays a role in breast cancer risk assessment. The American Cancer Society specifies many types of the well-established breast cancer risk factors, which are the advance age, family history of breast cancer, the inheritance of some gene mutations, dense breast tissue, a benign breast condition, early menarche, late menopause age, chest radiation, unhealthy weight, alcohol consumption, no physical activity, no children, not breastfeeding, hormonal therapy, hormonal birth control, and breast implants (American Cancer Society,). The National Institute of Health developed an interactive online tool for breast cancer risk assessment based on the Gail model, which can be used by patients and clinicians (National Cancer Institute, 1999).

When a tumor is found, physicians complete a detailed assessment of the tumor and the affected breast, evaluate for the possibility of malignancy, and aim to give an accurate diagnosis (Harris et al., 2014). To do so, most often, they use mammography and ultrasound imaging to visualize the breast tissues and suspicious masses. Mammography helps to detect microcalcifications, commonly caused by cancer. Ultrasound technology aids in identifying cysts. The patients with cysts usually do not need further evaluations, yet the patients with solid masses are scheduled to undergo biopsy procedure and to exclude the possibility of malignancy. Other supplemental tests are available to support the diagnosis (Hellawell, 2008).

To date, there are many prognostic factors identified for breast cancer patients. However, the most significant of them are the presence and the amount of metastasis in axillary lymph nodes and the tumor size. These two factors are used to stage the tumor, and therefore, are the once which define the treatment plan for the patient. The more metastatic lymph nodes are found, and the larger tumor is, the more ominous survival prognosis is given to the patient by doctors. (Aydiner et al., 2017).

2.3 Breast Imaging Techniques

Multiple imaging technologies are developed for breast cancer screening purposes, such as screening mammography, ultrasound, magnetic resonance imaging, computer tomography, ultrasound elastography, thermography, optical imaging, and others (Harris et al., 2014; Yin-Kwee Ng, 2011). The goal for screening is to detect the disease early and to give the best chance of survival and cure to the patient. Positive screening result follows by additional tests to confirm malignancy (Harris et al., 2014).

Here we provide a brief overview of different breast imaging modalities.

Mammography

Mammography is a gold standard method for breast cancer screening (Harris et al., 2014; Yin-Kwee Ng, 2011). It relies on low-dose X-rays to image the breast, which is placed between a source and detector plates. Microcalcification in the breast, which can be an indicator of malignancy, look brighter on the mammogram, whereas the breast tissues look darker. However, it is challenging to detect early-stage malignancy, especially in women with dense breasts. Therefore, additional screening tests are used as supplements to obtain better results for cancer detection. Recently, a digital 3D mammography developed to better characterize breast tissues. The modality uses the functional principles of mammography yet is modified to acquire three-dimensional views of the breast.

Computer-aided detection (CAD) is a set of machine learning algorithms developed to support doctors with the identification of small tumors, which now become a standard feature in modern mammography machines. Besides all of its advantages, CAD is associated with a high false positive rate and may mislead radiologists (Yin-Kwee Ng, 2011).

Ultrasound

Ultrasound (US) is a first choice for the supplemental to mammography diagnostic modality and can also be used as a stand-alone test in some cases. It is used to image patients, which had not conclusive result from mammogram due to high breast density or other factors (Harris et al., 2014)

The US method uses high frequency sound waves to image the tissues. A US transducer sends and senses the reflected inside the tissue waves to construct the ultrasound image.

The images are generated in real-time, while the transducer is moved over the region. The cons of the method are the high rate of false positive and false negative during screening.

One of the notable advancements in US technology is the development of ultrasound breast elastography, which can characterize tissue elasticity. There are two types of US elastography: free-hand elastography and shear wave elastography. The first relays on the light compression of the transducer on the tissue during acquisition, which creates a displacement field for strain estimation. The second method relays on the generated additional shear waves in transducers, which are used for strain estimation as well. Stiffness information is displayed as a range of colors, and the elastography image superimposed over the corresponding US image (Ricci et al., 2014). The method is under development.

Magnetic Resonance Imaging

Magnetic resonance imaging (MRI) uses a single proton (a hydrogen nucleus) to image tissues. It is possible because different tissue types are composed of molecules with different amounts of hydrogen nuclei. MRI is using the magnetic properties of the nuclei to analyze the tissues. The patient is placed in a magnetic field, and then radio frequency waves are applied to acquire an image sequence.

The pros of the method include high contrast of the images, no radiation concerns to patients, the ability to image both breasts together, and the ability to image dense breasts efĭňĄciently. The cons of the method are the high cost of the imaging (Harris et al., 2014), high false-positive rate, and microcalcifications that may not be shown correctly on images (Yin-Kwee Ng, 2011).

Positron Emission Tomography

Positron emission tomography (PET) is a nuclear medicine imaging technique, which uses gamma rays to image tissues and visualize their functional characteristics. To distinguish benign from malignant tumor images, PET modality uses the differences in levels of glucose metabolism. The relatively higher level of metabolism in the tissue will indicate malignancy.

PET is a useful supplemental method for detecting and staging breast cancer. It also can be coupled with MRI and mammography to overcome the issue with breast density and the menopausal status of a woman. There are also negative aspects of the method. The

PET experiment cost is high, the resolution of the images is low, and patients are exposed to radiation (Yin-Kwee Ng, 2011).

Thermography

Thermography imaging of the breast sometimes also called the digital infrared imaging. It is designed to use the infrared light spectrum for breast cancer detection (Harris et al., 2014). Cancerous and pre-cancerous tissues characterized by increased growth and higher metabolism than surrounding normal tissues. When the tissue becomes cancerous, it starts to draw more blood supply. These changes are causing the increased temperature in the affected areas, which can be detected by thermography. Thermography is a promising screening modality; however, its performance suffers from high sensitivity to the test conditions, and the image interpretation difficulties (Yin-Kwee Ng, 2011).

Diffuse Optical Imaging

Diffuse Optical Imaging (DOI) uses the near infrared wavelength band (650 nm - 1000 nm) to find tumors within a breast. The two types of DOI: the diffuse optical tomography and the diffuse optical mammography use the same principle yet different wavelengths for the imaging. The pros of the method are that it is non-invasive and not ionizing. It can give a quantitative assessment of the imaged tissues for hemoglobin saturation and concentration. The cons of the method are the difficulty to accurately measure biochemical components, to reconstruct an image, and the use of contrast mechanisms (Yin-Kwee Ng, 2011).

Electrical Impedance-based Imaging

The human body is a collection of tissues with different permeability properties. Research shows that cancerous tissues have lower impedance than the normal tissues (Yin-Kwee Ng, 2011). Two imaging methods are developed based on that property: the electrical impedance tomography (EIT), and the electrical impedance scanning (EIS). Multiple electrodes are placed on the breast to detect the impedance level samples, and then images are reconstructed from the values and analyzed (Yin-Kwee Ng, 2011).

Computer Tomography

Computer tomography (CT) uses X-rays to capture planar images or slices of the body. CT algorithms can recreate three-dimensional images from the taken slices, which can help to localize the tumor. The modality requires to use the intravenous iodine contrast agent.

The combination of CT imaging with PET is used to define the stage for metastatic cancers because it is able to assess the location of the tumor and the metabolism level of it (Yin-Kwee Ng, 2011). The method has multiple advantages with high quality of anatomical details visualization, yet uses 70 times higher level of ionizing radiation than a chest x-ray to complete a test (Harvard Medical School, 2010).

2.4 Discussion

Detailed overview of the breast physiology and the common manifestations of benign and malignant breast diseases are given in this chapter. Next, the breast disease management strategies are outlined. Finally, we gave the list and a short description of the available breast cancer imaging modalities.

Despite all of the advancement in imaging technology, no diagnosis rely purely on a single method. Very often, doctors use multiple imaging techniques in combination with pathological tests to find and to stage cancer. There is a need for an accessible and informative tool for medical professionals to quantify breast tumor and tissue properties.

CHAPTER 3

TACTILE IMAGING PROBE

In this chapter, we introduce the Tactile Imaging Probe (TIP) for breast tumor characterization, its principle, and hardware design. We will also describe the acquisition software and its capabilities. Next, we outline the algorithm and the graphical user interface for the size and stiffness estimation. Following, we describe the method to capture the dynamic properties of the tissue under compression by constructing Tactile Profile Diagrams from the sets of tactile images. We describe the method to estimate size and stiffness of the embedded tumors directly from Tactile Profile Diagrams.

3.1 Tactile Imaging Modality

Research shows that cancerous masses tend to be stiffer than benign ones (Krouskop et al., 1998; Wellman et al., 2001), and in some studies, malignant tumors are found to be tenfold stiffer than normal breast tissue through compression experiments (Price et al., 2010). It is also shown, that mechanical imaging can help in the classification of breast tumors on benign or malignant (Egorov et al., 2009). Moreover, the size of the detected tumor defines its grade during diagnosis, and defines the future treatment plan for the patient (Aydiner et al., 2017).

We developed the Tactile Imaging Probe (TIP) and its algorithms to mimic human touch sensation and to non-invasively measure the size and stiffness of embedded tumors. We also introduced the malignant/benign classification method to support doctors.

Tactile imaging modality is an inexpensive, non-invasive, and non-ionizing method for breast tumors characterization. This method provides information about the tumor's mechanical properties for pre-screening purposes.

3.2 Sensing Principle and Hardware Design

The Tactile Imaging Probe (TIP) is designed to mimic human touch sensation. From tactile images, TIP algorithms quantify the size and stiffness of the imaged tissues and tumors.

Fig. 3.1 shows sensing principle and hardware design of Tactile Imaging Probe. TIP uses a transparent and highly flexible polymer as a sensing element, which we fabricate from Polydimethyl siloxane (PDMS) two-compound material. We insert visible light to scatter within the sensing element using four light emitting diodes (LEDs) and the principle of total internal reflection (Lee and Won, 2013). When the sensing element is compressed against tissue with a tumor, its contact surface is deformed. This deformation causes the scattered within the polymer light to escape and to be captured by the lens-camera unit. We use a UI-3240CP-NIR monochrome CMOS Camera (IDS Imaging Development Systems GmbH, Obersulm, Germany), and a 5 Megapixel 12 mm lens (Schneider, Rhineland-Palatinate, Germany). The size of a tactile image is 1024 pixel $\times$ 1280 pixel. The depth of the pixel is 8 bit, which makes the pixel value range from 0 to 255. The image acquisition rate is 20 images per second (IDS Imaging Development Systems GmbH, 2015).

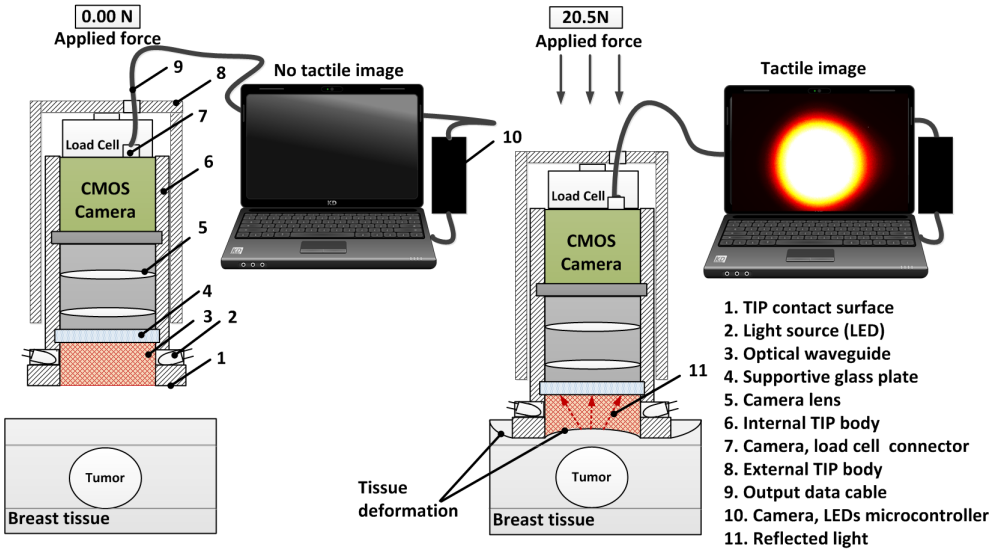

Figure 3.1: TIP Principle and Hardware Design

The compression force is measured with a FC22 Force Sensor (TE Connectivity, USA), attached on top of the camera body. The typical number of images in one acquisition

session is 50. The controller unit consists of a microcontroller (SparkFun Pro Micro 5V/16 MHz, SparkFun Electronics, Niwot, Colorado, USA) and its circuitry to manage brightness of the LEDs, as well as, the force-camera synchronization. Fig. 3.2 shows the design of the controller circuit. The controller circuit locates outside of the TIP main body to decrease the weight of the hand held probe.

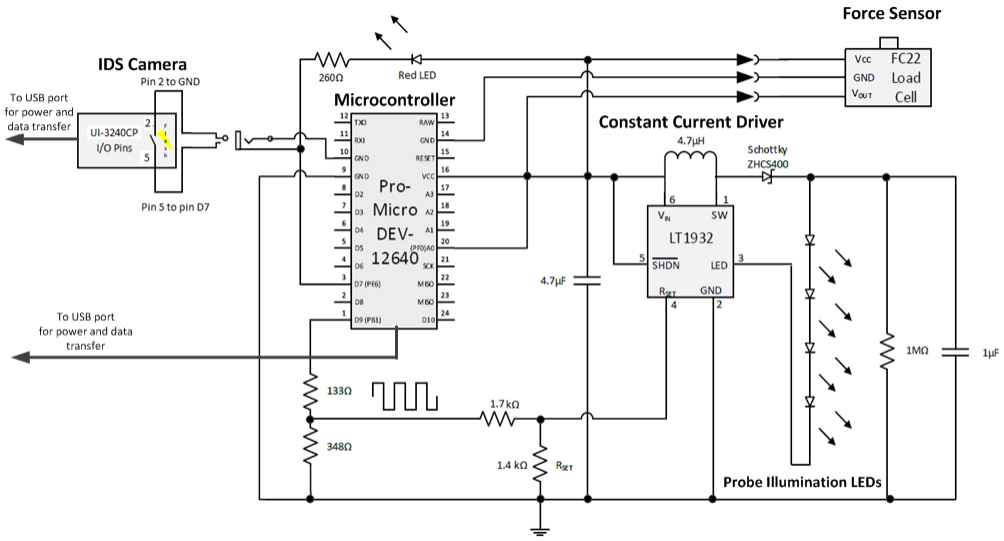

Figure 3.2: TIP Controller Circuit (Moser, 2016)

The image data, together with the corresponding compression force data, are continuously transferred to the laptop during acquisitions and saved to its hard drive using TIP acquisiÂňtion software. Finally, we use TIP calculation software to analyze the images and the force information and to quantify the mechanical properties of the embedded tumors.

3.3 Acquisition Software Design and Implementation

Acquisition software is used to control the acquisition through the controller unit, and to transfer the data from the camera and the force sensor to the laptop. Fig. 3.3 shows the TIP prototype connected to the laptop with the acquisition software graphical user interface (GUI) on the screen.

The software is based on the "ueyedemo" project bundled with the IDS uEye Linux

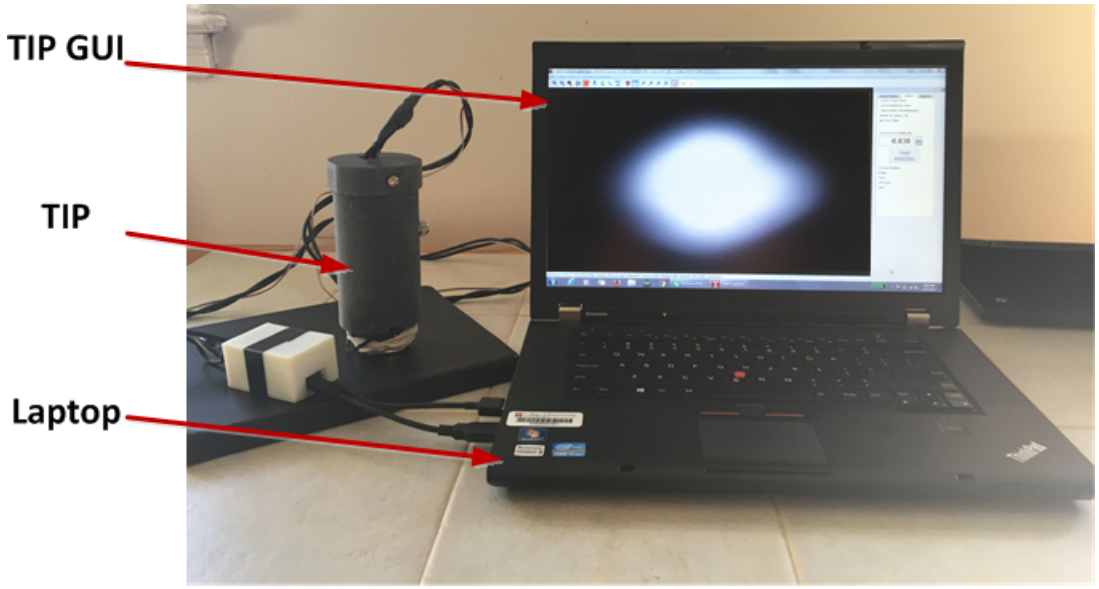

Figure 3.3: TIP Prototype Connected to TIP GUI

SDK. The GUI is developed with Qt Creator and Qt 4.8, uses MinGW C++ Compiler and OpenCV 2.4.13 library. The initial version of the GUI was created by Moser (Moser, 2016). We developed it further to satisfy the operational requirements from doctors and to make the overall operation procedure easier.

The TIP acquisition software operation has three sequential steps: setup, capture, and results.

The setup step allows the parameter to be set for the camera, controller, and force sensor, as well as the input of the information about the imaging session and the tumor. Fig. 3.4 shows the TIP GUI setup step.

After the setup is completed, we move to the capture step. Information about the current sample and the acquisition session number are displayed. Dynamic force information is provided on the screen in real-time as a value in Newtons and a color bar. The Zero button can be used to offset the force sensor. When the Start button is pressed, a number of tactile images with the corresponding forces are captured and saved to the session folder on the hard drive. The number of images in one session can be set from 1 to 270. The system takes 20 images per second. The applied force level is visualized on the side panel as a dynamic status bar. The bar area covers the range of forces from 0 to 50N. Also,

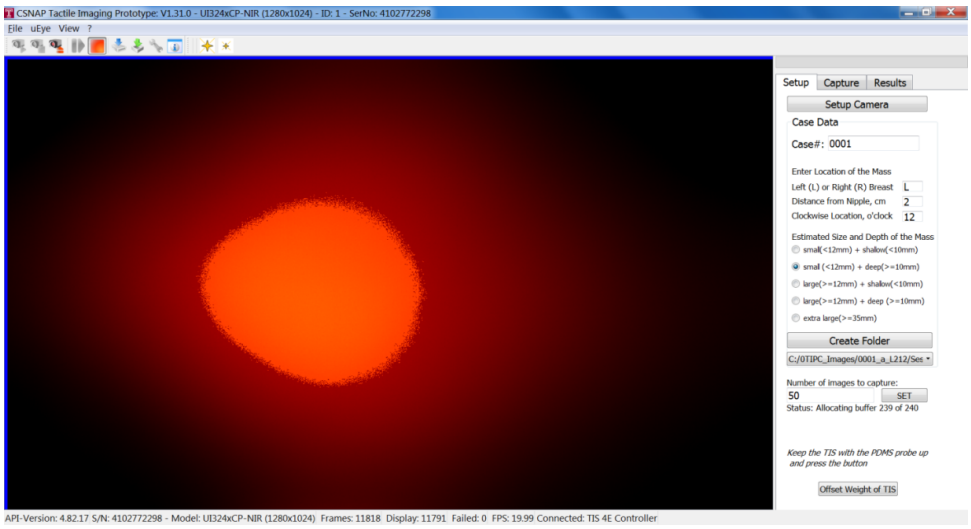

Figure 3.4: TIP GUI Setup

colors are assigned to different levels of compression force. The compression of up to 5N is not sufiňĄcient and will give the yellow color of the force status bar. Compressions between 5N and 45N will show the green color of the force status bar. This range is the typical acquisition range. Compressions over 45N will be indicated in red. These forces are considered to be excessive. Fig. 3.5 shows the TIP GUI capturing capabilities. After images from one compression session are saved, the software creates an additional folder with the false colored images for better visualization of the results.

Fig. 3.6 shows the folders with 50 tactile images and the corresponding force information from one compression session. Each image file name includes time and information about the acquisition. The image file names are in the following format:

`Case#<number>_TumorEstimationModel_TumorLocation_Compression#_YYYY-MM-DD_<Time in ms>_TIP_im#<image number>_<force in N>N.bmp`.

The final step is the results output. It designed to present the operator with the preliminary calculations of size and stiffness of the tumor, the confidence in the calculations, as well as the preliminary malignancy score estimation in the range from 0 (benign) to 5 (malignant). This step should help the operator to evaluate the quality of the completed acquisition, and to decide if additional compressions are needed. Fig. 3.7 shows the TIP GUI Results Tab.

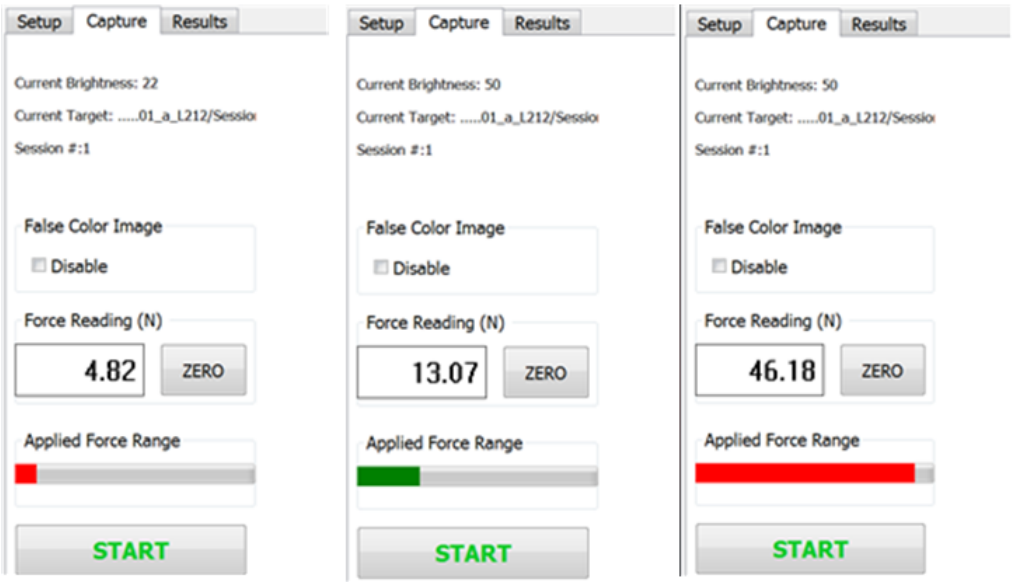

Figure 3.5: TIP GUI capturing capabilities

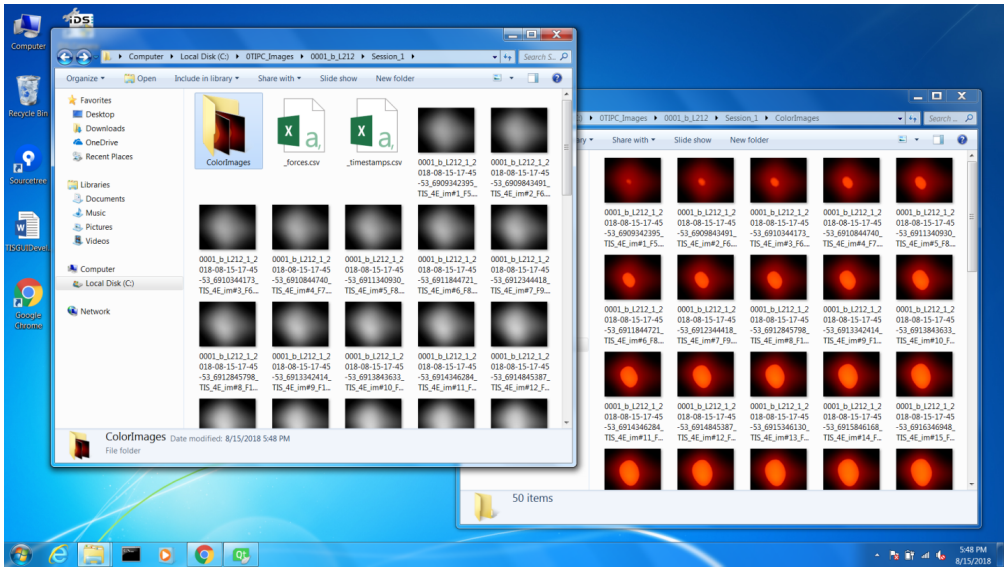

Figure 3.6: Example of the images saved during one TIP acquisition session.

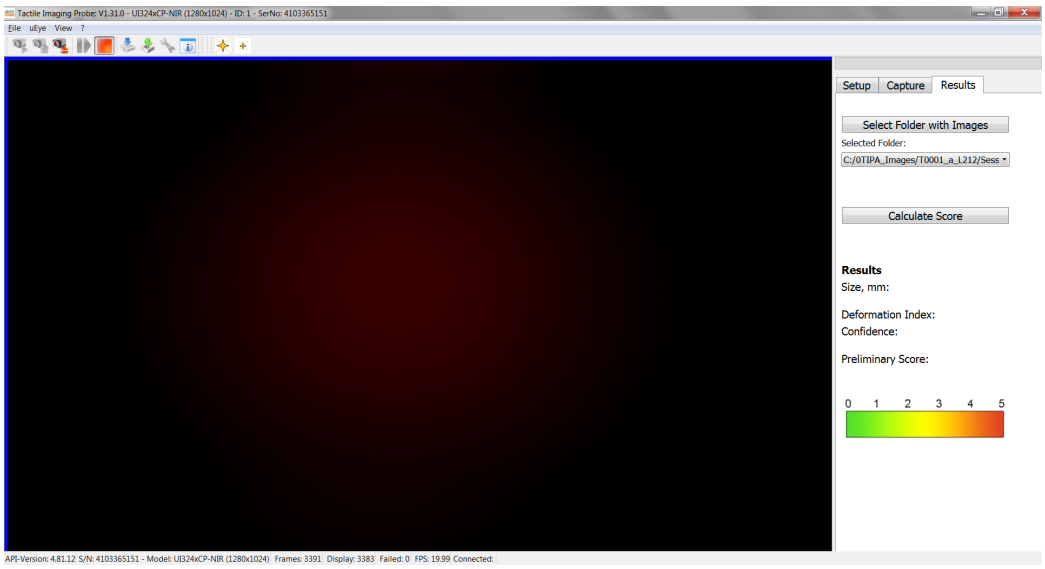

Figure 3.7: TIP GUI Results tab

3.4 Mechanical Properties Estimation Algorithm

The mechanical properties estimation algorithm evaluates the size and stiffness of the tumors by analyzing the tactile imaging sets with the corresponding applied force information from TIP acquisition sessions (Oleksyuk et al., 2018; Oleksyuk et al., 2015).

3.4.1 Numerical Simulation for TIP Sensing Element

We completed a numerical simulation for the TIP sensing element to understand how the contact surface of the sensor deforms during its compression against an embedded tumor. We used ABAQUS simulation software (ABAQUS Inc., RI, USA) to create the model.

To complete the simulation, we specified the components of TIP and multiple samples of tissue with tumors, their dimensions, and stiffness. We set up the sensing element dimensions (23 mm $\times$ 23 mm $\times$ 12 mm) and specified its stiffness as Young's modulus value (27 kPa). We also specified the thickness of the glass plate (3 mm), which supports the sensing element internal side. Next, we specified a range of breast tissue and tumor properties based on our breast mimicking phantom characteristics, which will be discussed in Chapter 7. We varied the size of the tumor from 5 mm to 30 mm and the stiffness of the tumor from 15 kPa to 465 kPa. We also varied the depth of the tumor within the tissue from

2 mm to 20 mm (the depth layer). Finally, we specified the range of applied force to TIP (5 N - 30 N), which caused the deformation of the polymer in contact with the tissue sample. Fig. 3.8 outlines our ABAQUS model setup.

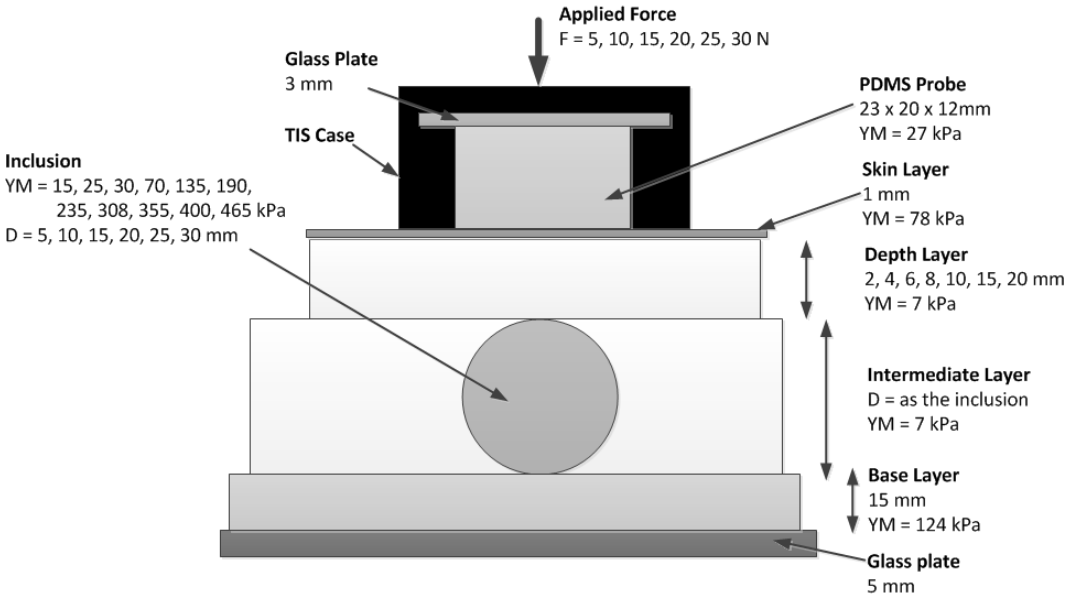

Figure 3.8: ABAQUS simulation setup

The results from the numerical modeling are summarized in Fig. 3.9. The three graphs describe the deformation effect from varying tumor size, stiffness, and depth, respectively, for the selected 26 N applied force. Each of these parameters has a unique effect on the formed tactile image, so it is possible to develop algorithms to estimate these properties from the sets of TIP images.

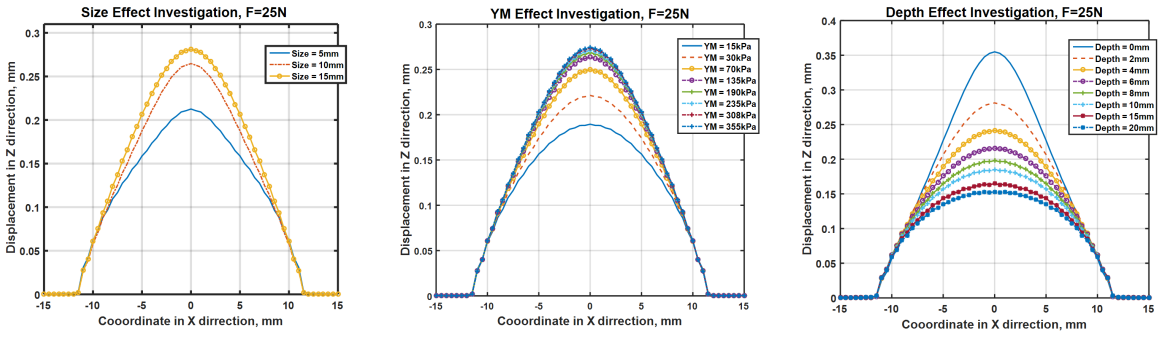

Figure 3.9: Abaqus simulation results

3.4.2 Tumor Size Estimation

To estimate the size of a tumor from a set of tactile images, we developed a three dimensional (3D) interpolation models (Oleksyuk et al., 2018). The 3D interpolation method relates the size of the tumor as diameter measure, D, applied force in compression, F, and the sum of pixel intensities value on the corresponding tactile image, I_p. We built several interpolation models to adjust the method for different tumor sizes and depths. To use the modeled surfaces for size calculation, we employ (3.1). To prepare for the calculation, we collect applied force data, F, from the force sensor, calculate the sum of pixel intensities from the corresponding tactile images, and use the estimated depth information from the TIP operator. Then the we employ (3.1) to calculate the size of the tumor.

$$D(F, I_p) = \sum_{i=0}^{i=n} \sum_{j=0}^{j=m} p_{ij} F^i I_p^j. \tag{3.1}$$

The size estimation model coefficients, p_{ij}, define the shape of the modeled surface. Indices n and m in (3.1) denote the order of the polynomial for the size estimation. We developed a third order polynomial surface for the 3D interpolation (i.e., n=3, m=1), which fits our empirical data the most. We also build four 3D models for four different imaging scenarios. The four models are designed for large and deep inclusions, large and shallow inclusions, small and deep inclusions, and small and shallow inclusions. Fig. 3.10 shows an example of the model for large ($D > 12$ mm) and deep (> 10 mm) tumors. The size and depth thresholds depend on the application.

3.4.3 Tumor Region Stiffness Estimation

The extend at which the sensing element gets deformed during TIP compression against the embedded tumor within the tissue is called the deformation index. The amount of deformation depends on the tumor's size and stiffness, as well as on the stiffness properties of the sur-rounding tissue. When the conditions of the depth, size, and applied force are fixed, the stiffer tumor deforms the surface of the sensing element more than the softer tumor. Fig. 3.11 shows the surface deformation of the TIP sensing element in compression against stiffer inclusion vs. a softer inclusion.

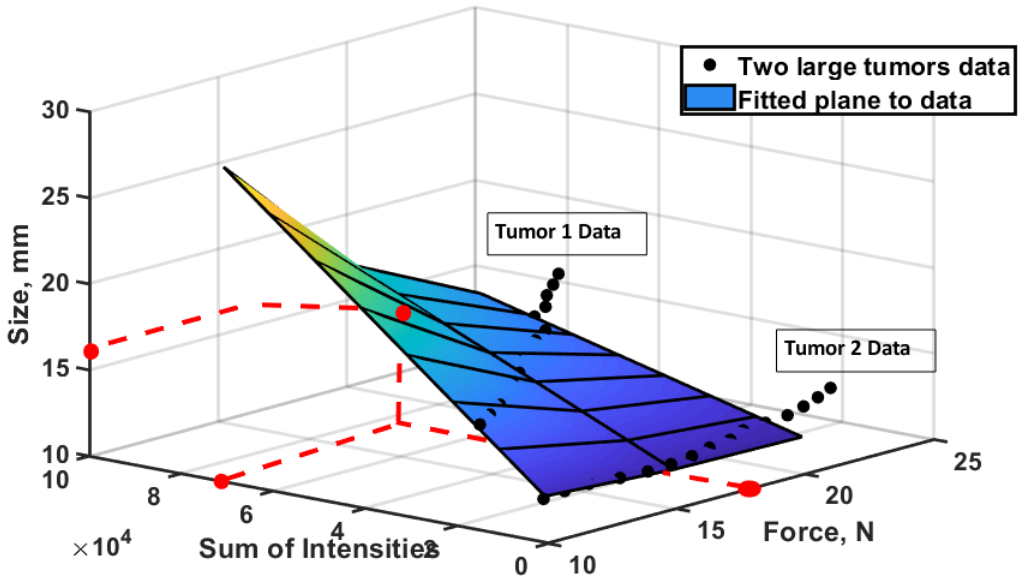

Figure 3.10: Example of a 3D interpolation model

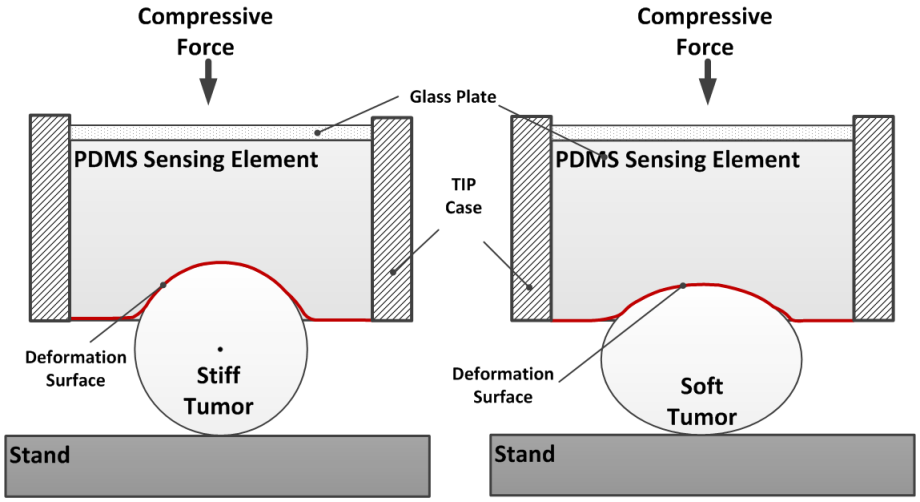

Figure 3.11: TIP sensing element deformation

Every image is defined as a multiple of 8-bit grayscale numbers (0 to 255) with the size of 1024 $\times$ 1280 pixel. Consider that the reference force F_{ref} is applied to the contact region (phantom), which produces a reference image M_{ref}, which is 1024 $\times$ 1280 matrix. The i^{th} tactile image, M_i, is obtained after applying a force F_i. The change in the pixel intensities can be represented as (3.2).

$$\Delta M = M_i - M_{ref}, \tag{3.2}$$

here i = 1, 2, 3 ... .

The change in the force values corresponding to change in pixel intensity can be calculated as given below:

$$\Delta F_i = F_i - F_{ref}, \tag{3.3}$$

where i = 1, 2, 3 ... .

The deformation index, DI, is the slope value of the graph plotted with the sum of pixel intensities ΔM_i vs. the change in the applied force ΔF_i, which is calculated using (3.4).

$$DI_i = \frac{\sum_{l=1}^{n}\sum_{k=1}^{m}\Delta M_i^{l,k}}{\Delta F_i}, \tag{3.4}$$

where the i^{th} tactile image has l rows and k columns.

3.5 Semi-automatic Mechanical Properties Estimation GUI

We developed a semi-automatic mechanical properties estimation graphical user interface using GUIDE application in MATLAB named MP_EST_GUI. The GUI loads one set of tactile images, eliminates outlier samples within the set, visualizes the compression force data, automatically searches for the best compression subset to be analyzed, plots the stress-strain characteristic for the selected subset, and calculates size and stiffness of the tumor. The GUI allows the operator to define the subset manually and to make the estimations. Fig. 3.12 shows MP_EST_GUI results for an imaging session with 270 images. There were three compressions within that acquisition session. The GUI automatically selected the best compression for analysis out of the three, which is between the two red points on

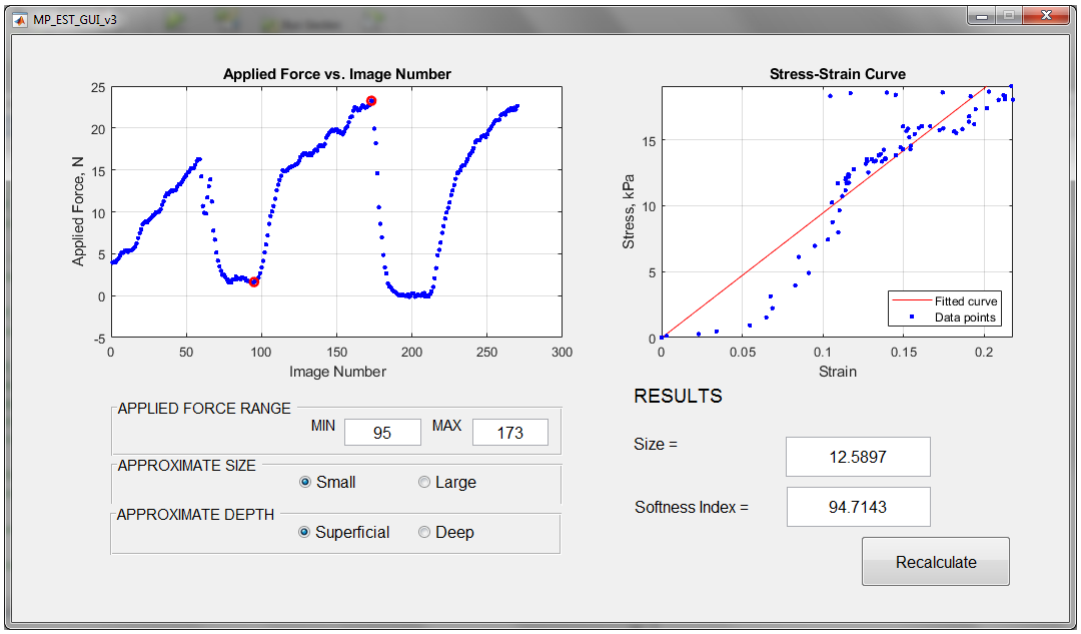

Figure 3.12: GUI visualizations and calculations

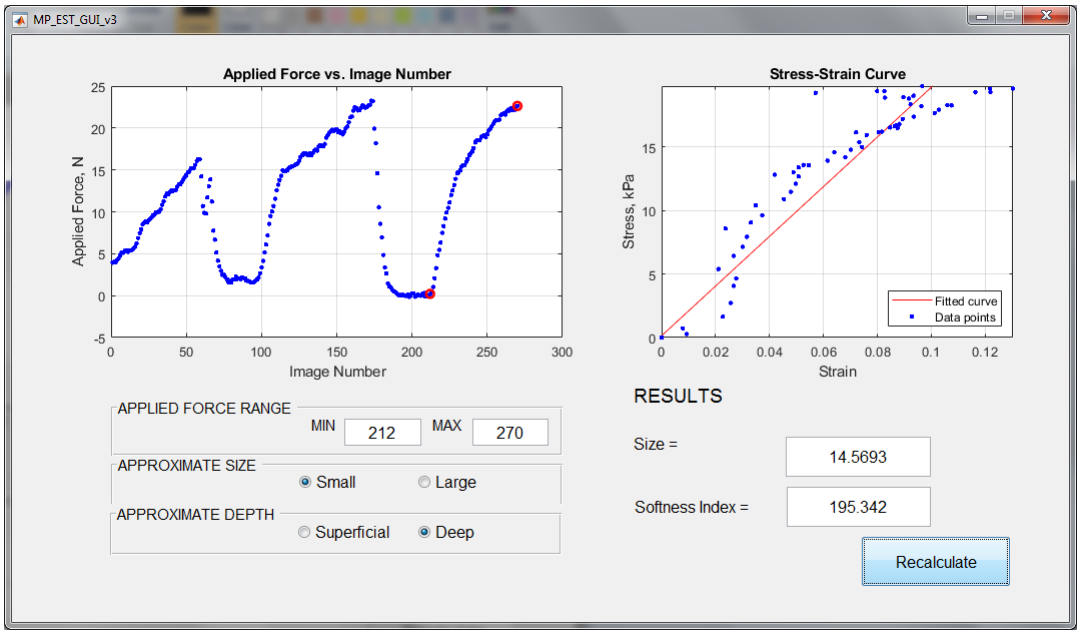

Figure 3.13: GUI output after the change of the subset and parameters

the left graph. Fig. 3.13 presents MP_EST_GUI results for the same session, yet when we manually selected another subset for analysis and changed the depth estimation. The GUI is very useful for processing multiple TIP sessions, where we want to decrease the calculation time yet obtain quality results. The operator is able to process data in an interactive manner and visually verify the tactile imaging data.

3.6 Tactile Profile Diagram

Clinical data is highly multimodal due to the variety of sensors and diagnostic devices. The data can be one- or multi-dimensional; it can be stationary or dynamic, depending on how it was generated. Therefore, different methods are applied to the analysis of medical data. Time series data is one of the most popular in the field. One patient in a hospital can generate a large amount of such data. The dynamic data can produce more useful information about the patient's condition than the static data; however, due to the computational limitations, not all of it will be analyzed and used for classification.

Clinical time series data analysis was explored by many researchers (Imani et al., 2011; Uniyal et al., 2014). Recently, researchers directed their attention on the processing of the series of data with deep learning tools by visualizing time series data via pattern images (Hatami et al., 2017; Hatami et al., 2018). The reconstructed patterns from time-series data given names such as Gramian Angular Summation/Difference Fields and Markov Transition Field (Wang and Oates, 2015).

One of the fields, which explores the dynamic properties of time-series signals for a long time is the speech processing field. In speech processing and recognition, it does not make much sense not to process sounds over the wide range of frequencies and time (Riley, 1989). Spectrograms are the way of visualization speech signals (Howard and Murphy, 2007; Fulop, 2011). A spectrogram is a visual representation of time-varying frequencies of an acoustic signal. It reflects on acoustic energy stored within the signal over a period of time (Howard and Murphy, 2007). Spectrogram can be presented as grayscale or a color plot Fig. 3.14. Human hearing relays on signals from the cochlea of the inner ear. These signals are functionally similar to how spectrograms are developed (Smith, 2007), so it

makes sense to represent audio signals via spectrograms (Riley, 1989).

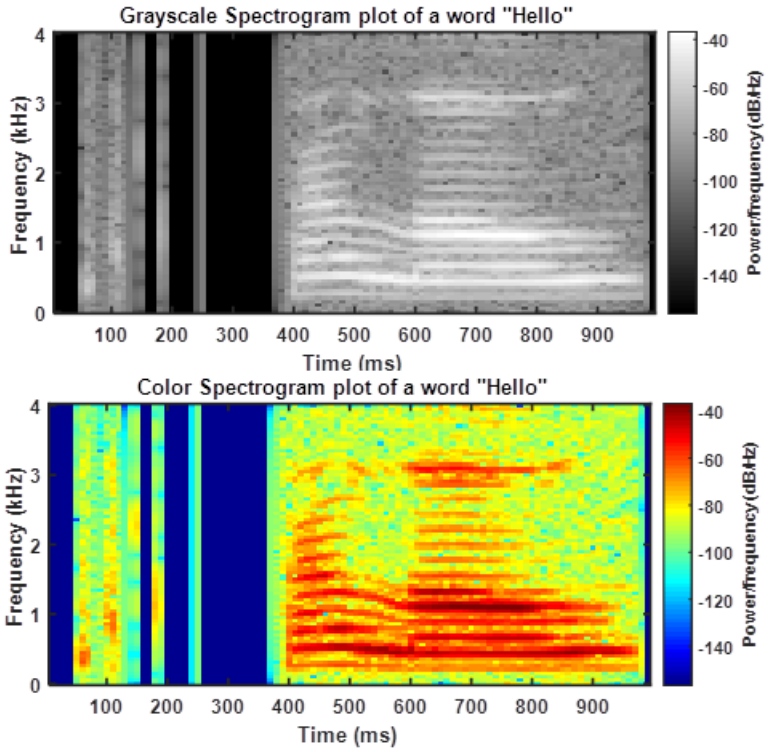

Figure 3.14: Example of a speech signal representation via a spectrogram

Human touch sensation is based on signals from tactile sensors throughout our body and are processed in the parietal lobe of our brain (Center for Plasticity of the Brain, 2016). The tactile signals are processed in our brain very similar to the visual signals (Bicchi et al., 2008). Tactile Imaging Probe (TIP) is developed to measure the tactile properties of touched tissues (Lee and Won, 2011; Oleksyuk et al., 2018). So far, we described how TIP and its algorithms estimate the size and stiffness of embedded tumors from the series of tactile images.

We wanted to use the differential tactile information as a dynamic signal we obtained during TIP acquisition sessions to improve the tumor characterization. With that goal in mind, we propose the method of combining sets of tactile images into one representative diagram, called Tactile Profile Diagram (TPD). TPD is a complex tactile image, which combines the information from a set of 50 single tactile images and gives a possibility of using the dynamic information from tactile imaging with TIP.

3.6.1 Tactile Profile Diagram Development

Here we present a method to construct a Tactile Profile Diagram (TPD) as a representative pattern image of a TIP imaging set. TPD is a pictorial representation of relative stiffness and size of the imaged tumor. The range of applied force should be kept the same between different TPDs. We used the range from 15 N to 45 N.

TPD carries a tumor's size and stiffness information in the form of a stiffness map for the imaged tissue region over the range of applied forces. However, a raw TIP image characterizes the stiffness distribution of a region for an instantaneous value of the compression force. The method of creating a TPD from a set of tactile images is as follows.

We acquire a set of images with TIP by compressing it on the region with a tumor. The number of raw tactile images, $I_i(x,y)$, in a set is $i = 1,2,...,N$. Variables x and y are the horizontal and the vertical coordinates respectively of a pixel within an image I_i. We apply an averaging filter with a non-overlapping sliding window of size 10 pixels $\times$ 10 pixels to each $I_i(x,y)$ to reduce the level of white noise within the images, decrease image size without the loss of tactile information, and improve the speed of computations. The pixel values in the created reduced image, $R_i(m,n)$, corresponding to the average values of pixel intensities in the window at each step. The number of reduced images in the set is the same as the number of original images. The size of the reduced images is 103 pixels (m) $\times$ 128 pixels (n). The reduced images are the more compact copies of TIP raw images.

Each tactile image, I_i, has a corresponding compression force value. The $\acute{F}_i$ is the vector of forces of size $N \times 1$. Similar to the pre-load step during Instron tests (Mangano, 2014), we select a reference force, F_{ref}, and it's corresponding reference reduced image, $R_{ref}(m,n)$, from the set to account for the imperfections at the test tissue surface. Empirically, we chose 5 N as F_{ref}. To obtain the vector of the change in compression force, ΔF_i, we subtract the reference force value from the force vector.

$$\Delta\acute{F}_i = \acute{F}_i - F_{ref} \cdot \acute{1}_{N\times 1}, \tag{3.5}$$

Subsequently, we complete pixel-wise subtraction of the reference reduced image, $R_{ref}(m,n)$, from all reduced images, $R_i(m,n)$, in the set to create an image set ΔR_i, which represents the change in tissue deformation under compression. These images describe the

deformation of the silicone sensing element of the TIP.

$$\Delta R_i(m,n) = R_i(m,n) - R_{ref}(m,n), \tag{3.6}$$

Next, we find the maximum intensity value, ΔR_{max}, present in the ΔR_i images set. Then we subtract each pixel value in ΔR_i images from ΔR_{max} to get the change of deformation images, ΔW_i, of the tissue with inclusion, and not of the sensing probe's material.

$$\Delta W_i(m,n) = \Delta R_{max} - \Delta R_i(m,n), \tag{3.7}$$

To construct a Tactile Profile Diagram, we calculate Young's modulus index values, $YMI(m,n)$, which is the stiffness estimation parameter, for each pixel location in ΔW_i (Fig. 3.15). We mimic the definition of Young's modulus and calculate YMI in a pixel location (m,n) as a slope of the compression force over an area (the compression change $\Delta \acute{F}_i$) vs. the deformation change due to the compression (the change in deformation ΔW_i for the tissue with inclusion). To calculate the slope in each pixel location (m,n), N data points will be available from a TIP set. Finally, a TPD is obtained by plotting $YMI(m,n)$ for $m = 1...103$ and $n = 1...128$ (Fig. 3.15). If $\Delta \acute{F}_i$ is divided by the contact area and ΔW_i is correlated with the strain, then $YMI(m,n)$ is directly related to the young's modulus of the tissue at any given point at (m,n).

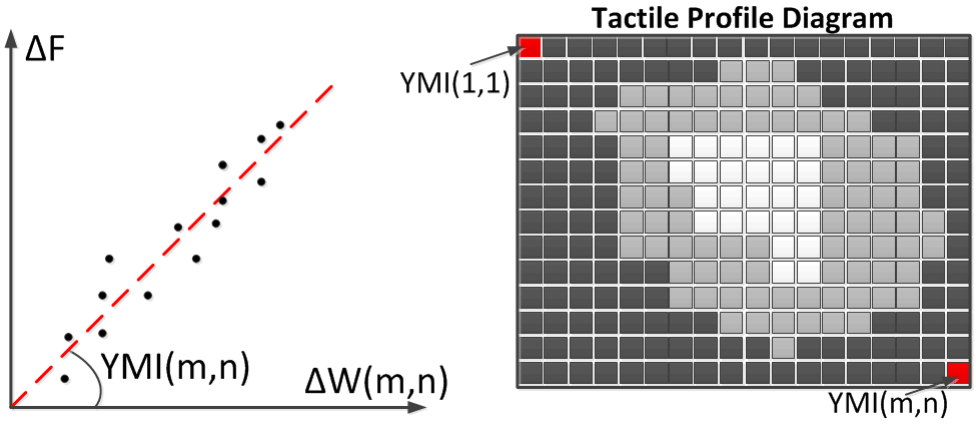

Figure 3.15: Tactile Profile Diagram Generation

3.6.2 Mechanical Properties Estimation Algorithm from Tactile Profile Diagram

To use Tactile Profile Diagrams for mechanical property estimation, the diagrams have to be segmented due to the high level of hardware-related noise in their perimeter. Then size and stiffness can be estimated from TPDs directly.

TPD Segmentation

Similar to the Canny edge detection method (Canny, 1986), we utilize directional gradient of TPD to find a region of interest for calculations. Because an image gradient is the directional change of the pixel intensity in an image, one can use it to detect intensity changes associated with the inclusion region vs. the changes due to the perimeter noise. We use MATLAB 2019a function $imgradient(YMI,'sobel')$ to create a gradient magnitude image, $G_{mag}(m,n)$, and a gradient direction image, $G_{dir}(m,n)$, from a TPD (MATLAB MathWorks, 2019). Next, we create a composite image, $G(m,n)$, from a difference between $G_{mag}(m,n)$ and $G_{dir}(m,n)$ using $imfuse(Gmag,Gdir,'diff')$. We semi-manually select the region of interest in the center of $G(m,n)$ image by following the edges of the circular region in Matlab using *drawassisted* function. The selected region corresponds to the inclusion indentation into the probe during the TIP test. Segmented image $G_{magS}(m,n)$ has zero-valued pixels outside of the selected region, and non-zero pixels inside it. The segmentation method steps are shown in Fig. 3.16.

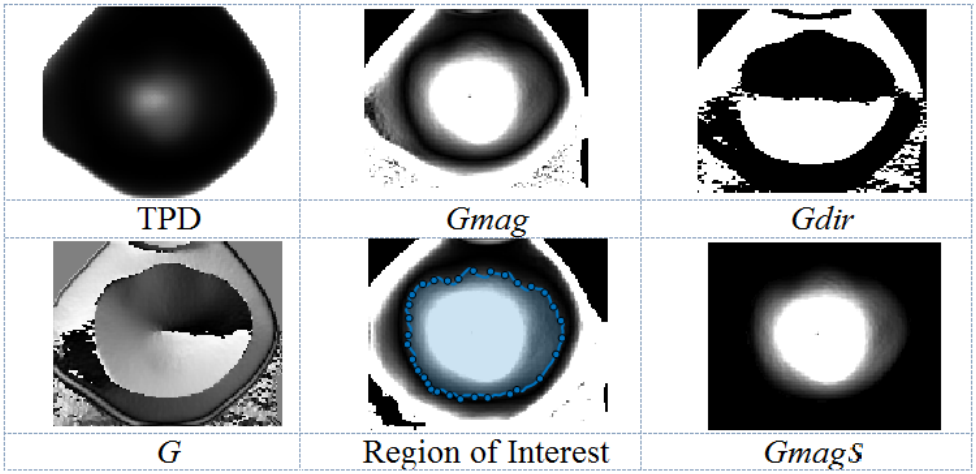

Figure 3.16: Tactile Profile Diagram segmentation

Tumor Size Estimation

Tumor's size is estimated by summing the number of non-zero pixels within the segmented image $G_{magS}(m,n)$. Next, this value is related to the tumor's size with the use of a linear regression model. Use (3.8) to find the size of the inclusion, D, in mm.

$$D = aN_p + b, \tag{3.8}$$

where N_p is the number of nonzero pixels in the segmented area, $a = 0.0019$ and $b = 7.1028$ are the empirical coefficients. The coefficients are developed by linear interpolation to the data points of known inclusion sizes vs. N_p from the corresponding $G_{magS}(m,n)$. Fig. 3.17 shows steps for size calculation.

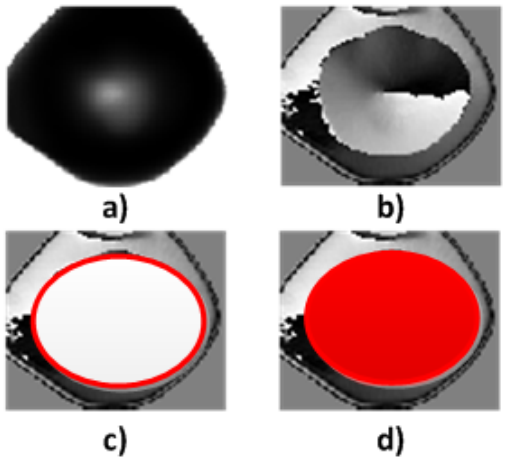

Figure 3.17: Tumor size calculation from a TPD: a)load a TPD; b) calculate $G_{mag}(x,y)$; c) detect edges of the tumor; d) calculate the number of pixels within the selected region inside the edges.

Tumor Region Stiffness Estimation

Stiffer the inclusion, the larger is the change in TPD pixel intensities, and the greater are the pixel intensities of the segmented gradient magnitude image G_{magS}. Therefore, we define Stiffness Index, SI, as the measure of the tumor's stiffness based on the collection of local stiffness measurements (YMI). The calculation of SI follows (3.9).

$$SI = \frac{\sum_m \sum_n G_{magS}(m,n)}{N_p}, \tag{3.9}$$

Therefore, in one number, *SI* represents the sum of all gradient magnitudes divided by the number of nonzero pixels. Stiffer the inclusion, the intensity changes will be larger, and *SI* will be larger.

Fig. 3.18 shows representative examples for four different imaging samples. The leftmost column describes a stiff and small tumor. The next column shows stiff and large tumor. The following column to the right represents soft and small inclusion. Finally, the rightmost column shows soft and large inclusion. For each case, we plotted 3D reconstruction of the image, the corresponding gradient images, and the segmented magnitude gradient images. The differences among cases can be seen. The stiff and large sample gives the most bright and large segmented gradient magnitude image, where the soft and small tumor produced the least bright.

3.7 Discussion

In this chapter, we described the sensing principle and design of the Tactile imaging Probe. We outlined the capabilities of the developed TIP acquisition software. Following, we presented the calculation algorithms for tumor size and stiffness estimation from sets of tactile images. Later, we proposed a method to represent dynamic tactile information from an imaged with TIP tumor in the form of a Tactile Profile Diagram. Finally, we described algorithms for tumor size and stiffness estimation from Tactile Profile Diagrams.

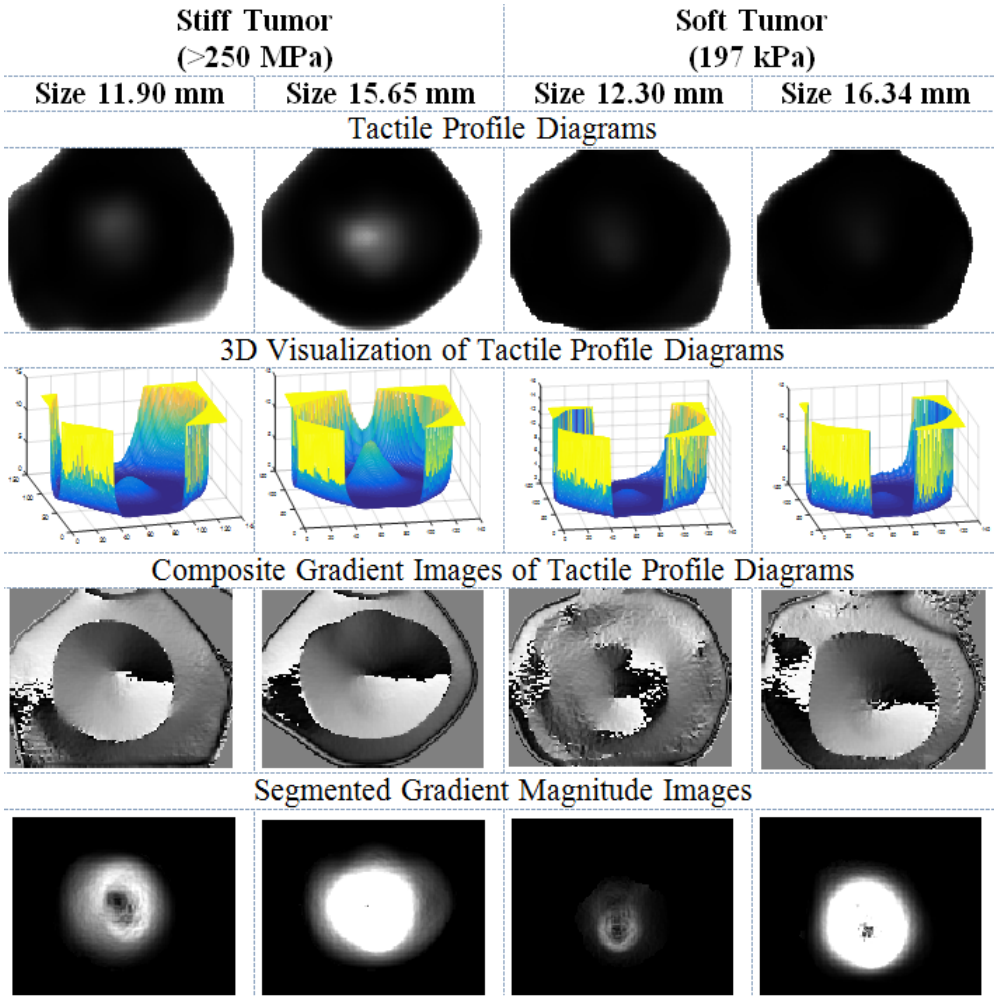

Figure 3.18: Tactile Profile Diagram results

CHAPTER 4

MULTISPECTRAL IMAGING PROBE

Researchers are constantly looking for new methods to measure tissue properties and to distinguish different tissue types. In this chapter, we describe the design and development of the Multispectral Imaging Probe to characterize the superficial properties of the potentially cancerous tumors.

4.1 Overview of the Modality

In Chapter 2, we gave an overview of breast imaging technologies, including near-infrared (NIR) and thermal imaging. The two methods use near-infrared or infrared (IR) light spectrum to image breast tissues. The advantages of the methods are their non-ionizing nature, and the ability to characterize the breast tissue metabolic properties.

Hyperspectral imaging is commonly used to image samples with high resolutions in the spectral and spatial domains. It requires significant acquisition time, special setup and conditions, as well as, sophisticated and complex image analysis (Qin et al., 2013). Because the tissue optical properties change when the tissue becomes malignant, due to angiogenesis and hypermetabolic activity, hyperspectral imaging has great potential in cancer diagnostic applications. Tissue absorption in the near infrared region is the lowest, so the light can penetrate deep into the tissue. For this reason, NIR imaging is the primary type of hyperspectral images of biological tissues (Lu and Fei, 2014; Nioka and Chance, 2005).

In our previous work, we used hyperspectral imaging for mammary tumors characterization (Sahu et al., 2014). The method evaluated levels of deoxyhemoglobin (Hb), oxyhemoglobin (HbO_2), water (H_2O), and lipid chromophores' within the imaged tissue regions.

For the current work, we propose to build on our expertise on hyperspectral imaging of mammary tumors to be used with Tactile Imaging Probe for breast tumor characterization as a multispectral imaging modality. Instead of imaging the whole NIR spectrum, we

will target the mentioned chromophores by tuning the imaging system to the chromophore revealing wavelengths. Tests will be completed to find the appropriate wavelengths for this task.

4.2 Hardware Design and Imaging Principles

Hyperspectral imaging collects and processes information for a scene from across the electromagnetic spectrum. Fig. 4.1 illustrates the difference between an RGB image and a hyperspectral image. The goal of hyperspectral imaging is to obtain the spectrum for each pixel in the image of the scene, to finding objects, identify materials, or detect metabolic changes.

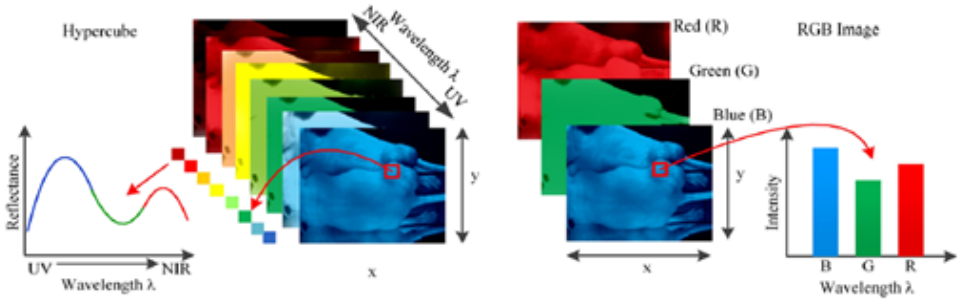

Figure 4.1: Hyperspectral image vs. bitmap image

Biological tissues are composed of multiple molecular types, which cause their nonhomogeneous optical properties. Light scatters and gets absorbed while traveling through the tissue (Fig. 4.2). The difference in refractive indices causes the light to be scattered within the tissue.

The depth of light penetration is an important characteristic for optical measurements. The imaging depth depends on the tissue absorption properties (Jacques, 2013). Light absorption is at its minimum at the NIR range from 600 nm to 1300 nm for most living tissues (Fig. 4.3). In that range, the scattering is greater than absorption, so the light diffuses into the tissue the most, and can reach the depth of up to 15 mm (Lu and Fei, 2014).

Chromophores are the tissue components that absorb light, and their absorbance depends on the wavelength Fig. 4.3. It is important to mention, that light travels a random

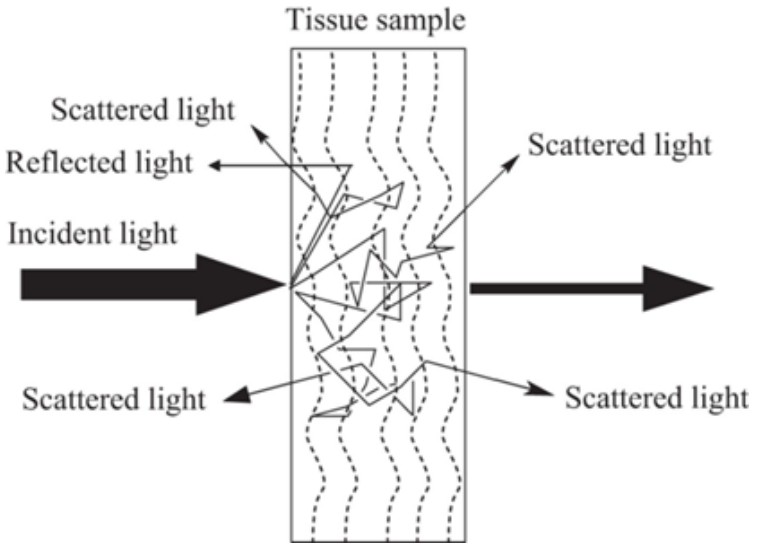

Figure 4.2: Light reflectance, scattering, and transmission within a tissue sample

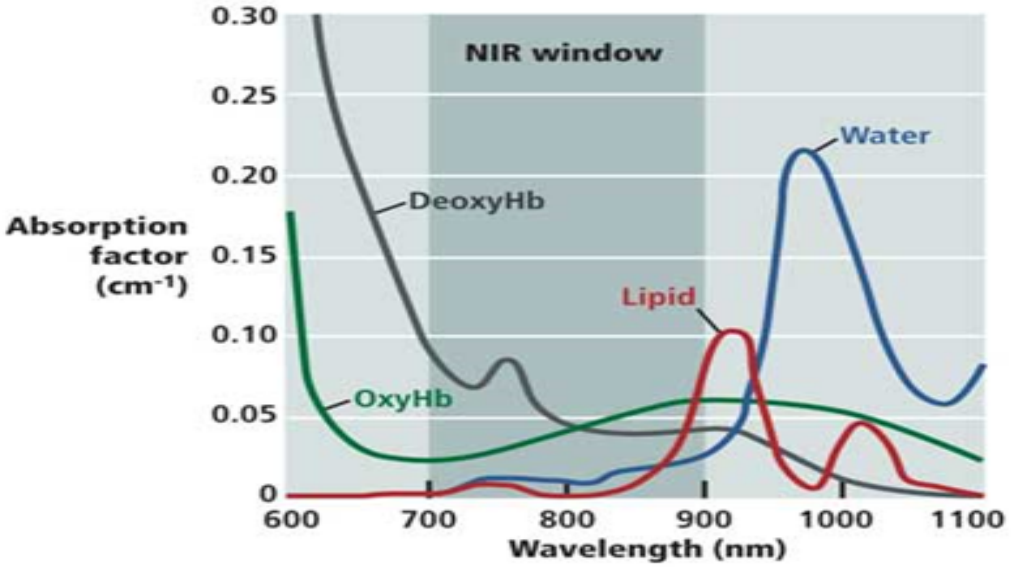

Figure 4.3: Absorption spectra of different tissue chromophores (Godavarty et al., 2015)

path within tissue while scattering. This is called the diffused reflectance. The gradual histopathology changes of the unhealthy tissue will be captured by the reflectance spectra shape of that region.

For hyperspectral experiments, we used RetigaEXi F-M-12-C hyperspectral camera (QImaging Inc., Surrey, BC, Canada) and a VeriSpec NIR liquid crystal tunable filter (LCTF) (Cambridge Research, and Instrumentation Inc., Woburn, MA, USA). The camera with the lens had the LCTF block pictured on Fig. 4.4. Hyperspectral images were taken for each 10 nm band from 650 nm to 1100 nm. Two quartz tungsten halogen lamps (500 W each) were used for tissue samples illumination. Visualization of images and analysis of the spectral data were performed using ENVI v4.5 (Exelis Visual Information Solutions, Boulder, CO, USA) and MATLAB (The MathWorks, Inc., Natick, MA, US).

Figure 4.4: Hyperspectral camera acquisition system

For the current work, we changed the acquisition hardware to make it less expensive, less bulky, and more adjusted to the application of breast imaging. We shifted from the hyperspectral imaging to the multispectral imaging idea. We decided to target the tissue chromophores we are most interested in (deoxyhemoglobin, oxyhemoglobin, water, and lipids) (Sahu et al., 2014), instead of taking images for the entire NIR spectrum. The number of images to analyze will decrease from 48 to 4.

Because the TIP video camera (IDS UI-3240CP-NIR) has NIR sensitivity, and the Xenoplan 1.4/23mm, 5 megapixel lens (Schneider Optics Inc., Hauppauge, NY) is de-

signed to work with NIR spectra, we compared two cameras to assess the possibility of using TIP's camera and lens for multispectral imaging, see Fig. 4.5.

Figure 4.5: IDS UI-3240CP-NIR

Figure 4.6 shows the comparison of the quantum efficiencies between two cameras. Table 4.1 shows the comparisons of the two camera parameters.

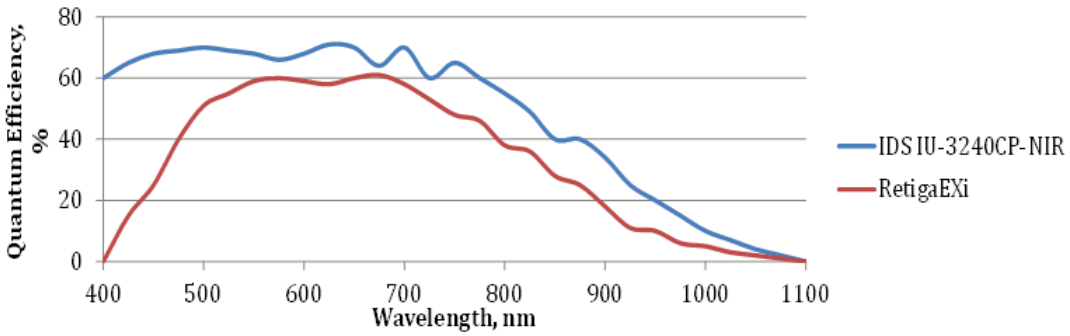

Figure 4.6: Comparative characteristic of the quantum efficiency curve for both cameras (QImaging, 2014; IDS Imaging Development Systems GmbH, 2015)

We can see from the comparison that the key properties for the two cameras are very similar. Therefore we completed an experiment to compare the acquisition parameters of the TIP camera (IDS UI-3240CP-NIR) with the hyperspectral camera (RetigaEXi F-M-12-C) used in our previous experiments. Both cameras were focused on the same image sample. The illumination and distance settings were exactly the same for both setups. The multispectral images were taken for 700 nm and for 840 nm. The setup of the experiment is shown in Fig. 4.7.

From the comparative research on the topic and the imaging experiment, we found the more compact and less expensive IDS camera had very similar performance to the

Table 4.1: Comparative characteristics of the two cameras(QImaging, 2014; IDS Imaging Development Systems GmbH, 2015)

PARAMETER	IDS UI-3240CP-NIR	RetigaEXi F-M-12-C
Sensor Type	CMOS	CCD
Resolution, μm	5.3×5.3	6.45×6.45
Max Image Size, *pixel*	$1,280 \times 1,024$	$1,390 \times 1,040$
Pixel Depth, *bit*	8	12
Acquisition Speed, f/s	60	10
Dimension, *mm*	29L×29W×29H	150L×76W×64H

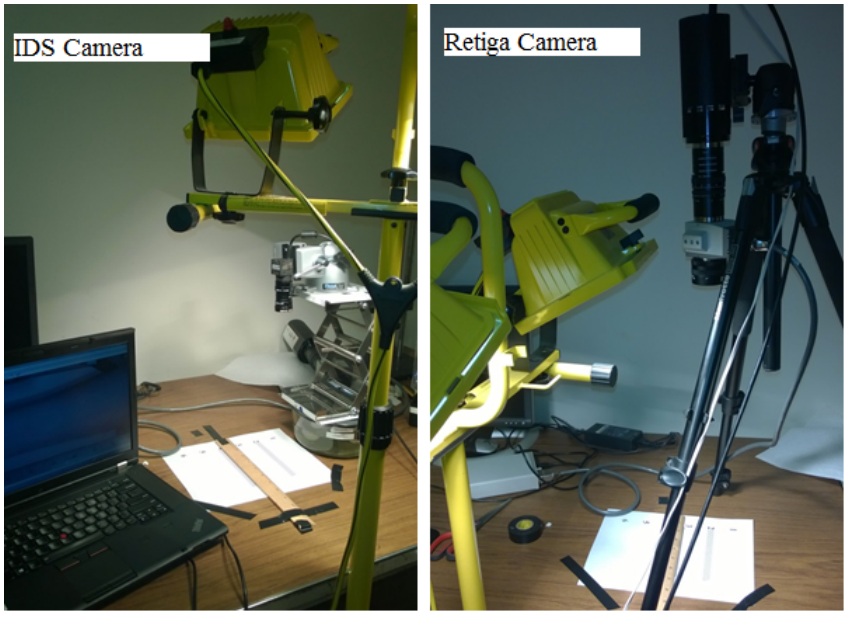

Figure 4.7: Two imaging systems setups

performance the Retiga camera for breast imaging application. The spectral response and the pixel resolution are alike. The hyperspectral camera has larger pixel depth and larger image area size. The optics is better in the Retiga camera. Nevertheless, the resulting images from the experiments showed very good quality for both cameras at different tested

wavelengths. The temperature conditions influenced the performance of both cameras and have to be taken into the account during future acquisitions. It is reasonable to assume that the performance of IDS camera will match the needs of the application.

The proposed design of the Multispectral Imaging Probe includes the TIP camera and the lens with four bandpass filters attached to it. The filters are the hard coated OD 4.0 10 nm bandpass filters (Edmund Optics Inc., Barrington, NJ). They will limit the imaged reflected light to the target wavelengths. Fig. 4.8 shows the proposed MIP hardware components.

Figure 4.8: Multispectral Imaging Probe hardware components

4.3 Acquisition Software

We propose the modification to the TIP acquisition GUI in Qt (The Qt Company, Espoo, Finland). Using this GUI, we integrate the needs of Multispectral Imaging Probe.

The proposed changes will include the setup of five images per acquisition. We will acquire five images in a burst for each wavelength. There will be four imaging sessions for each of the four selected wavelengths.

Additionally, we will develop the acquisition graphical user interface to include the space for entering the acquisition mode information (tactile/multispectral), to specify the wavelengths, and to set up the information about the samples. Each of the sets of 5 images

with the corresponding acquisition information will be saved in a directory with four sub-folders for each wavelength.

4.4 Optical Properties Estimation with Multispectral Imaging Probe

We propose to use the Multispectral Imaging Probe to estimate the superficial optical properties of breast tissues.

4.4.1 Image Pre-processing

Image pre-processing involves data smoothing, normalization, and image registration. The smoothed and normalized multispectral images will be aligned to improve the optical properties characterization performance of MIP.

Image Smoothing

For the image smoothing, we use a median filter to eliminate the "salt and pepper" type noise coming from the sensor. The suggested filter window size is 5, which is enough to eliminate the noise speckles, yet not enough to significantly decrease the image resolution. This procedure prepares multispectral images for the normalization step.

Image Normalization

Reflectance normalization is done to normalize the raw acquisition image data to the reflectance or absorption values. Normalization decreases the effect of the inhomogeneous illumination of the imaged region and the hardware-related noise, such as the dark current of the imaging sensor. The dark current level increases with temperature and integration time.

In our test setup, we acquire two additional images for normalization purposes. The first is the image taken with the closed lens. No external light should reach the sensor. This image will characterize the dark current level in the imaging system. The second is the reference image of a standard reflectance surface (National Institute of Standards and Technology certified 99% Spectralon white diffuse reflectance target). This image will be used to convert raw multispectral images, I_{raw}, to normalized reflectance images, I_{norm}.

All four multispectral images from one test sample set have to be pre-processed and

normalized. The conversion from raw images to the normalized images is done pixel by pixel using the following equation.

$$I_{norm} = \frac{I_{raw} - I_{dark}}{I_{white} - I_{dark}}, \tag{4.1}$$

were I_{raw} is the reflectance intensity from the raw multispectral images obtained during the experiments, I_{white} represents pixel intensity of the white reflectance standard, I_{dark} is the black current pixel intensity.

Image Registration

Image registration searches for the geometric transformation of multiple images of the same scene to align them. In our case, we align four images that captured reflectances in the four selected wavelength bands. Image registration is a necessary step for the multispectral image alignment and analysis (Modersitzki, 2004; Gonzalez and Woods, 2008; Calin et al., 2014). We are mostly interested in translational distortions due to the nature of MIP tests. The methods for image registration will be developed.

4.4.2 Multispectral Profile Diagram

To characterize superficial optical properties of the breast tissue, we will implement the same idea as was developed for the sets of TIP images. In this section, we describe how we can construct Multispectral Profile Diagrams (MPD) from the sets of pre-processed (smoothed, normalized, and aligned) multispectral images. MPDs carry unique information about the optical properties of breast tissue from four imaging bands consolidated in one pattern image. The wavelength bands are selected to target the chromophores of interest in the breast cancer application. Such chromophores are deoxy-hemoglobin, oxy-hemoglobin, lipids, and water.

From our previous research developments, we know that a higher total hemoglobin content indicates higher tissue blood volume and malignancy. Higher water content suggests malignancy as well. Decreased lipid content indicates that the parenchymal adipose tissue has been displaced, which is a warning sign for malignant mass (Sahu et al., 2014).

The reflectance changes of these chromophores are combined into Tissue Optical Index (TOI) formulation expressed via (4.2). The lower TOI values suggest high metabolic

activity and probable malignancy (Sahu et al., 2014).

$$TOI = \frac{R_{H_2O}(R_{Hb} + R_{HbO_2})}{R_{lipid}}, \tag{4.2}$$

where R_{Hb} is the total reflectance of deoxy-hemoglobin chromophores, R_{HbO_2} denotes the total reflectance of oxy-hemoglobin chromophores, R_{H_2O} is the reflectance of water, and R_{lipid} expresses the reflection of lipids within the imaged tissue.

The tissue optical index was calculated for the manually segmented multipixel patch within the imaged tissue region. In this work, we propose to construct a Multispectral Profile Diagram from the four multispectral images and calculate TOI for each pixel in the aligned image set. It will help us to extract the high resolution information on the chromophores' concentration automatically without manual region selection in ENVI software.

After MIP multispectral images are pre-processed and aligned, we create a Multispectral Profile Diagram for the imaged tissue sample. Each pixel of the Multispectral Profile Diagram will be calculated as equation (4.3). When all calculations are done, the Multispectral image is composed and shown on Fig. 4.9.

$$MPD_{M\times N} = \begin{bmatrix} \frac{\acute{c}_{1,1}(\acute{a}_{1,1}+\acute{b}_{1,1})}{\acute{d}_{1,1}}, & \frac{\acute{c}_{1,2}(\acute{a}_{1,2}+\acute{b}_{1,2})}{\acute{d}_{1,2}}, & \cdots & \frac{\acute{c}_{1,N}(\acute{a}_{1,N}+\acute{b}_{1,N})}{\acute{d}_{1,N}} \\ \frac{\acute{c}_{2,1}(\acute{a}_{2,1}+\acute{b}_{2,1})}{\acute{d}_{2,1}}, & \frac{\acute{c}_{2,2}(\acute{a}_{2,2}+\acute{b}_{2,2})}{\acute{d}_{2,2}}, & \cdots & \frac{\acute{c}_{2,N}(\acute{a}_{2,N}+\acute{b}_{2,N})}{\acute{d}_{2,N}} \\ \vdots & \vdots & \ddots & \vdots \\ \frac{\acute{c}_{M,1}(\acute{a}_{M,1}+\acute{b}_{M,1})}{\acute{d}_{M,1}}, & \frac{\acute{c}_{M,2}(\acute{a}_{M,2}+\acute{b}_{M,2})}{\acute{d}_{M,2}}, & \cdots & \frac{\acute{c}_{M,N}(\acute{a}_{M,N}+\acute{b}_{M,N})}{\acute{d}_{M,N}} \end{bmatrix}, \tag{4.3}$$

where $\acute{a}_{m,n}$ corresponds to the multispectral image taken to capture Hb concentration, $\acute{b}_{m,n}$ is the multispectral image taken to capture HbO_2 concentration, $\acute{c}_{m,n}$ corresponds to the multispectral image taken to capture $Water$ concentration, and $\acute{d}_{m,n}$ is the multispectral image taken to capture $Lipid$ concentration. $m = 1,2,\ldots,M$ is the image row number, $n = 1,2,\ldots,N$ is the image column.

An example of a Multispectral Profile Diagram is shown in Fig. 4.10.

4.4.3 Multispectral Profile Diagrams for Differential Tissue Properties Estimation

To characterize superficial optical properties of breast tissue, we will develop a method to find the following parameters: differential color, differential size, differential texture,

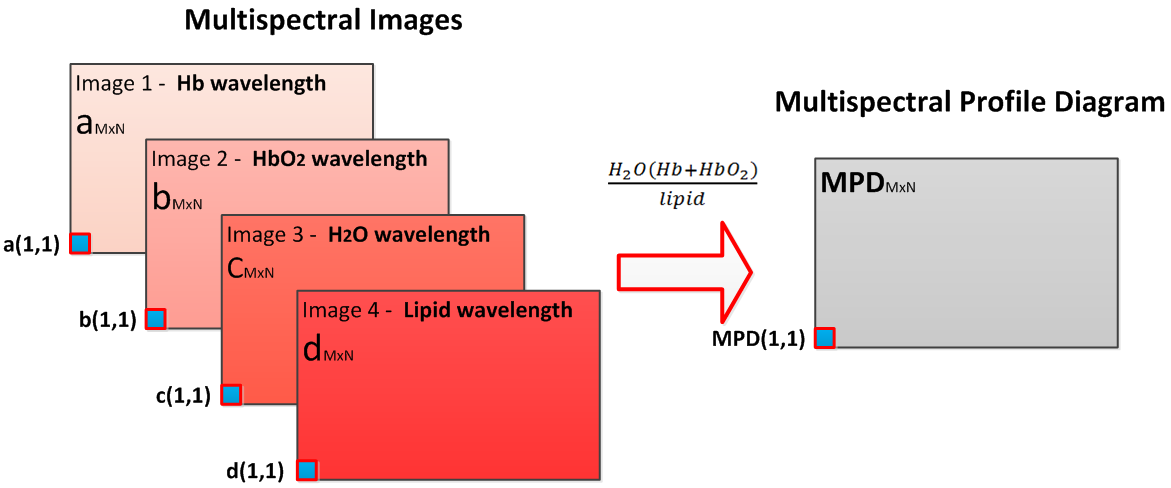

Figure 4.9: Construction of a Multispectral Profile Diagram

and differential asymmetry from a set of two Multispectral Profile Diagrams (MPD of the affected and MPD of the normal breasts from the same subject).

These parameters showed potential for helping doctors during cancer diagnostic steps, such as classifying the tumors on malignant or benign or deciding the stage of the disease (Robertson et al., 2010; Boisserie-Lacroix et al., 2012; Garg, 2014; NIH, 2006; Garza-Salazar et al., 2013).

The differential parameters will reflect the difference between the normal breast and the affected breast tissue for a patient in terms of skin color and texture, size of the reddened region, and the extent in the lateral asymmetry of breasts. The idea is similar to the data normalization idea. Because all of the patients have distinct anatomy of normal breast tissues, the abnormal tissues will have varying manifestations. Therefore, normalization is crucial.

4.5 Discussion

In this chapter, we described the Multispectral Imaging Probe development. We outlined its hardware development, the principle of operation, and the imaging data analysis strategies for the imaging modality. We propose a method for combining the information from multiple multispectral images into the Multispectral Profile Diagram. We also described the

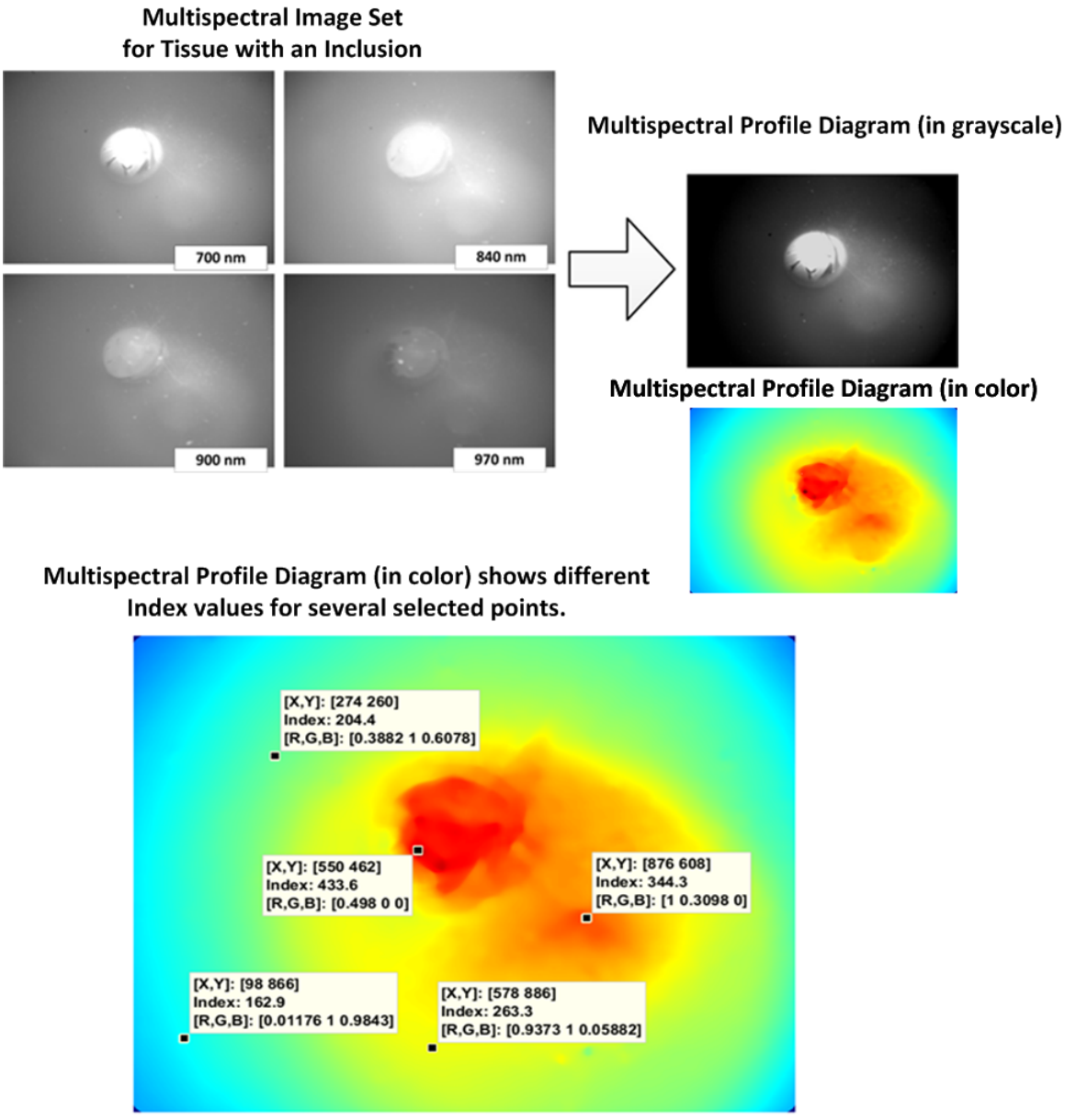

Figure 4.10: Multispectral Profile Diagram Example

parameters we evaluated from the multispectral imaging modality to characterize tissues and to aid breast cancer diagnostic.

CHAPTER 5

CLASSIFICATION

In this chapter, we develop classification methods to extract desired information about the imaged tumor from Tactile Profile Diagrams and the superficial optical properties from Multispectral Profile Diagrams. We will use the results of the classifications to calculate the Malignancy Risk Score for the tumor. Also, classification results will improve tumors' mechanical property calculation of Tactile Imaging Probe algorithms described in Chapter 3. Here we provide a method to estimate the ranges for depth, size, and stiffness of the tumor.

Fig. 5.1 presents the dataflow diagram for the proposed breast tumor imaging method. We will discuss in length the selected classification methods and the designed models.

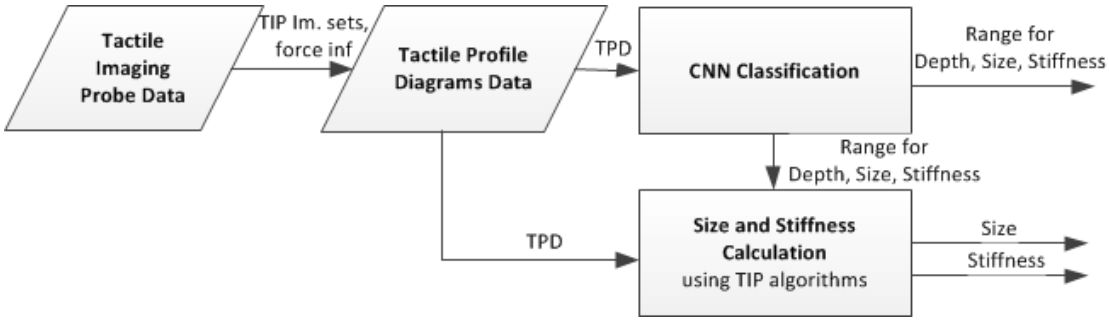

Figure 5.1: Dataflow Diagram for Tactile Imaging Probe

5.1 Classification Methods

Artificial intelligence (AI) is applied to a wide variety of research topics (Goodfellow et al., 2017). It is used in engineering, medicine, and science to improve people's life.

The challenge presented to AI is to solve the problems, which humans can perform, yet found difficult to explain how it was done. The computers' ability to mimic human vision and speech are examples of such problems. The way to enable computers to perform such tasks is to let them learn from the smaller and less complex tasks, which can be easily

described (Goodfellow et al., 2017).

A complex task will include many layers of simpler concepts built and defined one over another. This idea of multiple layers is translated into the concept of AI deep learning (DL). A person uses years and decades of experience and knowledge to complete everyday tasks. This knowledge differs from person to person. It is difficult to express knowledge in a formal way, and it is difficult to teach it to computers. The attempts to define knowledge about the world proved to be very challenging (Lenat and Guha, 1989). On the other hand, machine learning (ML) is a modern tool in AI, which allows computers to learn concepts from data directly.

There are three main types of ML algorithms, depending on the way how they learn: supervised, unsupervised, and reinforced learning. A supervised ML algorithm learns from a data set with labels (annotations), which means the model has input and output for training. Examples of supervise learning algorithms include support vector machines (SVM), k-nearest neighbors (KNN), and decision trees. An unsupervised algorithm learns the feature representation from the data without labels, which means that the model is given only an input. Examples of unsupervised learning algorithms include the principal component analysis (PCA), and k-means clustering. The reinforcement learning algorithm interact with the environment and learns through a rewards system (Goodfellow et al., 2017; Gulli and Pal, 2017).

Simple ML algorithms, such as logistic regression or naive Bayes, are very dependent on the data representation. The data is represented as a set of features. So the choice of features influence the results of the algorithms and is somewhat subjective. While it may be easy to create a set of features for one application, it may be challenging for others. It is possible to use ML to discover the feature representation for a given task. This concept is called representation learning, and it currently outperforms the manual feature learning (Goodfellow et al., 2017).

Some of the algorithms were inspired by our knowledge about living systems. For example, artificial neural network algorithms were designed to mirror brain structure and functions to learn. The network systems are the combinations of layers, where each layer composed of multiple nodes (neurons). The neurons transmit information ("fire") if the

given condition is met (Gulli and Pal, 2017). Autoencoders are successful neural network algorithms, which rely on representation learning. One of the main goals in the design of these algorithms is to be able to explain the factors of variation within the data, yet it is not always easy to do.

In recent years, this problem with explaining variations within data is solved by introducing deep learning. Deep learning algorithms were inspired by neural networks, and are able to represent complex concepts as sets of simple representations presented in multiple layers. Fig. 5.2 explains the way how deep learning represents an image of a person in simple concepts. The DL system learned edges in the image first, then the corners and contours were learned based on the edges. Next, the object parts were learned based on the previous knowledge of corners and edges. Finally, the object on the picture was classified as a person.

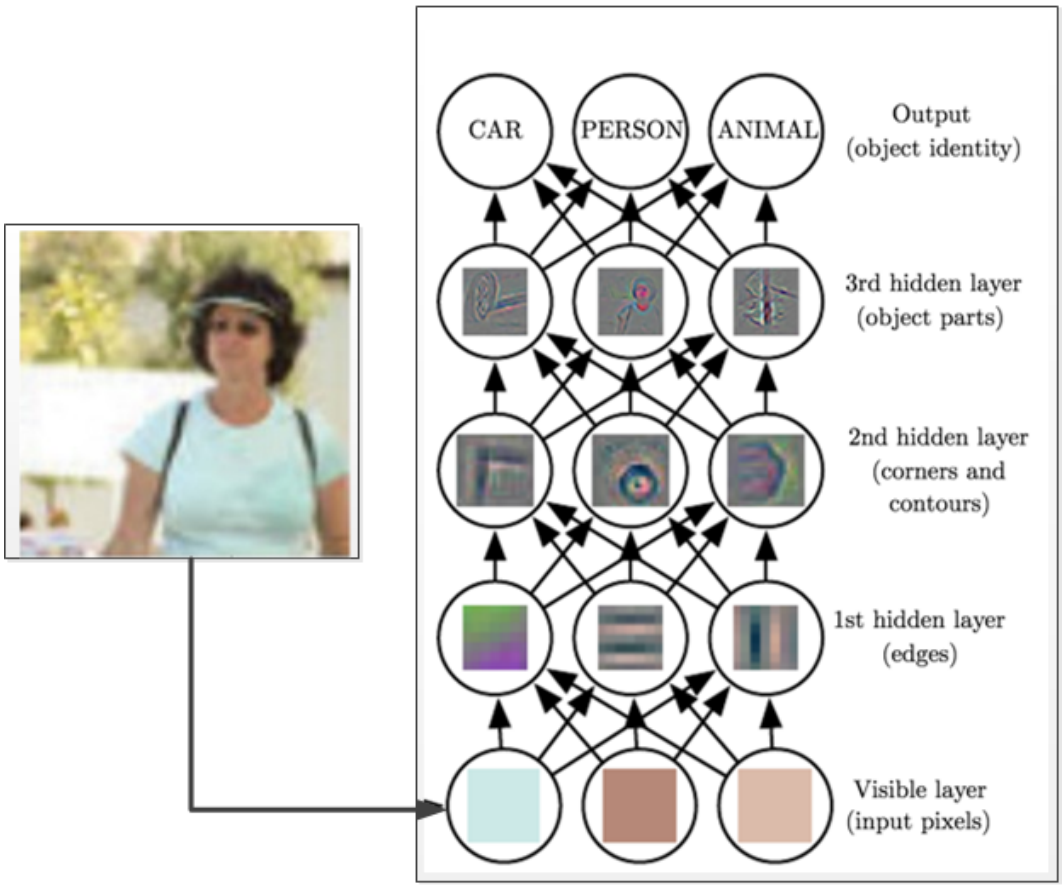

Figure 5.2: DL representation (Goodfellow et al., 2017)

5.1.1 Convolutional Neural Network (CNN) Classification

Convolutional Neural Network (CNN) is a special type of neural network designed to work with the data presented in grids: time-series (1D data), and images (2D data) (Goodfellow et al., 2017; Lecun, 1989). CNN is a neural network that uses convolution operation instead of matrix multiplication in at least one of its layers (Goodfellow et al., 2017).

The structure of the network was inspired by the visual cortex hierarchy and presented by Fukushima (Fukushima, 1980). Since then, it was applied for visual object recognition and image classification tasks with good performance (Jiao et al., 2016).

One CNN layer usually contains three steps to complete. The first step is convolution, which produces a set of linear activations. Followed by the detection (perception) step, where the linear activations are combined with nonlinear activation functions. Finally, the pooling step makes the output invariant to small translations (Goodfellow et al., 2017).

Convolution

To introduce the idea of convolution, let us introduce a sensor system for an airplane location. The sensor system will have the output $x(t)$, which is the location of the airplane in time t. Both x and t are real values. We can have the value of x at any time t.

To reduce the amount of noise in the sensor output, we would like to compute a weighted average of several output values. We would like to give higher weights to the later readings in the sequence of samples. This can be done if we apply a weight function $w(a)$ at each instance of time, where a represents the age of the measurement. The calculated s function (5.1) will correspond to the clean sensor's output and is called convolution.

$$s(t) = \int x(a)w(t-a)da = (x*w)(t). \tag{5.1}$$

The convolution operation is used not only to implement the weighted average, yet has many other uses. In CNN, the first argument ($x(t)$) is called input, and the second argument (w) is called a kernel. The output is called a feature map.

Computers are not capable of processing continuous data; therefore we need to define

the discrete convolution function (5.2)

$$s(t) = \sum_{a=-\infty}^{\infty} x(a)w(t-a)da = (x*w)(t). \tag{5.2}$$

When we want to apply convolution to an image I, we need to use a two-dimensional kernel K as well. The two-dimensional convolution will look as follows.

$$S(i,j) = \sum_m \sum_n I(m,n)K(i-m, j-n) = (I*K)(i,j). \tag{5.3}$$

The commutative property of convolution allows us to write the following.

$$S(i,j) = \sum_m \sum_n I(i-m, j-n)K(m,n) = (K*I)(i,j). \tag{5.4}$$

Very often in CNN implementation cross-correlation is used instead of convolution (5.5). Cross-correlation is the same as convolution but does not involve flipping of the kernel (Goodfellow et al., 2017).

$$S(i,j) = \sum_m \sum_n I(i+m, j+n)K(m,n) = (K*I)(i,j). \tag{5.5}$$

Fig. 5.3 demonstrates the convolution operation via cross-correlation.

Applying convolution to an image creates a map of features of that image. Some types of input image transformations, such as scale or rotation, will not be adequately handled by convolution (Goodfellow et al., 2017). Therefore, the augmentation of training data can improve the performance of a CNN model.

Detection

Detection is done by using a detection algorithm on the output of a convolution step. The detection functions are also called activations.

Perceptron. The most simple detector is the perceptron. It has two possible outputs: yes (1) or no (0), and can be defined as follows (Gulli and Pal, 2017).

$$f(x) = \begin{cases} 1 & wx+b > 0 \\ 0 & otherwise \end{cases} \tag{5.6}$$

were w are weights, b is bias, and wx is the dot product $\sum_{j=1}^{m} w_j x_j$.

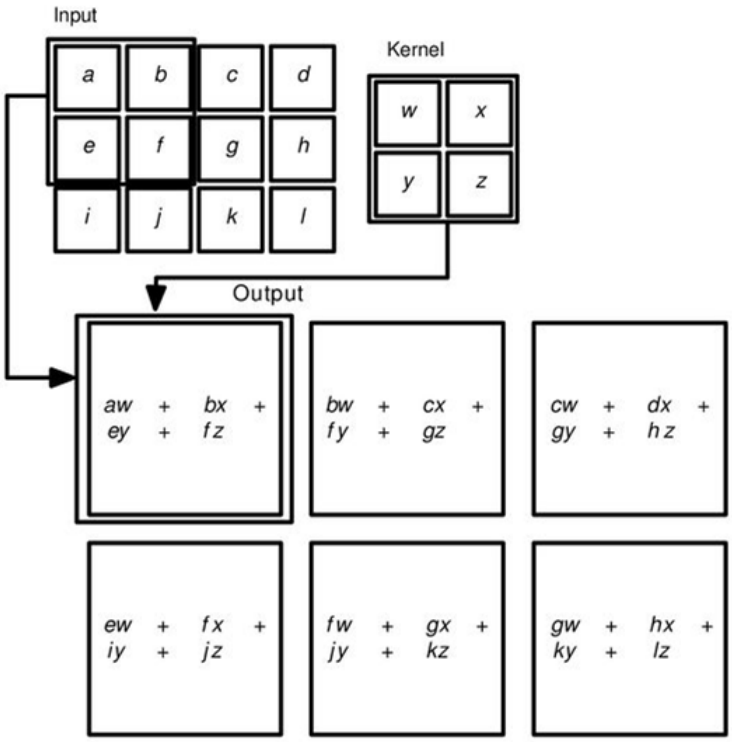

Figure 5.3: Convolution operation via cross-correlation (Goodfellow et al., 2017)

Unfortunately, the perceptron algorithm has serious flaws. It does not allow for a neuron to learn gradually, only with sharp changes. Therefore other activation functions were introduced.

Sigmoid. The sigmoid activation function defined as

$$\sigma(x) = \frac{1}{1+e^{-x}}. \tag{5.7}$$

The function is continuous and gives the neuron ability to learn in tiny steps (Gulli and Pal, 2017).

Hyperbolic Tangent. Similar to sigmoid function is the tanh activation, which is defined as

$$f(x) = tanh(x). \tag{5.8}$$

ReLU. Another activation function is called a rectified linear unit (ReLU). It gained a great popularity in recent years due to its practical compatibility with different applications.

ReLU is defined as

$$f(x) = max(0,x). \tag{5.9}$$

Leaky ReLU. The leaky rectified linear unit (Leaky ReLU) is a modification of ReLU, yet Leaky ReLUs allows small learning when the neuron is not activated. Leaky ReLU is defined as

$$f(x) = \begin{cases} x & x > 0 \\ ax & otherwise \end{cases} \tag{5.10}$$

were a is the slope parameter.

ELU. Another modifications to the linear rectified unit function is the exponential linear unit (ELU) (Clevert et al., 2016).

$$f(x) = \begin{cases} x & x > 0 \\ a(e^x - 1) & otherwise \end{cases} \tag{5.11}$$

were a is a hyper-parameter to be tuned.

All of the discussed activation functions are plotted in Fig. 5.4.

Pooling

Pooling is an essential part of a CNN model, which was inspired by the complex structure of brain visual cortex cells (Jiao et al., 2016). Small translational variations (shifts of pixels) in the input image can be compensated by using pooling. It allows us to find a particular feature on the image without caring much where precisely the feature is on the image (Goodfellow et al., 2017).

A pooling replaces the feature map pixels with the generalized neighboring pixel statistics (Goodfellow et al., 2017). There are many ways to implement pooling, yet the most common is the max pooling, which replaces the pixel value on the feature map with the maximum pixel value of its neighboring pixels (Zhou and Chellappa, 1988). Fig. 5.5 illustrates how the max pooling works.

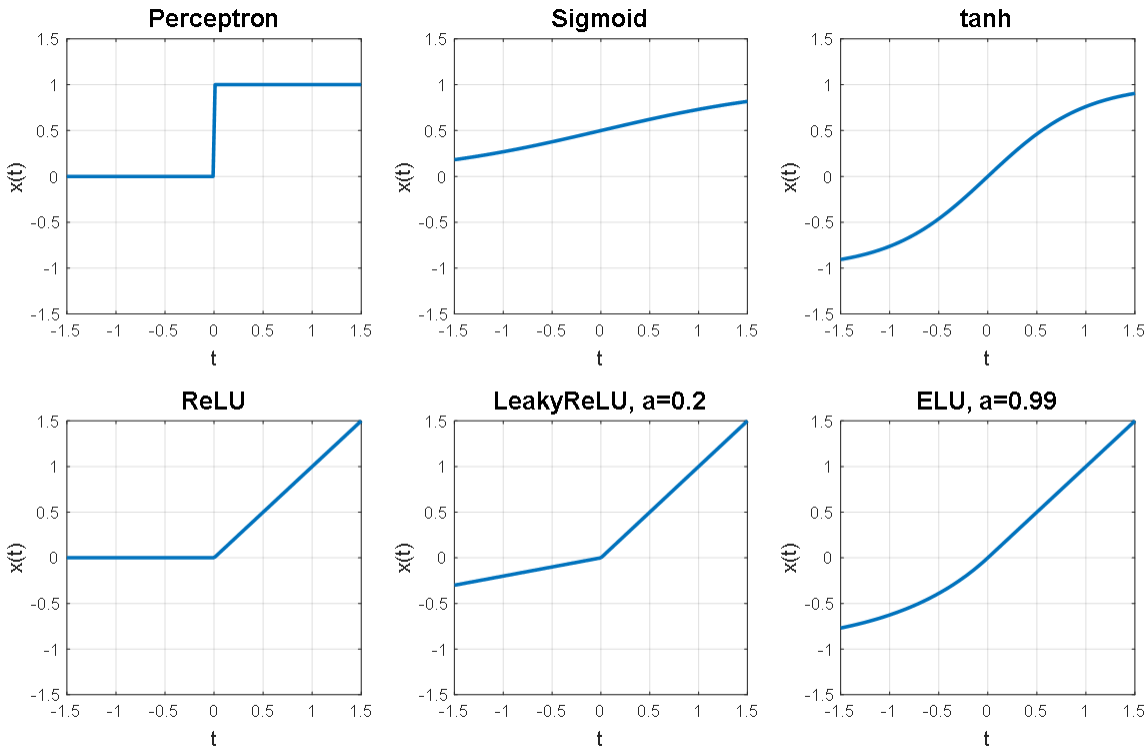

Figure 5.4: Common activation functions

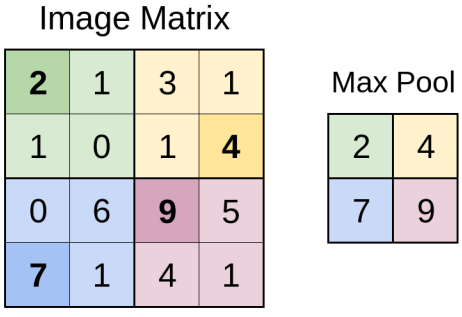

Figure 5.5: Convolution operation via cross-correlation (Walters, 2019)

Model Compilation

There are three main steps required to compile a CNN model (Gulli and Pal, 2017). All three of them are briefly summarized here.

Optimization

The optimizer is an algorithm used to update the model training weights. The most common algorithm used for optimization is the gradient descent algorithm (Gulli and Pal, 2017).

A large amount of training data is necessary for good generalization of deep learning. Therefore, DL heavily relays on the fast version of the gradient descent algorithm - the stochastic gradient descent algorithm (SGD), to be able to process a large amount of data (Goodfellow et al., 2017).

There are several more commonly used optimizers, which are: adam and adamax optimizers introduced by Kingma (Kingma and Ba, 2015), as well as RMSprop (Gulli and Pal, 2017).

Objective function

The objective functions or loss functions are used by optimizers with the goal of minimization of the loss during the weights update (Gulli and Pal, 2017). The most commonly used objective functions are the following.

MSE optimizer uses the mean square error calculation between the prediction and the true value. The function is expressed as following (Gulli and Pal, 2017).

$$MSE = \frac{1}{n}\sum_{i=1}^{n}(\gamma - Y)^2. \tag{5.12}$$

were γ is a vector of n predictions, and Y is the vector of n observations.

The binary cross-entropy optimizer employs the logarithmic function and is used in binary label prediction (Gulli and Pal, 2017).

The categorical cross-entropy optimizer is a logarithmic loss for multiple classes. The optimization is used for the multiclass classification, and described as follows (Gulli and Pal, 2017).

$$L_i = \Sigma_j t_{i,j} log(p_{i,j}) \tag{5.13}$$

were $t_{i,j}$ is the target, and $p_{i,j}$ are predictions.

Model Evaluation

After a CNN model is compiled, it has to be evaluated. There are several common evaluation metrics: recall, precision, and accuracy (Gulli and Pal, 2017).

Recall is the number of correct positive predictions divided by the number of all samples that had to be positive.

Precision is the number of correct positive predictions divided by the number of positive predictions by the classifier.

Accuracy is defined as the total number of the correct predictions to the total number of the given predictions.

5.2 Classification of Tactile Profile Diagrams

Classification of Tactile Profile Diagrams, which are the one-image representations of multiple TIP imaging sessions, designed to extract the tumor's depth, size, and stiffness information. Classification of the tactile imaging data can help to characterize the mechanical properties of tumors and to distinguish malignant from benign ones (Egorov et al., 2009).

In this work, we will use several CNN models to classify imaged tumors first on two classes, depending on their depth (deep or shallow tumors), then on six classes, depending on their size and stiffness (small and soft, small and less stiff, small and stiff, large and soft, large and less stiff, and large and stiff tumors). Further, these classification results will aid tumors' size and stiffness calculations with TIP algorithms without input estimations. Fig. 5.6 presents the described TPD classification steps.

5.2.1 CNN Model for Depth Evaluation

Because the tumor's depth estimation is important for its accurate size and stiffness estimation (Oleksyuk et al., 2018), we propose to use the CNN Model1 to evaluate the depth of the tumor prior to other steps.

We designed the CNN sequential model, which does not have a feedback loop, with three convolution, three max pooling layers, and activation functions for the feature learn-

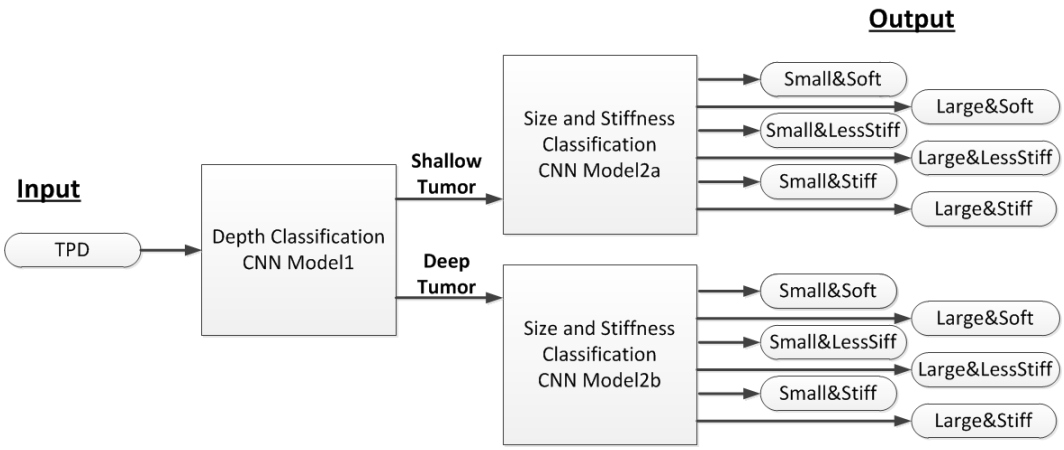

Figure 5.6: TPD classification steps

ing part. The classification part of the model includes four dense layers with different activation functions. The final fully connected layer has two nodes, corresponding to the shallow or deep classes. The model designed as a binary classifier to distinguish shallow and deep tumors. With the appropriate training data and the modiïňĄed ïňĄnal layer can output multiple depth ranges (classes) if required by the application. Fig. 5.7 shows the structure of the depth classification model (CNN Model1). The details on the model are given in Fig. 5.8.

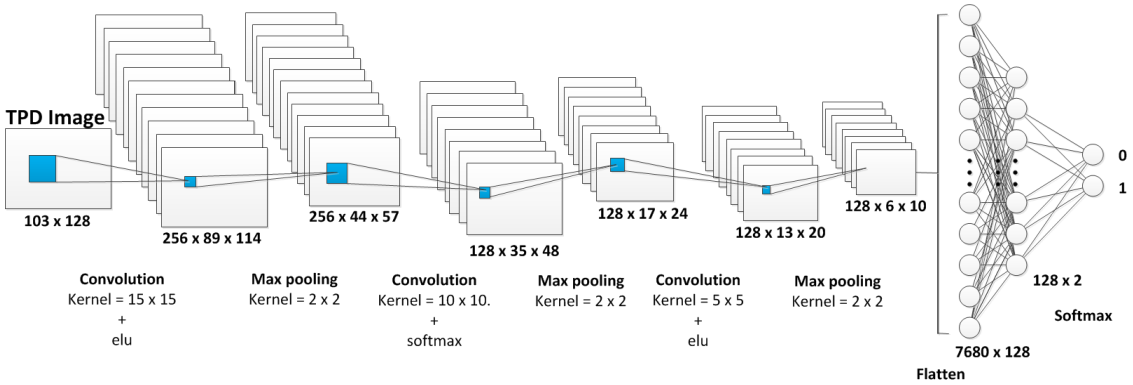

Figure 5.7: TPD depth classification model (CNN Model1) (Patel, 2019)

5.2.2 CNN Models for Size and Stiffness Evaluation

After the depth evaluation, we use another two CNN models to classify the tumor's size and stiffness: Model2a and CNN Model2b. The two models have the same structure (Fig. 5.9).

Layer (type)	Output Shape	Parameters #
conv2d (Conv2D)	(None, 89, 114, 256)	57856
activation (elu)	(None, 89, 114, 256)	0
max_pooling2d (MaxPooling2D)	(None, 44, 57, 256)	0
conv2d_1 (Conv2D)	(None, 35, 48, 128)	3276928
activation_1 (elu)	(None, 35, 48, 128)	0
max_pooling2d_1 (MaxPooling2)	(None, 17, 24, 128)	0
conv2d_2 (Conv2D)	(None, 13, 20, 128)	409728
activation_2 (elu)	(None, 13, 20, 128)	0
max_pooling2d_2 (MaxPooling2)	(None, 6, 10, 128)	0
flatten (Flatten)	(None, 7680)	0
dropout (0.3)	(None, 7680)	0
dense (Dense)	(None, 128)	983168
activation_3 (ReLU)	(None, 128)	0
dropout_1 (0.3)	(None, 128)	0
dense_1 (Dense)	(None, 128)	16512
activation_4 (elu)	(None, 128)	0
dropout_2 (0.3)	(None, 128)	0
dense_2 (Dense)	(None, 128)	16512
activation_5 (elu)	(None, 128)	0
dropout_3 (0.3)	(None, 128)	0
dense_3 (Dense)	(None, 2)	258
activation_6 (softmax)	(None, 2)	0

Total params: 4,760,962

Trainable params: 4,760,962

Non-trainable params: 0

Figure 5.8: CNN Model1 details

However, these models will be trained on different data. The CNN Model2a, designed to classify shallow tumors, will be trained on the training subset of shallow tumors (0 - 10 mm in depth). The CNN Model2b, designed to classify deep tumors, will be trained on the training subset of deep tumors (>10 mm in depth). The details on the model are given in Fig. 5.10.

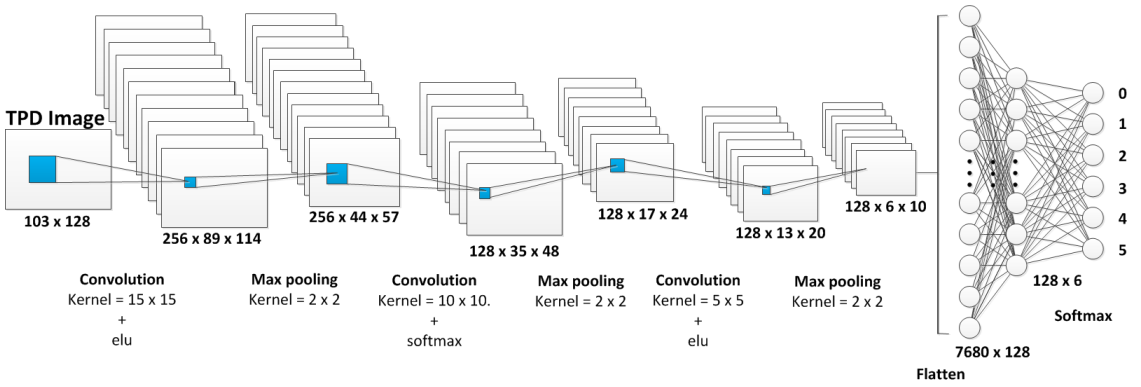

Figure 5.9: TPD Size and Stiffness Classification Model(CNN Model2) (Patel, 2019)

5.3 Classification of Multispectral Profile Diagrams

We propose to use CNN classification models to classify and quantify the differential parameters from Multispectral Profile Diagrams (MPD). Figure 5.11 shows the steps we will perform during the MPD classification.

To classify MPDs, we will develop a CNN model for each of the four differential parameters: differential color change (Yes or No), differential texture change (Yes or No), differential reddened area (Small or Large), and differential asymmetry (Small or Large). Each of the classes will include their corresponding prediction value.

We propose to develop the CNN models similar in design to the CNN models for TPD classification described earlier, yet make them better adjusted to the specifics of the Multispectral Profile Diagrams. Fig. 5.12 presents the proposed model description.

We will further use the probabilities of each differential parameter to construct the Multispectral Imaging Probe Index.

Layer (type)	Output Shape	Parameters #
conv2d (Conv2D)	(None, 89, 114, 256)	57856
activation (elu)	(None, 89, 114, 256)	0
max_pooling2d (MaxPooling2D)	(None, 44, 57, 256)	0
conv2d_1 (Conv2D)	(None, 35, 48, 128)	3276928
activation_1 (elu)	(None, 35, 48, 128)	0
max_pooling2d_1 (MaxPooling2)	(None, 17, 24, 128)	0
conv2d_2 (Conv2D)	(None, 13, 20, 128)	409728
activation_2 (elu)	(None, 13, 20, 128)	0
max_pooling2d_2 (MaxPooling2)	(None, 6, 10, 128)	0
flatten (Flatten)	(None, 7680)	0
dropout (0.3)	(None, 7680)	0
dense (Dense)	(None, 128)	983168
activation_3 (ReLU)	(None, 128)	0
dropout_1 (0.3)	(None, 128)	0
dense_1 (Dense)	(None, 128)	16512
activation_4 (elu)	(None, 128)	0
dropout_2 (0.3)	(None, 128)	0
dense_2 (Dense)	(None, 128)	16512
activation_5 (elu)	(None, 128)	0
dropout_3 (0.3)	(None, 128)	0
dense_3 (Dense)	(None, 6)	774
activation_6 (softmax)	(None, 6)	0

Total params: 4,761,478

Trainable params: 4,761,478

Non-trainable params: 0

Figure 5.10: CNN Model2 details

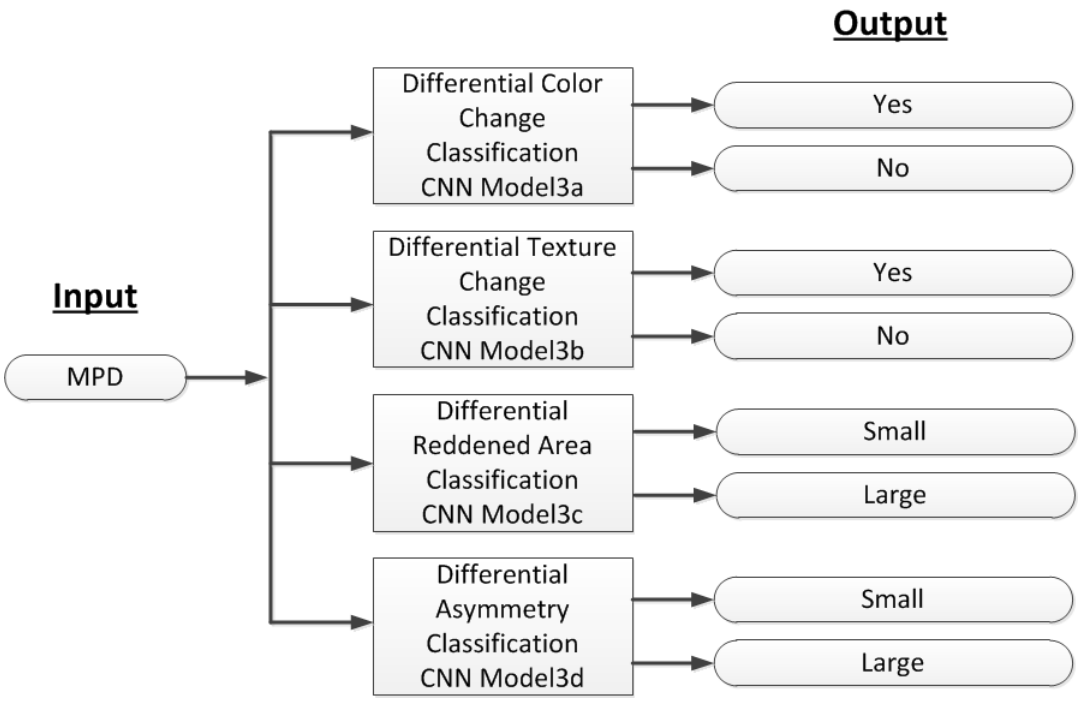

Figure 5.11: MPD classification steps

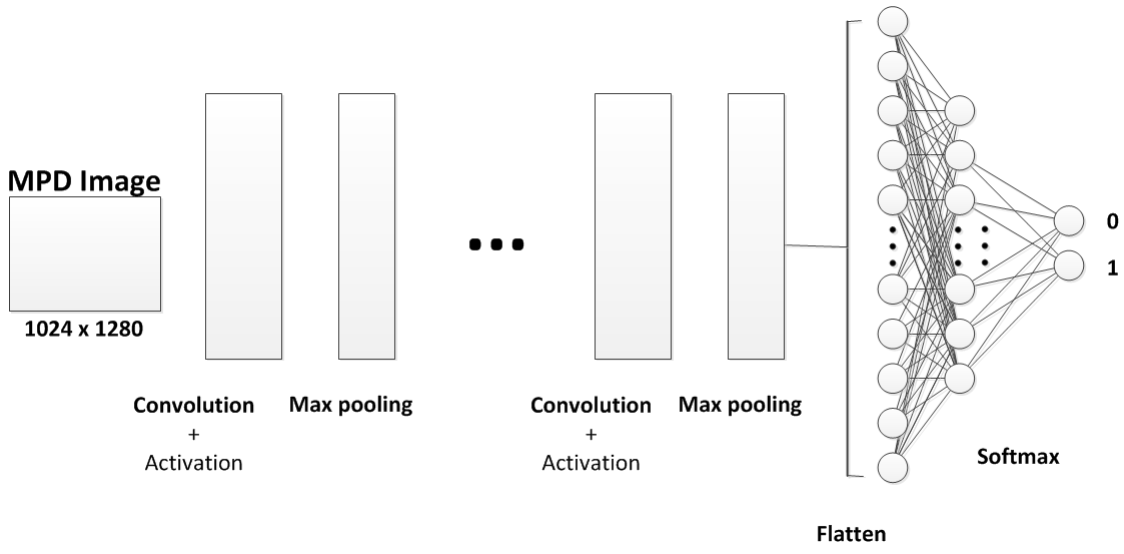

Figure 5.12: MPD differential parameters classification model (CNN Model3)

5.4 Discussion

In this chapter, we present an overview of the most popular machine learning classification methods with the emphasis on the Convolutional Neural Network. Then, we described the main model components of a CNN model. Later, we proposed the method to classify Tactile Profile Diagrams with CNN to learn the ranges for breast tumor depth, size, and stiffness, as well as the corresponding prediction values. Finally, we outlined CNN classification of Multispectral Profile Diagrams to evaluate the differential parameters as the superficial optical properties of breast tissue associated with malignancy development.

CHAPTER 6

RISK SCORE

In this chapter, we develop a method to evaluate the probability of malignancy for the imaged breast tissue with a tumor. We describe how to use the acquisition data from both imaging modalities of our system: the Tactile Imaging Probe and the Multispectral Imaging Probe, and how to combine it with the Breast Cancer Risk Assessment Tool (BCRAT) developed by National Cancer Institute, to calculate the Combined Malignancy Risk Score for a patient.

6.1 Review of the Malignancy Risk Score Calculations

Machine learning shows great potential in supporting doctors during clinical diagnostic procedures (Yadav et al., 2019). It is more robust, capable, and better individualized, so it outperforms the well established, manually developed empirical malignancy risk scoring models. It gives additional possibilities for the modern movement towards the individualized cancer risk assessment (Ming et al., 2019)

Accurate predictions on who will develop breast cancer are not available; however, there are several well-known malignancy risk assessment methods (Yadav et al., 2019). The methods help patients and doctors to develop a custom breast diagnostic plan, or even schedule a preventive surgery.

The Gail model (Gail et al., 1989) is the most popular tool for the five and ten year cancer development risk assessment based on a short questionnaire that women complete with their doctors.

The Claus model (Claus et al., 1994) gives age-specific risk probability of breast cancer for women with a family history of breast cancer.

The Tyrer-Cuzick model (Tyrer et al., 2004) tool assesses breast 10 year malignancy risk based on a woman's answers to a series of questions.

6.2 Tactile Imaging Probe Scoring Parameter

Recently, researchers pointed their attention to the capabilities of Convolutional Neural Network to extract the unknown before features from medical images, to calculate malignancy risk score, and aid radiologists on diagnostic decisions (Kallenberg et al., 2016; Heinemann et al., 2019). During CNN classification, the class assignment is based on the probabilities calculated for each of the classes. The empirical probabilities signify how confident the class decision is, and it can be used for the malignancy score calculation in cancer applications.

We propose to calculate the TIP Index, $Index_{TIP}$, as the weighted average of the CNN Model2 probability assignments for the main tactile imaging features: size and stiffness, as follows.

$$Index_{TIP} = \alpha_1 P_{11} + \alpha_2 P_{12}, \tag{6.1}$$

were P_{11} corresponds to the normalized probability of the tumor's size, and P_{12} corresponds to the normalized probability of the tumor's stiffness from CNN Model2. α_1 and α_2 are the corresponding weights for size and stiffness probabilities, respectively.

We will have to complete research on the distribution of the proper weights to obtain useful and clinically meaningful results for patients (Aydiner et al., 2017).

6.3 Multispectral Imaging Modality IBC Scoring Parameter

We propose to calculate the Multispectral Imaging Probe index, $Index_{MIP}$, using the four multispectral imaging parameters associated with breast cancer and their probabilities obtained from CNN Model3. Eq. (6.2) shows $Index_{MIP}$ calculation.

$$Index_{MIP} = \beta_1 P_{21} + \beta_2 P_{22} + \beta_3 P_{23} + \beta_4 P_{24}, \tag{6.2}$$

were P_{21} corresponds to the normalized probability of the differential color parameter, and P_{22} corresponds to the normalized probability of the differential texture parameter, P_{23} corresponds to the normalized probability of the differential reddened area parameter, and P_{24} corresponds to the normalized probability of the differential asymmetry from CNN

Model3. β_1, β_2, β_3, and β_4 are the corresponding weights for the differential color, texture, reddened area and asymmetry probabilities respectively.

Here, we also will have to complete research on clinically meaningful weights distribution (Aydiner et al., 2017).

6.4 Health Assessment Parameter from Medical Health Records

The National Cancer Institute made the Breast Cancer Risk Assessment Tool (BCRAT) publicly available online to calculate individual risk of developing malignancy(National Cancer Institute, 1999). The scoring is largely based on the well known Gail model (Gail et al., 1989), which was further developed by Costantino in 1999 (Costantino et al., 1999). Doctors and medical residents are currently encouraged to use the tool in their practice (Yadav et al., 2019).

BCRAT provides an online calculator, where women can enter their information (Fig. 6.1) and receive the predictions for developing breast cancer in five and in ten years in the future (Fig. 6.2). The women with higher than average risk are suggested to talk to their primary care physicians on developing an individualized diagnostic plan.

We will incorporate the BCRAT Score into the Combined Risk Score as the individualized health index, $Index_{Health}$. Eq. (6.3) shows the index calculation.

$$Index_{Health} = \gamma_1 P_{31}, \tag{6.3}$$

were P_{31} corresponds to the 5-year probability from BCRAT, γ_1 is the weight of the probability in our calculation.

6.5 Combined Malignancy Risk Score Computation

To calculate the Combined Malignancy Risk Score, we propose to compute the weighted sum of $Index_{TIP}$, $Index_{MIP}$, and $Index_{Health}$ as follows.

$$Score = w_1 Index_{TIP} + w_2 Index_{MIP} + w_3 Index_{Health}, \tag{6.4}$$

were w_1, w_2, and w_3 are the weights of the corresponding indexes.

1. Does the woman have a medical history of any breast cancer or of ductal carcinoma in situ (DCIS) or lobular carcinoma in situ (LCIS) or has she received previous radiation therapy to the chest for treatment of Hodgkin lymphoma?
2. Does the woman have a mutation in either the *BRCA1* or *BRCA2* gene, or a diagnosis of a genetic syndrome that may be associated with elevated risk of breast cancer?
3. What is the patient's age?
4. What is the patient's race/ethnicity?
   a. What is the sub race/ethnicity or place of birth?
5. Has the woman ever had a breast biopsy?
   a. How many breast biopsies (positive or negative) has the woman had?
   b. Has the woman ever had a breast biopsy with atypical hyperplasia?
6. What was the woman's age at the time of her first menstrual period?
7. What was the woman's age when she gave birth to her first child?
8. How many of the woman's first-degree relatives (mother, sisters, daughters) have had breast cancer?

Figure 6.1: The BCRAT Calculator Questions (National Cancer Institute, 1999)

5–Year Risk of Developing Breast Cancer

Patient Risk	Average Risk
0.4%	**0.3%**

Lifetime Risk of Developing Breast Cancer

Patient Risk	Average Risk
10.4%	**12.6%**

Figure 6.2: The BCRAT Calculator Results (National Cancer Institute, 1999)

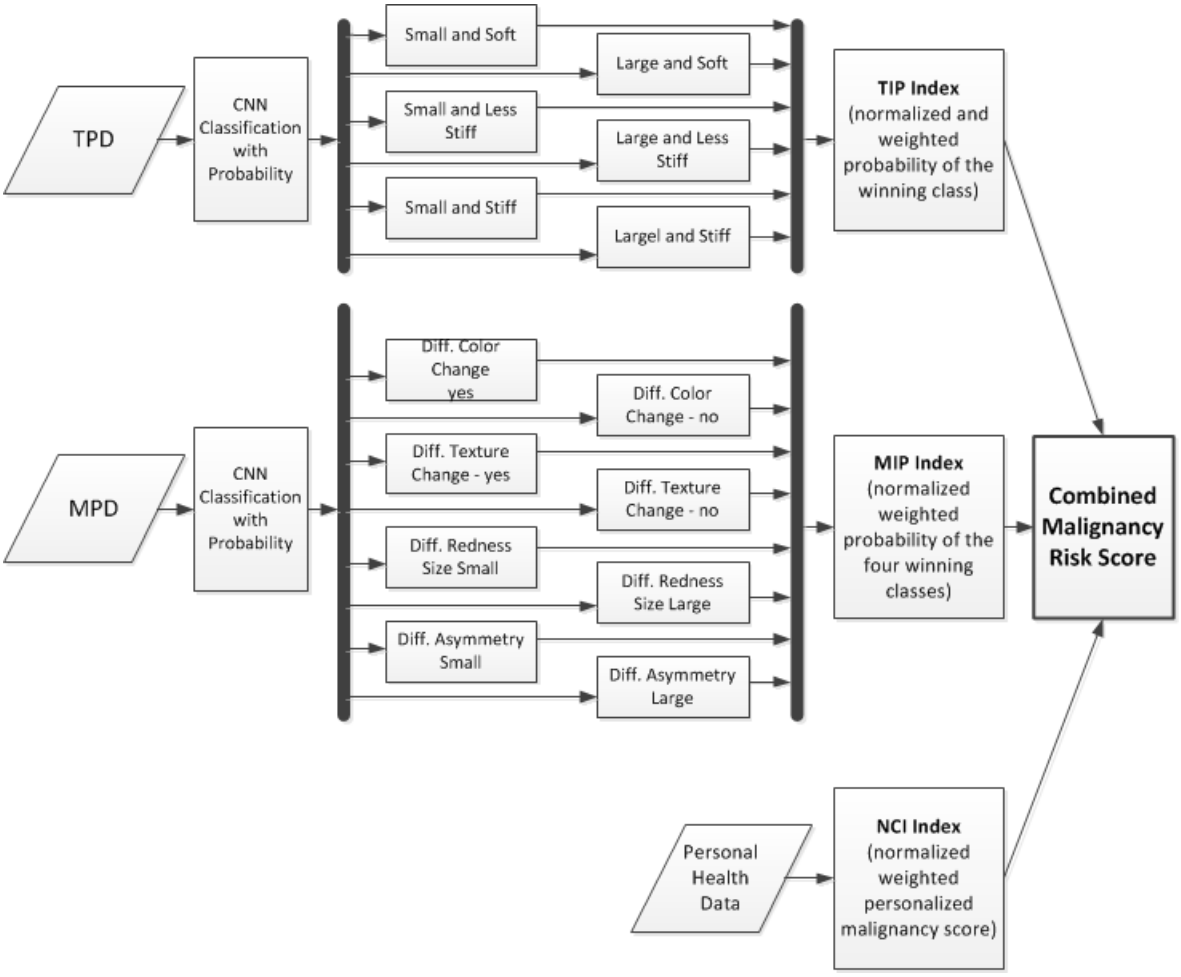

Figure 6.3: Combined Malignancy Risk Score development

Fig. 6.3 shows the block diagram for the Combined Malignancy Risk Score calculation.

The Combined Malignancy Risk score will range from 0 to 1. The values closer to zero will correspond to the probability of the tissue with a tumor to be benign, and the values closer to 1 will signify the higher probability of malignancy.

6.6 Discussion

In this chapter, we derived the method to calculate the Combined Malignancy Risk Score for breast tissue using the probabilities of the key features from Tactile Imaging Probe and Multispectral Imaging Probe, as well as the probability of malignancy based on the patient's health records from the Breast Cancer Risk Assessment Tool (National Cancer Institute, 1999). We want to use CNN's data mining capabilities to extract the probabilities associated with the features from each modality and to use it for the individualized malignancy risk assessment.

CHAPTER 7

TACTILE IMAGING PROBE EXPERIMENT

In this chapter, we describe the Tactile Imaging Probe experiments. We also outline the development of breast tissue and tumor phantoms. We will present the preliminary experimental results. We will also show the preliminary classification performance of the Convolutional Neural Network models, which classify the imaged tumors.

7.1 Tactile Imaging Phantom

Here we outline the development of the breast tissue mimicking phantom. The phantom is necessary to test the capabilities of the Tactile Imaging Probe.

7.1.1 Review of Phantoms that Mimic Mechanical Properties of Tissues

The Tactile Imaging Probe experiments require custom breast tissue mimicking phantom. Multiple studies have been done on developing tissue-like artificial breast phantoms (Lamouche et al., 2012; Boehm et al., 2001; Grand et al., 2008; Giller et al., 2003; Choe, 2005; Hebden et al., 2006; Sallaway et al., 2014; Mourant et al., 1997). The phantoms were made from different types of materials, which are inorganic or organic by nature. The most commonly used materials for mechanical phantoms are gelatin, agar, fibrin, Polydymethyl siloxane, Polyvinyl chloride, and Polydymethyl alcohol (PVA) silicones.

Not many of the mechanical property tissue phantoms incorporate tumors within the synthetic tissue. Researchers who work in breast cancer research, develop phantoms with tissue inclusions. Egorov and Sarvazyan fabricate a SEMICOSIL hydrogel tissue and tumor mimicking phantom (Egorov and Sarvazyan, 2008). The inclusions had varying sizes, yet constant stiffness.

Polyvinyl chloride (PVC) and Polydimethyl siloxane (PDMS) phantoms are well suited for mechanical property estimation experiments (Lee and Won, 2013; Sahu et al., 2014; Oleksyuk et al., 2018). In this work, we developed a phantom with tissue-like mechanical

characteristics and with embedded inclusions using PDMS plastisol. The phantom composed of multiple layers and is durable even with repeated mechanical compressions. It includes palpable PDMS inclusions of variable depth, stiffness, and size.

7.1.2 Phantom Proposed Design

The proposed mechanical property breast tissue phantom is composed of multiple layers. The base material of the tissue layers is Polydimethyl siloxane (PDMS) due to its safety and easiness to use, adjustable stiffness, and high tolerance to heat and mechanical compressions. Polydimethyl siloxane is a commercially available silicone rubber. It is composed of two materials: Base agent (A) and Curing Agent (B). We used RTV 6136-D1 (Momentive Performance Materials, Waterford, NY), a low viscosity silicone dielectric gel, to prepare PDMS. Two components A and B were mixed in a different mixing ratio by weight.

We developed four types of tissue layers using PDMS: base, intermediate, depth, and skin layers. The spherical tumors are manually cut out of cured PDMS cubes with a range of stiffness. Figure 7.1 shows the schematics of the phantom and its layers. The description of each layer is also provided on the figure.

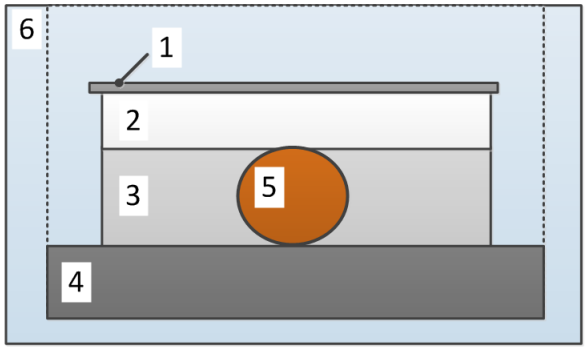

1. Protective top layer	PVC	78 kPa
2. Depth layer	PDMS 1:2 Ratio	94 kPa
3. Intermediate layer	PDMS 1:2 Ratio	94 kPa
4. Base layer	PDMS 1:20 Ratio	629 kPa
5. Tumor Phantom	PDMS Ratios	130 kPa ... 629 kPa
6. Pyrex glass container		

Figure 7.1: Breast phantom for TIP experiments

The base layer is a supportive layer, which mimics ribs and muscles under breast tissues.

The PDMS ratios (A:B components) of the layer is 1:20 (629 kPa). Intermediate layers of different thickness (10 mm, 12 mm, 14 mm, 16 mm and 18 mm) are developed to embed the tumors of different diameter (10 mm, 12 mm, 14 mm, 16 mm and 18 mm). PDMS ratio of the intermediate layer is 1:2 (94 kPa). Depth layers are made of PDMS ratio 1:2 (94 kPa) to vary the depth of the embedded tumors. Depths layers' thicknesses are the following: 2 mm, 4 mm, 6 mm, 8 mm, 10 mm, 12 mm, and 14 mm. The skin layer is a thin ($<$ 1 mm) and transparent PVC layer 78 kPa. It serves as a protective layer for compression experiments.

The PDMS ratios (A:B components) of the tumors are the following: 1:2.5, 1:3, 1:3.5, 1:4, 1:4.5, 1:5, 1:5.5, 1:6; 1:7, 1:8, 1:9, 1:10, 1:12.5, 1:15; 1:17.5, 1:20. These PDMS mixing ratios are covering Young's Modulus range from approximately 130 kPa to 629 kPa.

All of Young's moduli of the PDMS samples were obtained using the compression technique with the Instron 5944 testing machine (Oleksyuk, 2019).

7.2 Phantom Experiment Setup and Results

In this section, we outline the experimental design for Tactile Imaging Probe to test its capabilities and algorithms. The phantom data set, which we obtained by imaging with the phantom described in the previous section, contains thousands of entries. We incorporated in the phantom 5 different tumor sizes (10 mm, 12 mm, 14 mm, 16 mm, and 18 mm), eight tumor depths (0 mm, 2 mm, 4 mm, 6 mm, 8 mm, 10 mm, 12 mm, and 14 mm), and 17 PDMS ratios of component B to vary the tumor stiffness (2.5, 3, 3.5, 4, 4.5, 5, 5.5, 6, 7, 8, 9, 10, 12.5, 15, 15.5, 20, plastic ball). We completed the imaging for each combination of the three aforementioned properties, with 13 to 20 trials for slight hand displacement. This data set was used for Tactile Profile Diagrams development and classification.

However, for some of the following preliminary results, we used earlier developed phantoms. The phantoms and the data sets for these experiments will be described together with the results from these experiments.

In our earlier work (Oleksyuk et al., 2018), we estimated the size and stiffness of tumors

directly from the sets of raw TIP images. Recently, we decided to consolidate the tactile properties of tissues from TIP imaging sets into Tactile Profile Diagrams. We later learned that size, stiffness, and depth estimation from TPD with CNN classification leads to better tumor size and stiffness calculations. Additionally, the in-vivo pilot study results are not processed with the latest TPD algorithm and will be completed in the future. Nevertheless, the in-vivo results are presented in this section, as well as the calculation method.

7.2.1 Raw Tactile Images Results

The test objective of this experiment was to determine the depth and size of tumors that TIP can detect. We used different tumor depths (0 mm, 3 mm, 5 mm, 10 mm, 12 mm and 15 mm), and tumor sizes (3 mm, 10 mm, 15 mm and 18 mm) for this experiment. We also used two types of tumor stiffness: softer tumor inclusion (1:3 ratio A:B or 134 kPa) and stiffer tumor inclusion (1:20 ratio A:B or 466 kPa). The inclusions were tested in 2017 using Instron testing machine to determine the true elastic modulus values for the tumor samples.

Polyvinyl chloride (PVC) was used to prepare multiple layers of the breast phantom. There are four layers, namely base, intermediate, depth, and protective layer, as shown in Fig 7.2. The PVC materials we used were "regular liquid plastic," "super-soft liquid plastic," and "softener" (M - F Manufacturing Company Inc., TX, USA). The base layer was made from "regular liquid plastic." The intermediate and depth layers were softer and were made of "regular liquid plastic" plus "softener" with the 1:1 ratio and addition of skin color dye (Flesh Tone Silicone Pigment, Smooth-On Inc.). The thin protective layer made from the "super soft liquid plastic" material.

During the tests, we varied the depth by adding different layers from 0 mm to 23 mm to estimate the maximum depth of the tumor that the TIP can detect. The results of size and stiffness estimation experiments is presented in Table 7.1 and Table 7.2.

Table 7.1: Size and Deformation Index estimation at shallow tumor depths

Tumor inclusion	True Size (mm)	Estimated Size (Mean)	Size Error, (%)	DI (10^4)
Softer	3	8.24	174.78++	3.32
	10	10.77	1.87	5.06
	15	13.56	9.61	12.13
	18	14.74	18.12	25.94
Stiffer	3	8.55	185.51++	3.59
	10	9.50	5.01	8.68
	15	13.92	7.20	15.81
	18	14.95	16.94	29.56
		(a) Depth=0 mm		
Softer	3	8.26	175.40++	2.71*
	10	9.59	13.54	3.57
	15	13.58	9.47	3.25
	18	13.95	22.51	2.53
Stiffer	3	6.07	102.22++	2.07*
	10	8.66	13.35	3.88
	15	12.20	18.70	5.97
	18	14.07	21.83	9.95
		(b) Depth=3 mm		
Softer	3	8.34	178.13++	2.17
	10	9.24	15.97	3.38
	15	13.20	12.03	4.02
	18	13.63	24.27	9.41
Stiffer	3	8.58	186.14++	3.61
	10	8.68	13.15	4.53
	15	11.69	22.10	6.18
	18	13.97	22.41	17.47
		(c) Depth=5 mm		

Table 7.2: Size and Deformation Index estimation at deep tumor depths

Tumor inclusion	True Size (mm)	Estimated Size (Mean)	Size Error, (%)	DI (10^4)
Softer	3	8.37	179.14++	3.38
	10	8.65	24.67	2.26
	15	13.30	11.36	3.09
	18	14.13	21.49	5.97
Stiffer	3	7.93	164.36++	3.80
	10	9.03	9.68	3.50
	15	13.65	8.98	4.36
	18	13.93	22.61	10.60
		(d) Depth=10 mm		
Softer	3	n/a	n/a	2.19
	10	8.95	23.40	3.04
	15	12.99	13.38	2.66
	18	14.78	17.92	3.53
Stiffer	3	n/a	n/a	2.98
	10	9.22	7.77	3.15
	15	14.13	5.78	2.70
	18	14.40	20.03	4.212
		(e) Depth=12 mm		
Softer	3	n/a	n/a	1.88*
	10	8.58	23.97	2.94*
	15	13.77	8.23	2.04
	18	14.73	18.19	3.69
Stiffer	3	n/a	n/a	1.47*
	10	8.84	11.64	2.37*
	15	14.10	5.98	2.98
	18	14.69	18.38	4.60
		(f) Depth=15 mm		

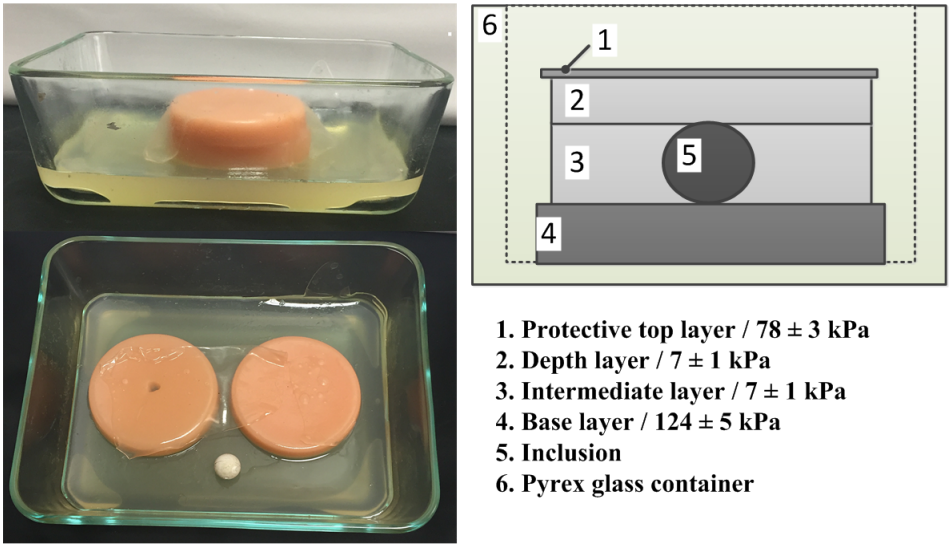

Figure 7.2: Breast phantom for the preliminary experiments

Soft Tumor

At superficial depth (0 mm), the tumor phantom sizes 10 mm, 15 mm, and 18 mm are detected better with a less size error percentage of 1.87%, 9.61%, and 18.12%, respectively. As the depth increased from 0 mm to 15 mm, the size estimation error only increased slightly, which shows the sensitivity of TIP and accuracy of measuring the tumor size in varying depth. The 3 mm size estimation shows a large error, which shows that size detection performance of TIP decreases when the tumor sizes are less than 3 mm.

Stiffer Tumor

The 1:20 samples are stiffer than 1:3; hence theoretically, the 1:20 samples represent malignant tumors, which is considered to be stiffer than benign tumors. The result shows that TIP can determine the size of 1:20 samples more accurately than that of 1:3, and the error is smaller. This shows that TIP is able to detect malignant tumors or stiffer growths over benign or non-stiff tumors. The phantom testing showed that the TIP is able to determine the size of tumors above 3 mm in size up to 18 mm and to a depth of up to 15 mm.

Deformation Index (DI)

The deformation index is calculated in Table 7.1 and Table 7.2. Comparing the same size tumors at the same depth between the softer and stiffer tumors, we note that the values

follow a similar pattern as explained above. The stiffer samples show a higher deformation index than the softer samples. At the depth of 15 mm, a small sized-tumor showed a large error due to the difficulties in detecting deeply embedded tumors.

7.2.2 Tactile Profile Diagrams Results

Tactile Profile Diagram (TPD) is a representative pattern image of a TIP image set and a pictorial representation of relative stiffness and size of the tumor. Therefore we hypothesize that it is possible to estimate size and stiffness of tumors from their corresponding TPDs.

Figure 7.3 shows examples of contracted TPD images.

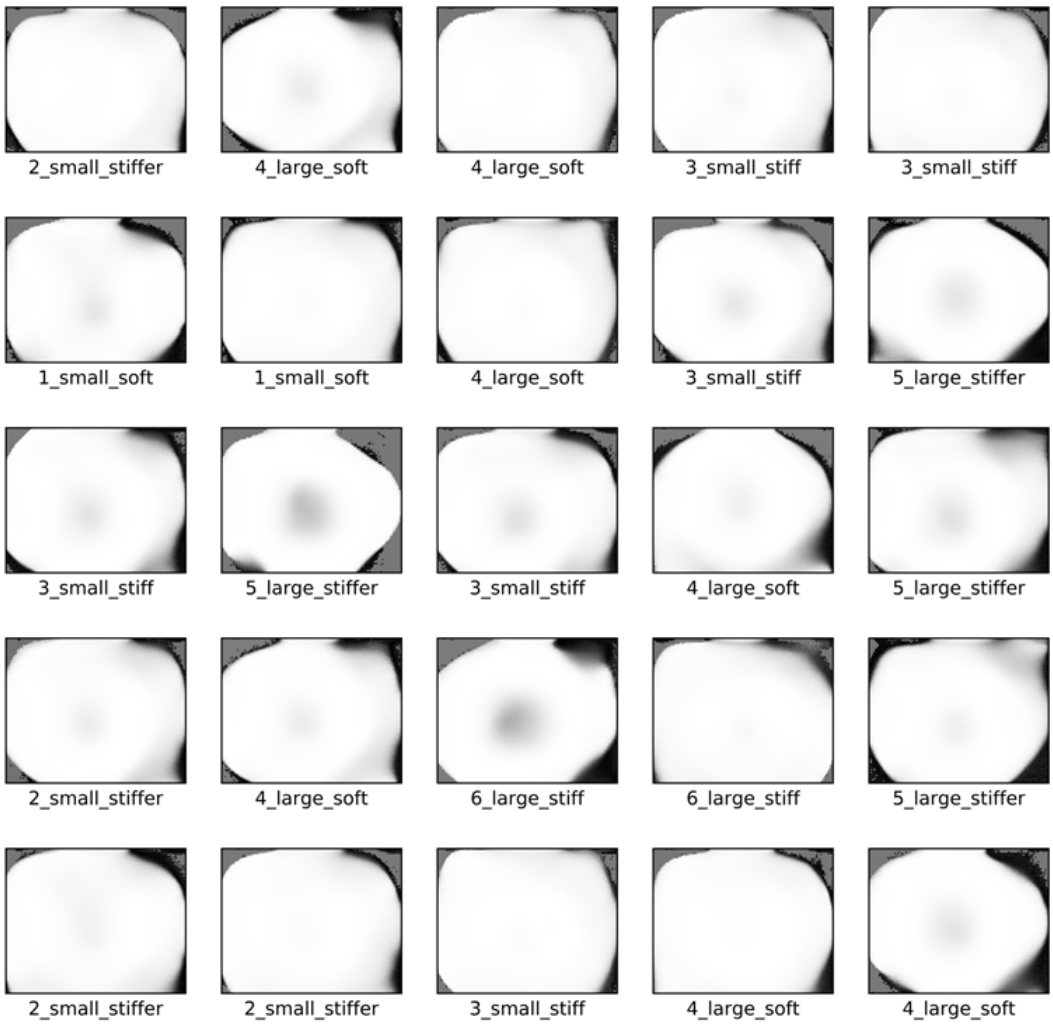

Figure 7.3: Examples of Tactile Profile Diagrams

Table 7.3: Properties of the phantom components

Description	Material	Thickness/Size, mm	Elastic Modulus, kPa
Tissue Layers			
Base	PDMS	15	629
Intermediate	PVC	12, 14, 16	7
Depth	PVC	4	7
Spherical Inclusions			
Stiff	Acrylic	11.90, 15.65, 17.20	250000
Less Stiff	PDMS	12.50, 14.43, 16.57	507
Soft	PDMS	12.30, 14.20, 16.34	197

To validate the proposed TPD method for the size and stiffness estimation, we perform the experiments with an earlier developed tissue and tumors phantom. TIP was applied in a normal direction to the tissue. The compression forces started at 0N and were gradually increased to 45N during the experiments. The phantom and its layers are shown in Fig. 7.4, and the details are presented in Table 7.3.

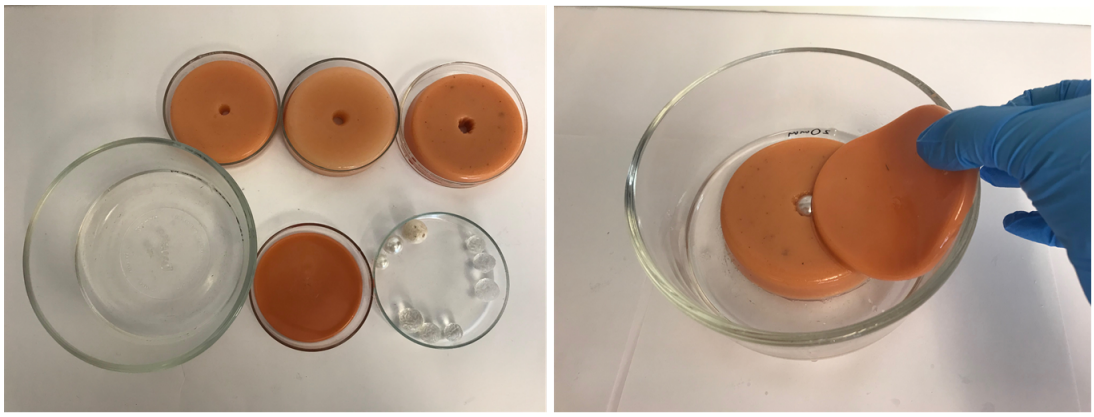

Figure 7.4: Test phantom components and their placement during the TIP experiments

We built Tactile Profile Diagrams (TPDs) from the experimental data. Selected samples of the TPDs, their corresponding volumetric reconstructions, composite gradient images, and segmented magnitude gradient images are presented in Fig. 7.5. One can see the differences in the area of high-intensity regions for smaller and larger inclusion. The sharpness and height of the 3D reconstruction peaks, and the average magnitude of the G_{magS} images, contain the information about the stiffness of inclusions. Also, the "fuzziness" of the edges

in composed gradient images seemed to correlates with inclusion's stiffness.

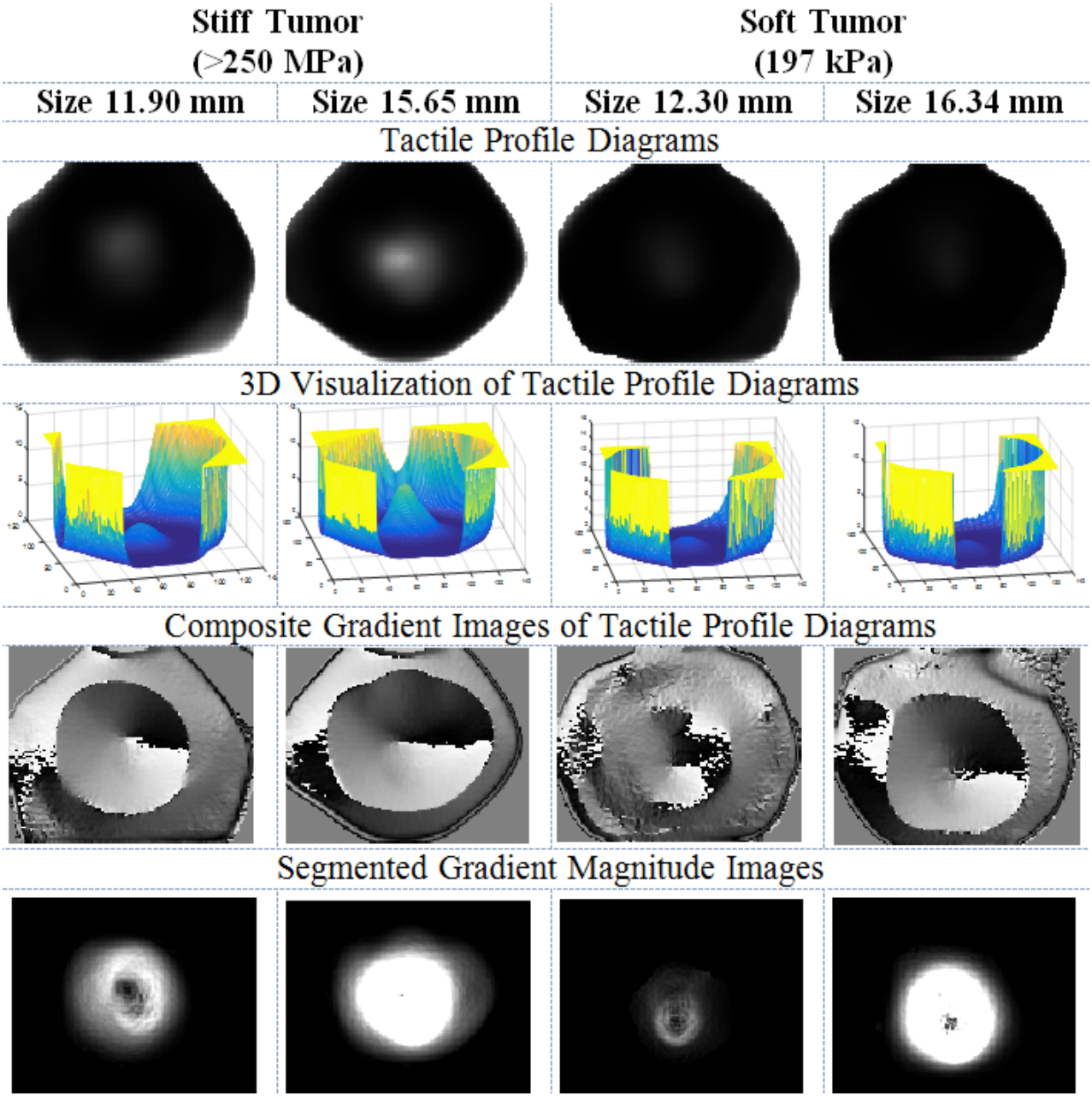

Figure 7.5: Examples of the TPD method results

Next, we calculate the size and stiffness of the tumors from their TPDs. The size estimation results from the proposed TPD method and the previously developed method are presented in Table 7.4. The calculated values are the average values of the two trials with stiff acrylic inclusions. The depths of 1 mm to 3 mm showed similar error for size

Table 7.4: Size and stiffness index calculation results

True Size, mm	**Calc. Size, mm**	**Size Error, %**	**Stiff. Index SI**
Stiff Inclusion (250 MPa)			
11.90	12.32	3.53	0.51
15.65	16.46	5.19	1.02
17.20	16.74	2.67	1.26
Average		3.80	0.93
Less Stiff Inclusion (507 kPa)			
12.50	10.66	14.71	0.55
14.43	12.49	13.42	0.81
16.57	14.55	12.20	1.39
Average		13.44	0.92
Soft Inclusion (197 kPa)			
12.30	9.75	20.75	0.23
14.20	11.94	15.92	0.41
16.34	12.83	21.50	1.00
Average		19.39	0.55

estimation as it was for the 4 mm depth. However, for the 8 mm depth, the size estimation error increased. The means and standard deviations of the relative size estimation errors are $3.80\% \pm 1.28$, $13.44\% \pm 1.26$, and $19.39\% \pm 3.03$ for stiff, softer, and soft inclusions, respectively.

Stiffness estimation results are shown in Fig. 7.6. Inclusion stiffness from the TPD method is in terms of the Stiffness Index, SI. Lower SI values are obtained for the softer inclusions, and larger SI values are obtained for the stiffer inclusions. The results for two sets of stiffer inclusions overlap due to the stiffness estimation limitations of the current TIP prototype.

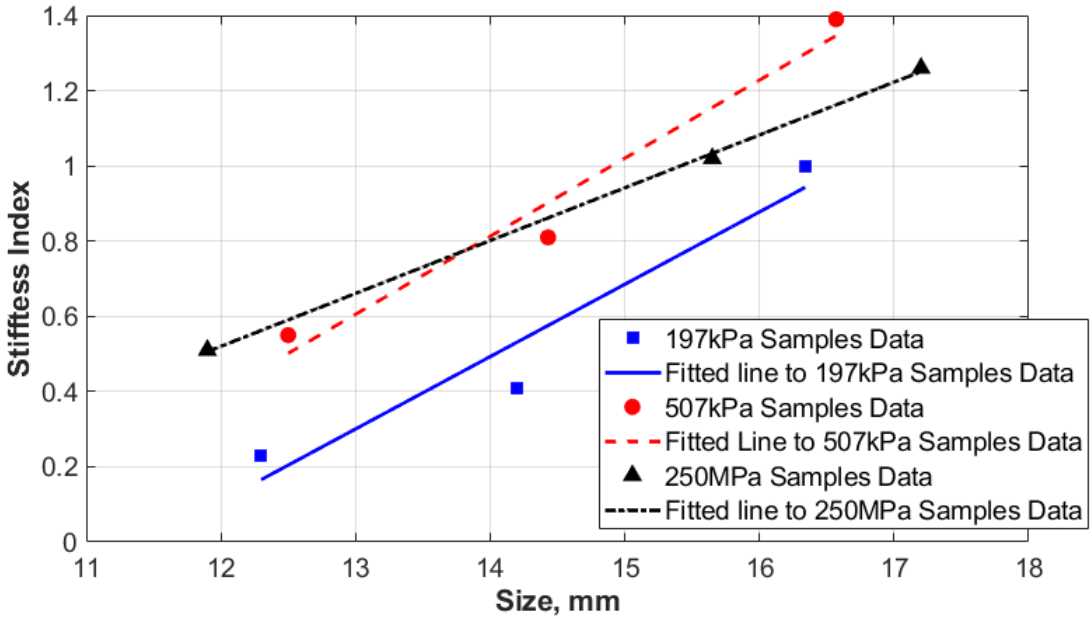

Figure 7.6: Stiffness estimation results

7.2.3 Results from Classification of Tactile Profile Diagrams

Here we describe the preliminary results for TPD classification using Convolutional Neural Network (CNN). We developed three models to classify TPDs on 12 possible classes with respect to the underlying tumor's depth, size, and stiffness.

Depth Classification (Model1)

The first CNN model is responsible for the tumor depth estimation. The description of the model is given in Chapter 5. The model was trained and tested on the data set obtained from the PDMS phantoms described earlier.

The data set included the tumor sizes 10 mm, 12 mm, 14 mm, 16 mm, 18 mm, and tumor stiffnesses 130 kPa - 250000 kPa. The tumors with depths 0 mm, 2 mm, and 4 mm considered as shallow tumors. The tumors with depths of 6 mm, 8 mm, 10 mm were considered as deep.

To separate the data on the training and the test subsets, we used the random assignment with a ratio of 0.8 correspond to the training, and 0.2 correspond to the test subset. The training subset had 6605 TPDs, and the test subset had 1651 TPD. During the model

training, we specified 50 epochs in batches of 250. No augmentation was performed at that time and may be required for the model improvement.

Figure 7.7 shows the accuracy and loss plot for the training and test subsets. The final validation accuracy of the classification is 0.9788.

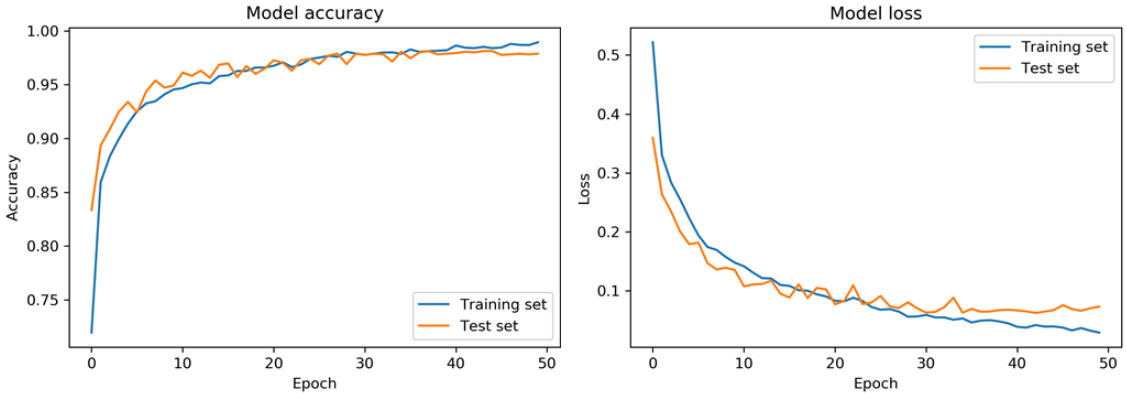

Figure 7.7: Accuracy and loss plots for Model1 over 50 epochs

Figure 7.8 shows 15 random TPD from the test subset classified. The figure shows the classification predictions for each of the samples as a bar diagram. Blue color corresponds to the correctly classified TPDs. Red bar color would signify an incorrectly classified TPD.

Size and Stiffness Classification for Shallow Tumors (Model2a)

The second CNN model is responsible for classifying shallow tumors (0 mm, 2 mm, 4 mm depth) based on their size and stiffness. The description of the model is given in Chapter 5. The model was trained and tested on the data set obtained from the PDMS phantoms, as described earlier.

The data set included the tumor sizes 10 mm, 12 mm (considered as small for the classification), and 14 mm, 16 mm (considered as large for the classification). The tumor stiffnesses ranged from 130 kPa - 250000 kPa. Soft tumors ranged from 130 kPa to 271 kPa, less stiff tumors ranged from 316 kPa to 444 kPa, and stiff tumors range was from 506 kPa to 250000 kPa (for Acrylic tumors).

To separate the data on the training and the test subsets, we used the random assignment

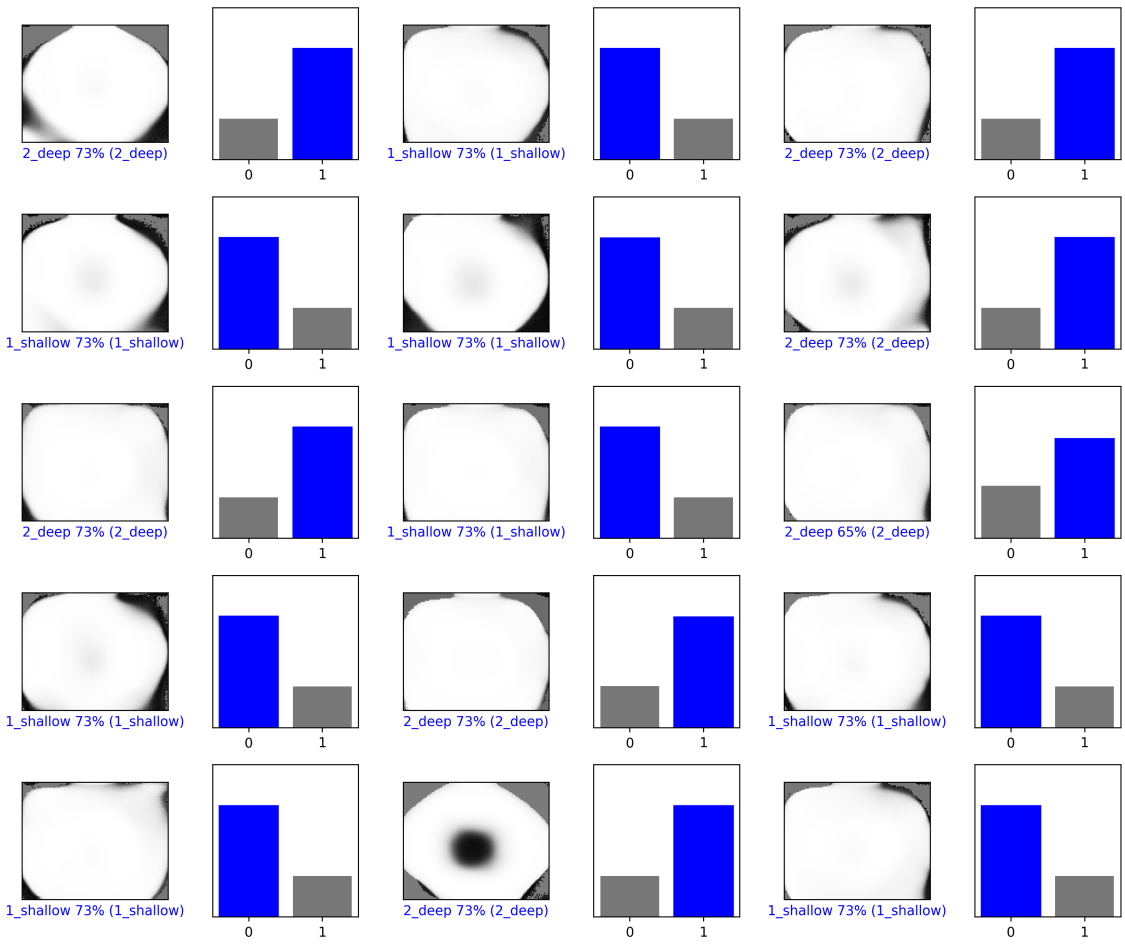

Figure 7.8: Examples of classification results for Model1

with a ratio of 0.8 correspond to the training, and 0.2 correspond to the test subset. The training subset had 2713 TPDs, and the test subset had 683 TPDs. During the model training, we specified 50 epochs in batches of 250. No augmentation was performed at that time and may be required for the model improvement.

Figure 7.9 shows the accuracy and loss plot along 50 epochs for training and test subsets. The final validation accuracy was 0.8594.

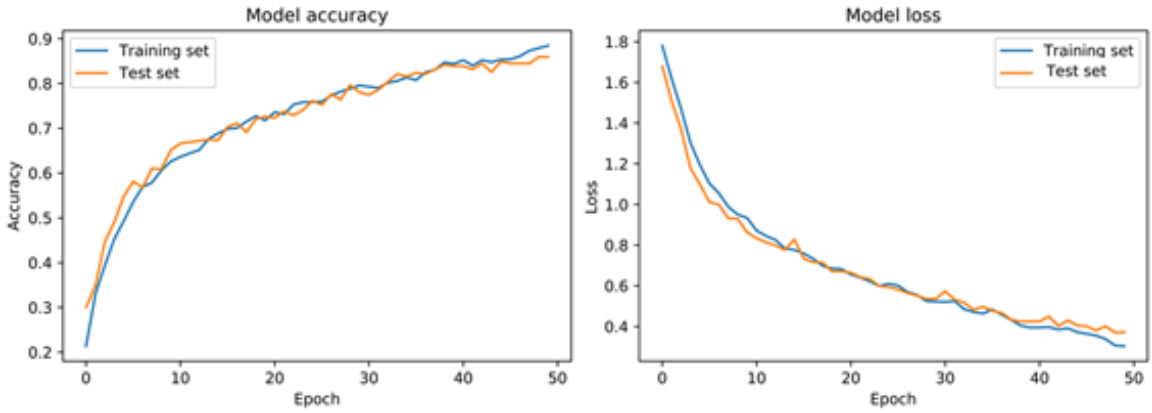

Figure 7.9: Accuracy and loss plots for Model2a over 50 epochs

Figure 7.10 shows 15 random TPD from the test subset classified. The figure shows the classification predictions for each of the samples as a bar diagram. Blue color corresponds to the correctly classified TPDs. Red bar color would signify an incorrectly classified TPD. All of the examples were correctly classified.

Size and Stiffness Classification for Deep Tumors (Model2b)

The third CNN model is responsible for classifying deep tumors (6 mm, 8 mm, 10 mm depth) based on their size and stiffness. The description of the model is given in Chapter 5. The model was trained and tested on the data set obtained from the phantoms described earlier.

The data set included the tumor sizes 10 mm, 12 mm (considered as small for the classification), and 14 mm, 16 mm (considered as large for the classification). The tumor stiffnesses ranged from 130 kPa - 250000 kPa. Soft tumors ranged from 130 kPa to 271

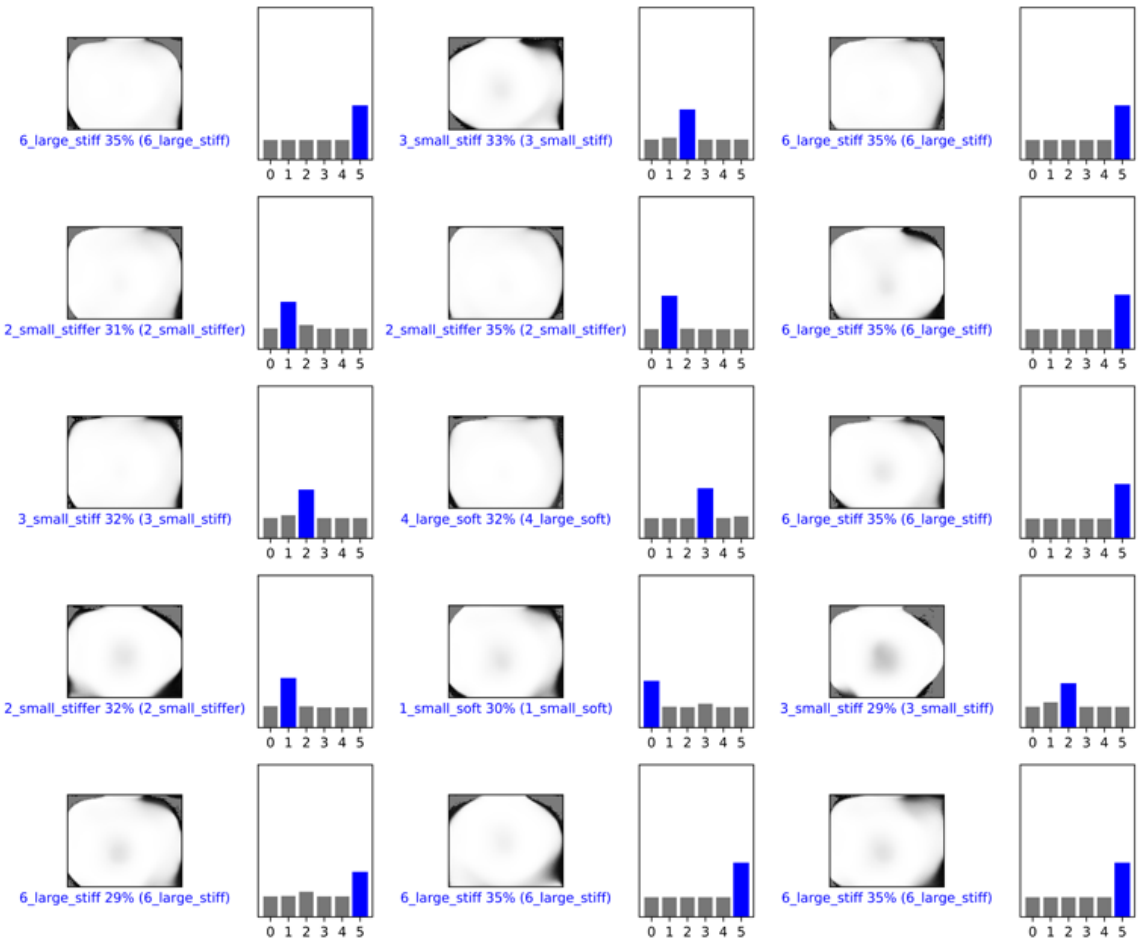

Figure 7.10: Examples of classification results for Model2a

kPa, less stiff tumors ranged from 316 kPa to 444 kPa, and stiff tumors range was from 506 kPa to 250000 kPa (for Acrylic tumors).

To separate the data on the training and the test subsets, we used the random assignment with a ratio of 0.8 correspond to the training, and 0.2 correspond to the test subset. Training subset had 2727 TPDs, and the test subset had 669 TPDs. During the model training we specified 50 epochs in batches of 250. No augmentation was performed at that time and may be required for the model improvement.

Figure 7.11 shows the accuracy and loss plot along 50 epochs for training and test subsets. The final validation accuracy was 0.8386.

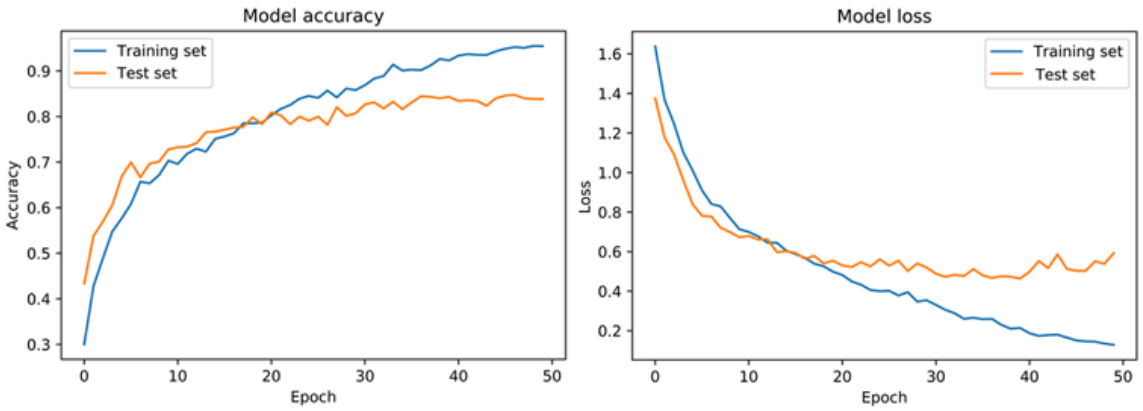

Figure 7.11: Accuracy and loss plots for Model2b over 50 epochs

Figure 7.12 shows 15 random TPD from the test subset classified. The figure shows the classification predictions for each of the samples as a bar diagram. Blue color corresponds to the correctly classified TPDs. The red bar color signifies an incorrectly classified TPD. There are two incorrectly classified examples.

7.3 *In-vivo* Human Experiment Results

The TIP was tested in a pilot study of twenty-one human patients (IRB# 22050 Temple University), to determine the accuracy of the device in a real healthcare environment (Oleksyuk et al., 2018). The patients were scheduled for a biopsy, where the histopathology reports from the biopsy were used as the truth values in the classification output of TIP. Patients

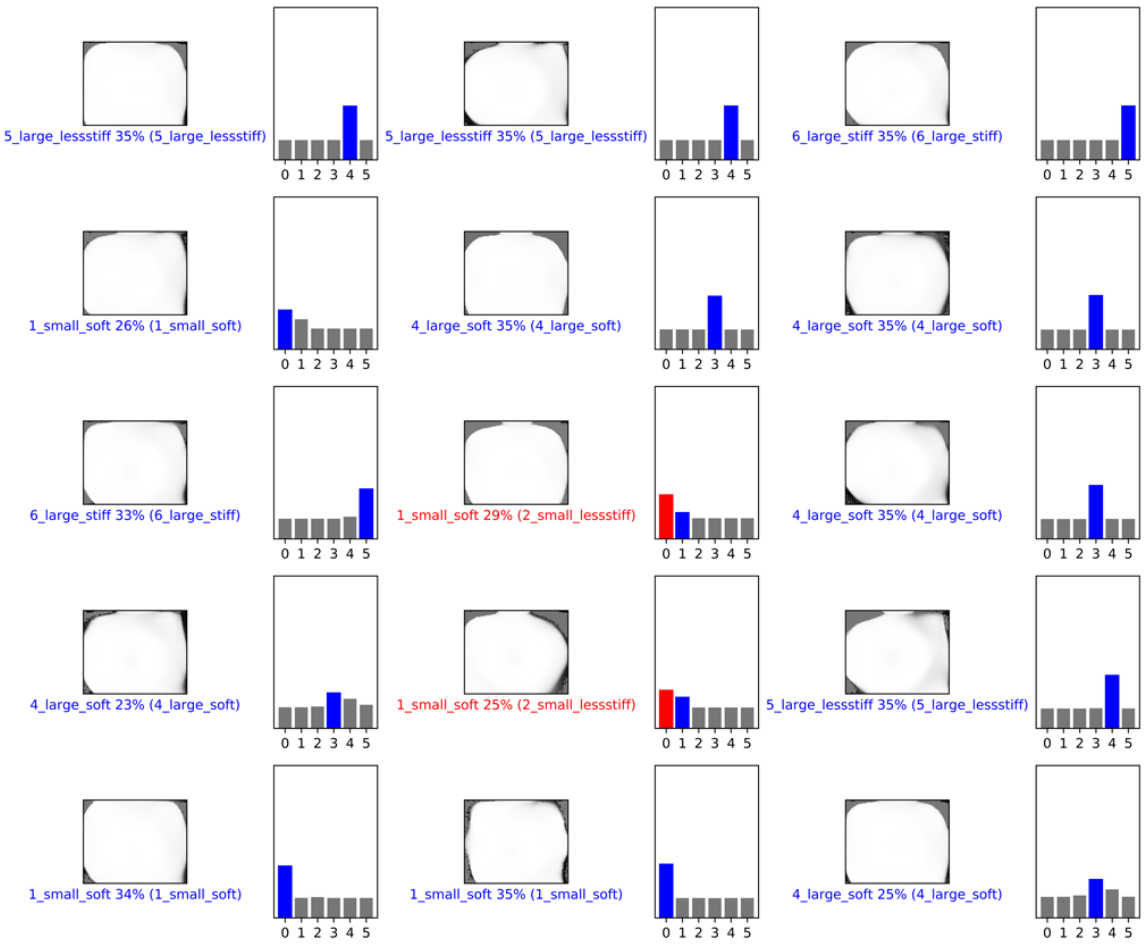

Figure 7.12: Examples of classification results for Model2b

were randomly selected by the radiologists.

7.3.1 Size and Deformation Index (DI) Estimation

For the human patient experiments, the physicians initially approximate the location, size, and depth of the masses. The doctors were instructed to use 12 mm threshold for size and 10 mm threshold for depth. However, if the mass was approximated as more than 30 mm in diameter, the 3D interpolation for large and deep inclusions was used for size calculation. The results from the human patients' experiments in-vivo are shown in Table 7.5. The patients used for the studies had tumors in varying sizes from 11 mm to 60.8 mm, which was determined from the ultrasound images (true tumor size in Table 7.5).

From the results, the serial numbers from 1 to 15 have a size estimation error of less than 20%. In these cases, the estimated size values are close to the real values. For example, in serial number 10, a patient with a small tumor of size 11 mm in a depth of 7 mm is showing a very good estimated size and is found to be malignant through the histopathology report. This shows the ability of the TIP to detect small tumors at deeper depth if it is stiffer or malignant. In serial numbers 16 to 21, the error percentage increased from 20% to 70%. This is mainly due to the non-palpable nature of the tumor and the human error in estimating the depth and size.

The deformation index is also given in Table 7.5. We observe that the malignant tumors (denoted with "+" symbol) show a higher deformation index than the benign cases. The malignant and benign cases are conïňĄrmed using histopathology reports. The malignant tumors have a deformation index values above 50,000, whereas benign tumors have smaller deformation index values. This pattern is due to the fact that malignant tumors are stiffer than benign tumors.

7.3.2 Breast Tumor Classification

After the size and deformation index of tumors are estimated using TIP, we calculate the Risk Score to classify tumors as benign or malignant.

Risk Score is a unitless numerical value, which can be used as a scale to classify the tumor as malignant and benign. Based on the calculated size of the tumor and measured de-

Table 7.5: The in-vivo test results for estimating size and deformation index using TIP in 21 patients

Serial number	True tumor size (mm)	Calculated tumor size (mm)	Error in size calculation (%)	DI (10^4)
1+	54.20	57.19	5.52	6.79
2+	56.40	52.95	6.12	4.19
3+	43.30	46.33	7.00	4.91
4	12.20	13.15	7.79	2.56
5	60.40	54.37	9.98	1.60
6	17.70	15.77	10.90	1.39
7	13.90	15.5	11.51	3.88
8+	53.80	60.82	13.05	4.31
9+	60.80	52.49	13.67	3.58
10+	11.00	9.39	14.64	9.34
11	35.00	40.31	15.17	1.90
12+	53.80	45.04	16.28	3.30
13	17.50	14.58	16.69	2.74
14	14.00	16.56	18.29	3.62
15+	24.29	19.65	19.10	5.04
16+	12.00	14.7	22.50	5.47
17	20.10	14.04	30.15	9.40
18+	35.90	50.23	39.92	5.58
19	20.06	11.86	40.88	2.90
20	11.02	15.96	44.83	10.75
21	30.61	52.23	70.63	4.58

+ Represents the malignant cases: information obtained by clinical pathology reports

formation index, the breast tumors are classified as benign and malignant using the scoring method. The Risk Score ranges from 0 to 5, where 0 represents the benign, and 5 represents the malignant tumor. A marginal threshold value was set, where any risk score below threshold is considered benign. The calculated Risk Score is based on the below equation,

$$RiskScore = \left[\frac{W_1 \times S}{S_{max}} + \frac{W_2 \times DI}{DI_{max}}\right] R, \tag{7.1}$$

where W_1 and W_2 are the two weights used for size and deformation index respectively, S represents the estimated size value, S_{max} is the maximum estimated size value, DI is the calculated deformation index, DI_{max} is the maximum calculated deformation index. R is the highest value of Risk Score used.

To classify tumors, we choose the pair of weights (W_1 and W_2), which gives the best classification sensitivity and specificity for a training subset (20 patients). We computed the Receiver Operating Characteristic (ROC) curve with different weights for each training subset, where W_1 and W_2 varied from 0 to 1 in steps of 0.1. The sum of the weights has to be one by using any of the eleven combinations (e.g., 0.1 and 0.9, 0.2 and 0.8, etc.). The optimal weights and corresponding threshold values were determined. For each pair of weights we computed the ROC curve varying the threshold values from the smallest calculated score to the largest calculated score in a subset. Then we looked for minimum distance from the (0, 1) point in the ROC graph to the curve, where (0, 1) point is a perfect classifier. In Fig. 7.13, a sample ROC curve is shown with the optimal point at (0.1818, 1), which corresponds to 100% sensitivity and 82% specificity. The corresponding threshold value for the risk score came out to be 1.99, and the optimal weight came out to be W_1 = 0.3 and W_2 = 0.7. Then the test subset (1 patient) was classified on malignant or benign with the found weights and threshold. The classification results are compared with original clinical pathological reports as shown in Table 7.6. From the table, we note that except for two false positive cases, the rest of the cases are accurately classified.

We employed the Leave-One-Out-Cross-Validation (LOOCV) technique to validate the human test results to determine the performance of the TIP device during the pilot study. The sensitivity, specificity, and accuracy of the system were measured to assess the reliability of the TIP. These performance metrics were calculated based on the Risk Score using

Table 7.6: Risk Score based classification of tumors using TIP output

Serial Number	Pathology Results	Calculated Risk Score	TIP Classification
1	Malignant	3.62	Malignant
2	Malignant	2.67	Malignant
3	Malignant	2.74	Malignant
4	Benign	1.16	Benign
5	Benign	1.86	Benign
6	Benign	0.84	Benign
7	Benign	1.65	Benign
8	Malignant	3.00	Malignant
9	Malignant	2.46	Malignant
10	Malignant	3.27	Malignant
11	Benign	1.61	Benign
12	Malignant	2.40	Malignant
13	Benign	1.25	Benign
14	Benign	1.59	Benign
15	Malignant	2.13	Malignant
16	Malignant	2.15	Malignant
17	Benign	0.65	Benign
18	Malignant	3.05	Malignant
19	Benign	1.24	Benign
20	Benign	4.42	Malignant++
21	Benign	2.78	Malignant++

++ Denotes false positive cases

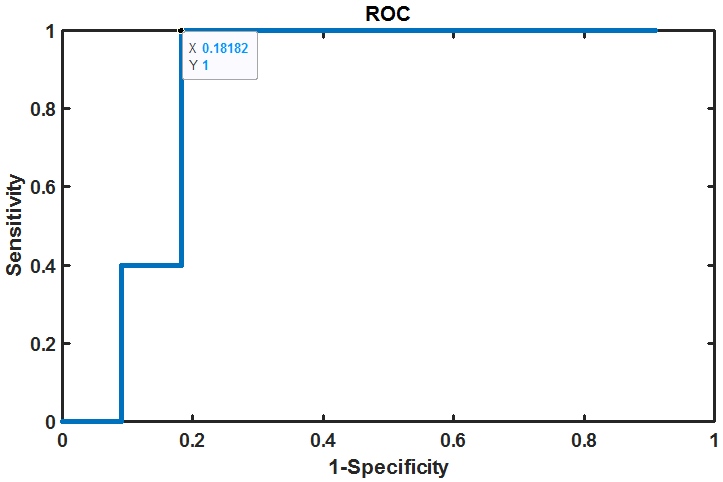

Figure 7.13: ROC curve to determine the threshold

the below equations,

$$Sensitivity_{TIP} = \frac{TP}{TP+FN}(\%), \tag{7.2}$$

$$Specificity_{TIP} = \frac{TN}{TN+FP}(\%), \tag{7.3}$$

$$Accuracy_{TIP} = \frac{TN+TP}{TN+FP+TP+FN}(\%), \tag{7.4}$$

were TP, TN, FP, and FN represent true positive, true negative, false positive, and false negative cases, respectively. False positive is considered to be a case where benign masses are classified as malignant, whereas false negative are cases where malignant masses are classified as benign. True positives are correctly classified malignant cases. True negatives are correctly classified as benign cases.

For our data set, $Sensititvity_{TIP}$, $Specificity_{TIP}$ and $Accuracy_{TIP}$ are calculated to be 100%, 82%, and 90.5%, respectively. We note that the optimal weights for all of the subsets came out to be W_1 = 0.3, W_2 = 0.7. The optimal threshold came out to be 1.99. Those optimal weights may not be the global optimal values. However, weighing stiffness more than the size seems to agree with literature and the experiences of doctors.

7.4 Discussion

In verify the performance of the system and the algorithms, first, we developed a breast tissue mimicking phantom with the mechanical properties of breast tissues and tumors. Then, we completed phantom experiments with TIP to create the application specific data set. Next, we propose the Tactile Profile Diagrams method combined with CNN classification for evaluation of depth, size, and stiffness of the tumors. Finally, we tested our device during a pilot study using 21 human patients. The preliminary results suggest that TIP can accurately characterize mechanical properties and superficial optical properties of breast cancer in-vivo.

CHAPTER 8

MULTISPECTRAL IMAGING PROBE EXPERIMENTS

In this chapter, we will describe the plan for multispectral imaging experiments and present our preliminary results. We will also introduce a custom tissue phantom, which mimics superficial optical properties of breast tissues and can be combined with the mechanical properties phantom described in the previous chapter, for bimodal imaging experiments.

8.1 Optical Property Phantom

Here, we complete a short survey on the available tissue phantoms, which mirror optical properties of human tissues. We describe the proposed design of the phantom and share how the phantom will be fabricated for our application.

8.1.1 Review of Optical Property Phantoms

Fluid-based phantoms are very convenient and commonly used to mimic optical property of living tissues in the lab settings. They are relatively easy to fabricate and to make changes to their property. The majority of the liquid phantoms are water-based, with the addition of scattering and absorption agents (Fiaschetti et al., 2018). However, liquid phantoms need to be in a secure container, and they are difficult to transport. In addition, the liquid phantom mixture can be unstable, with the larger particles concentrated at the bottom of the container (Hebden et al., 2006).

To overcome these difficulties, researchers are developing solid phantoms from a variety of materials, such as Delrin plastic, PDMS, wax, polyester resin, epoxy resin, agar gel, gelatin, and fibrin. The absorption and scattering agents that are used to fabricate the solid phantoms are intralipid, hemoglobin, dyes, titanium dioxide, carbon black, ferric chloride, and silica spheres (Sallaway et al., 2014; Hebden et al., 2006; Miranda et al., 2013; Giller et al., 2003; Boehm et al., 2001; Grand et al., 2008; Lamouche et al., 2012).

Unfortunately, hydrogels (agar and gelatin) are not durable, they cannot withstand me-

chanical compressions, and they melt at room temperature. The difficulty with silicone phantoms is the difficulty of adding organic additives. Fibrin can be used for optical property phantoms because it is a naturally occurring protein in humans, and it can be easily mixed with different types of scattering and absorption agents (Price et al., 2010). Also, Polyvinyl alcohol (PVA) is commonly used for many types of optical imaging phantoms (Price et al., 2010).

Some of the phantoms are able to mimic several types of tissue property - multimodal imaging phantoms. Lamouche et al. (Lamouche et al., 2012) provide a review of the possible materials for optical coherence tomography phantom, which has to possess the optical and mechanical properties of tissues. The study found that no one material is perfect for the application, yet several of them can be implemented. They mentioned the advantages and disadvantages of the phantom materials. They suggest using silicone if a volumetric phantom will be made, yet to prefer fibrin if adding organic agents. They also mentioned that PVA phantoms could provide the ability to tune mechanical property of the phantom, yet the adding of optical characteristics to such phantom is difficult. However, in another study, researches incorporate optical property in the PVA phantom to calibrate an optical tomograph (Hebden et al., 2006).

Researchers from (Spirou et al., 2005) study proposed to mimic the optical and acoustic property of tissues with Polyvinyl chloride (PVC) material, titanium dioxide, and a black plastic coloring agent.

Price et al. (Price et al., 2010) were able to combine mechanical and x-ray attenuation property in phantom. They developed a new phantom material, which was a solution of Polyvinyl alcohol in ethanol and water. The material underwent freeze-thaw cycles to obtain the desirable elastic property. Depending on the firmness of the material, it had varying x-ray attenuation properties.

One of the latest multimodal phantoms with tunable mechanical, optical, and acoustic property was developed from multiple compounds (gelatin, agar, PDMS silicone) and additives (blood mimicking fluid, bovine blood serum, intralipids, microbeads, India Ink and dyes) (Chen et al., 2016). The authors propose a multilayered design with the ability to change the property as desired by adding or removing different layers in the phantom.

8.1.2 Proposed Phantom Design

Multispectral Imaging Probe and its algorithms are developed to characterize superficial optical property of tissues, which can distinguish malignant and benign tumors. The targeted features, such as the differential color, the differential texture, the differential size of the reddened area, and the differential asymmetry, will be implemented in the phantom to test the method.

We propose to use multiple thin layers of silicone (Polydymethyl siloxane) with added artificial coloring agents (Smooth-On Inc., Macungie, PA), intralipid, and human blood (Lampire Biological Laboratories, Pipersville, PA) to mimic the aforementioned breast tissue features. There will be more or less coloring agents added to the PDMS silicone layer to fabricate the test samples. The reflectance variations due to PDMS concentration will be experimentally eliminated.

We completed a preliminary study by mixing an organic absorber with PDMS material before curing. The mixture cured well. Fig. 8.1 presents the design of the proposed MIP phantom.

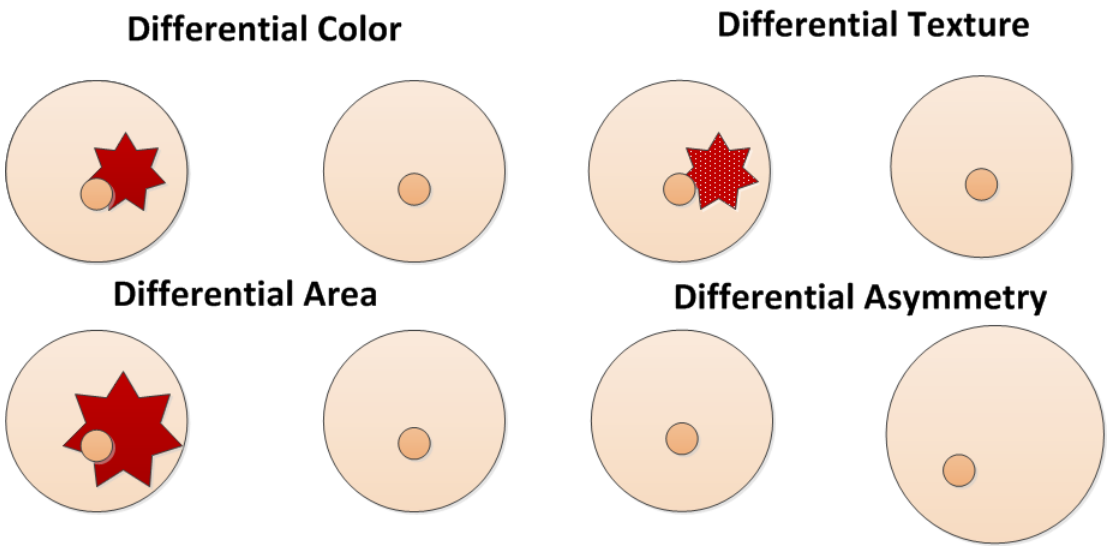

Figure 8.1: MIP phantom sets

The differential color feature will be implemented by adding some amount of blood to the skin-colored PDMS sample, in contrast to the PDMS sample of skin-color only. The

differential size of the reddened area will be implemented as a different amount of blood added to the colored silicone sample. The differential texture parameter will be implemented with the use of textured fabric on the top of the curing PDMS sample. The result will mimic the orange type of skin (pitted skin). Finally, the differential asymmetry parameter will introduce asymmetric changes in the breast phantom with additional enlargements and distortions described in the literature. There will be one feature on one sample or several features implemented on one multispectral imaging phantom sample.

The silicone layers with the desired optical property can be placed on the top of the mechanical property phantom described in the previous chapter. We will be able to use both phantom modalities at once for each imaging acquisition if needed (Fig. 8.2).

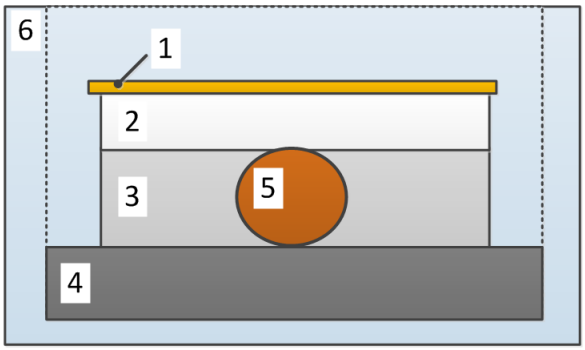

1. Multispectral layer	PDMS 1:2 Ratio + absorption and scattering agents	94 kPa
2. Depth layer	PDMS 1:2 Ratio	94 kPa
3. Intermediate layer	PDMS 1:2 Ratio	94 kPa
4. Base layer	PDMS 1:20 Ratio	629 kPa
5. Tumor Phantom	PDMS Ratios	130 kPa ... 629 kPa
6. Pyrex glass container		

Figure 8.2: Bimodal imaging phantom with optical and mechanical property

8.2 Experimental Setup

The first step of MIP experiments is to verify the target wavelengths for multispectral image acquisitions. We will use human blood samples (Lampire Biological Laboratories, Pipersville, PA) and will employ the Retiga EXi hyperspectral camera to complete this task. In our preliminary experiments, we demonstrate how we found the wavelengths cor-

responding to the porcine blood chromophores of deoxyhemoglobin, oxyhemoglobin, lipid, and water.

To select the four wavebands in NIR spectrum for human blood, we will use TIP with the multispectral attachment and a Retiga EXi hyperspectral camera. We will image the following samples: three water samples, three human blood samples, three soft phantom layers, three stiff phantom layers. We plan to complete three trials of imaging in the range 650 nm to 1100 nm using Retiga/TIP Imaging System. After that, we select regions of interest on the images with ENVI software. Later, we will plot the reflection intensity vs. wavelength results for the selections and identify the four wavebands of interest, based on the acquired data.

After the four target wavelengths are selected, we will proceed to phantom fabrication. We will make 100 tissue samples for each Multispectral Imaging Probe's differential feature, as well as, 100 silicone tissue samples without the features to mimic normal breast tissue. This amount of the test samples will allow us to complete MIP feasibility experiments and collect a meaningful for the application dataset.

Finally, we will complete the MIP experiments. To distinguish each of the differential parameters, we will image the phantom in pairs using MIP. One PDMS sample will represent the affected breast and will include one or more differential features. The other sample in the pair will represent the corresponding normal breast and will not carry differential features. We will complete five imaging sessions of the same sample pair during the Multispectral Imaging Probe experiments.

8.3 Preliminary Results

We completed two preliminary experiments to evaluate the multispectral imaging idea and its algorithms for our application. In the first, we completed the search of the target wavelengths for porcine blood, which was available to us at that time. Next, we composed Multispectral Profile Diagrams for nine samples of porcine tissues with blood injections and evaluated tissue representation capabilities of MPDs.

We completed an imaging experiment with porcine blood injected into ex-vivo tissues

to locate the reflectance wavelengths for deoxy- and oxyhemoglobin, lipid, and water chromophores. Fig. 8.3 illustrates the setup of the experiment.

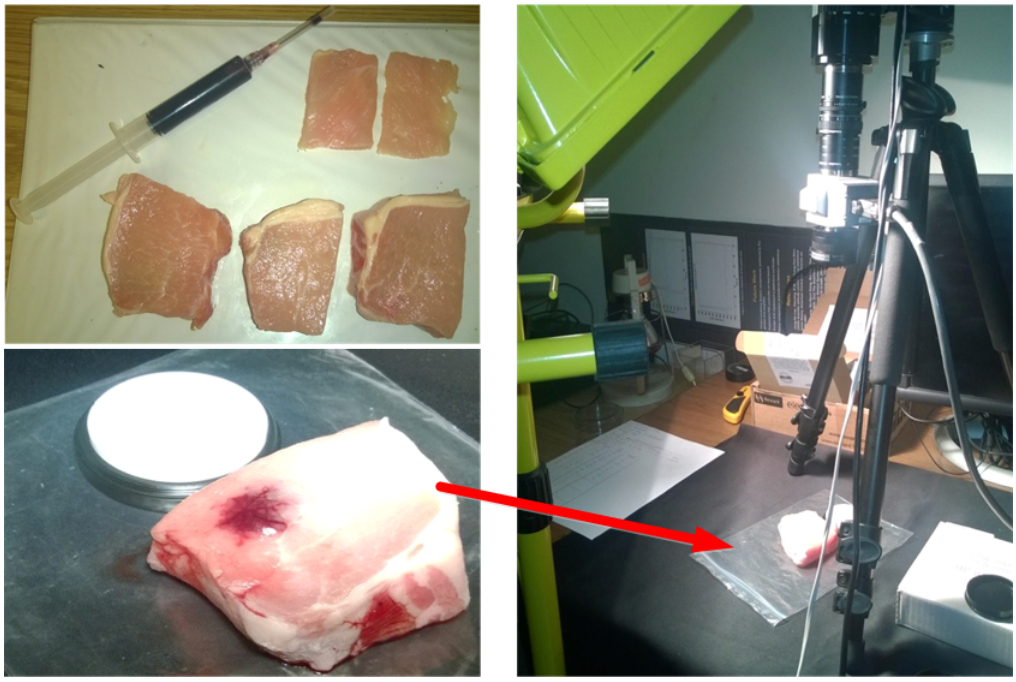

Figure 8.3: MIP phantom test setup

We employed the Retiga EXi hyperspectral camera and a white reflectance standard to complete imaging for the wavelength range of 650 nm to 1100 nm. We had three porcine tissue specimens, which we used to develop nine imaging samples. At first, we imaged the samples 1, 2, and 3, which had no blood injected. Then we injected 1 cm^3 of blood into each of the 3 specimens, which becomes samples 4, 5, and 6. After we imaged them, we added another 1 cm^3 of blood into each of the 3 specimens to obtain samples 7, 8, and 9 for the imaging. All nine samples imaged at 650 nm band are shown in Fig. 8.4. In addition, Fig. 8.5 presents examples of reflectance images for Sample #8.

The hyperspectral images were processed with ENVI software (Broomfield, CO). We applied a median filter to eliminate salt-and-pepper noise. After the pre-processing steps and calculations, we plot the normalized reflectace intensities vs. the acquisition wavelength for normal tissue regions (N) and for blood injection sites (T) in Fig. 8.6. The reflectance spectra of the injection cites are lower in general than the spectra corresponding to the normal tissue cites. The primary mechanisms that define reflectance are absorption

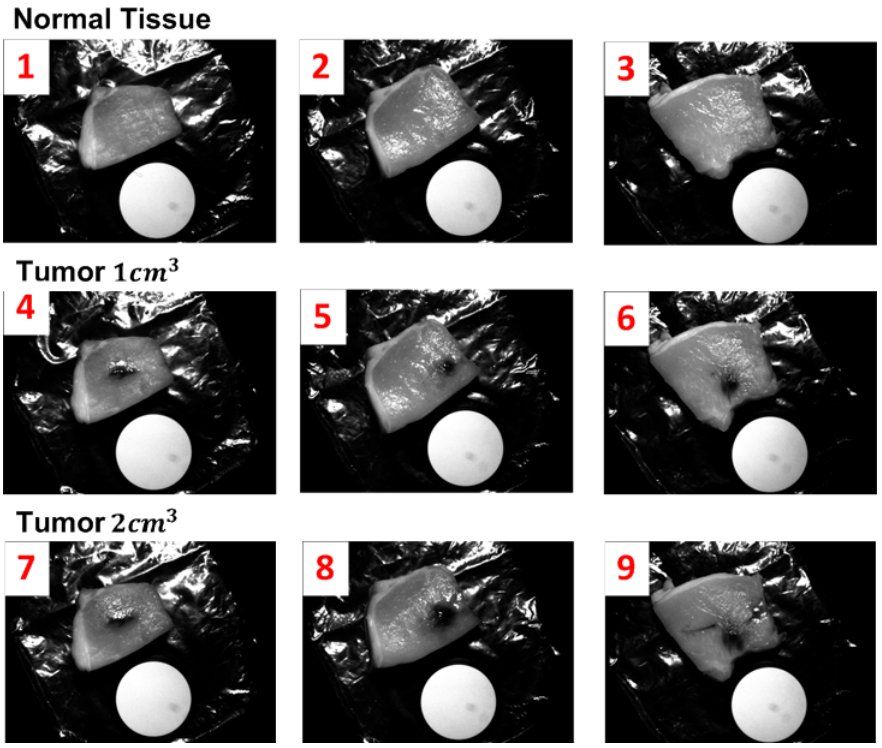

Figure 8.4: Preliminary experimental samples at 650 nm

and scattering, both of which vary with wavelength to produce the reflectance spectrum. Because tissue with blood absorbs more than tissue without blood content, it reflects less light to be captured with the camera. The target wavelengths we found to be at 740 nm, 810 nm, 860 nm, and 990 nm for deoxy-, oxyhemoglobin, lipid, and water, respectively.

Next, we used the selected wavelengths to compose Multispectral Profile Diagrams for the nine porcine samples. Fig. 8.7 shows the developed MPD for Sample #8 and the segmented injected blood region on the MPD.

Fig. 8.8 presents MPDs and their segmentation for all nine porcine samples. We can see from the figure, that we are able to automatically segment the MPD on the normal tissue region and the injection region.

8.4 Discussion

We proposed the design of the test phantom and experimental setup for Multispectral Imaging Probe experiments. We presented the literature overview on the silicone optical prop-

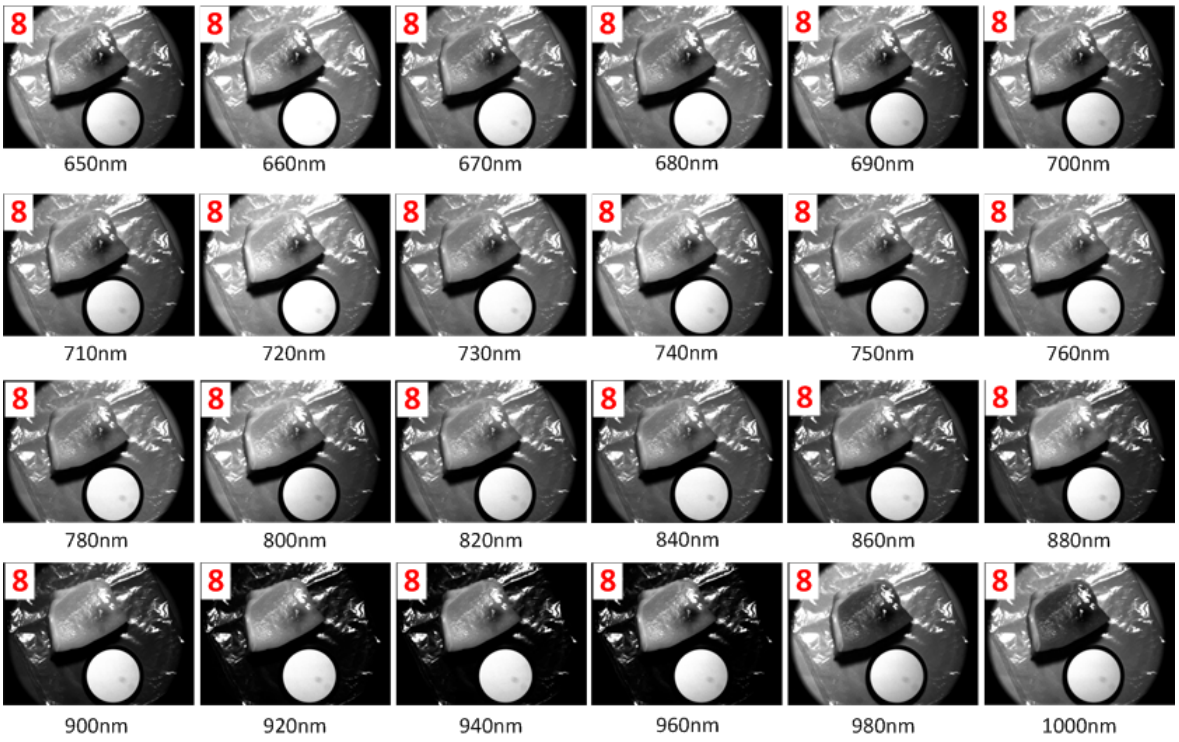

Figure 8.5: Selected reflectance images of Sample #8 over the range of the acquisition wavelengths

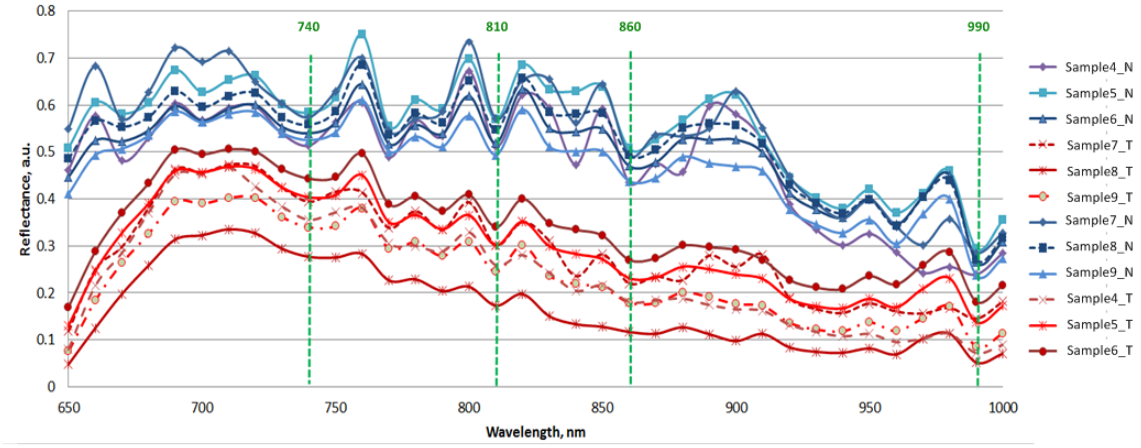

Figure 8.6: Reflectance spectra results for the preliminary experiment with porcine samples

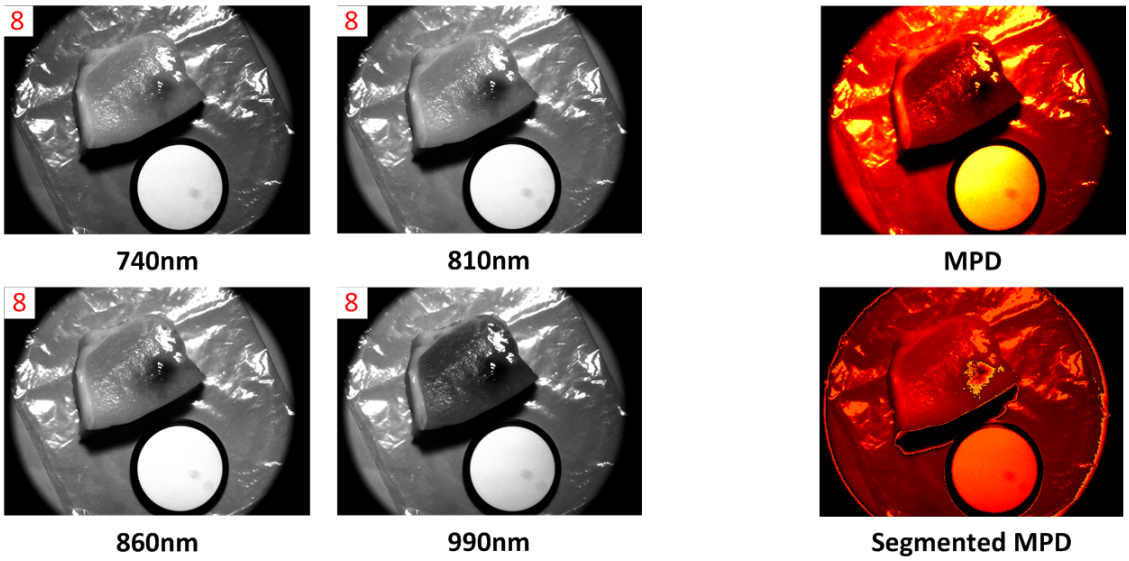

Figure 8.7: Sample #8 Multispectral Profile Diagram and its segmentation

erty phantom. We also demonstrated the results from our preliminary experiments, where we were able to construct Multispectral Profile Diagrams, find the target wavelengths of MIP for porcine tissue phantoms, and were able to do segmentation of the affected area within the composed Multispectral Profile Diagrams for these samples.

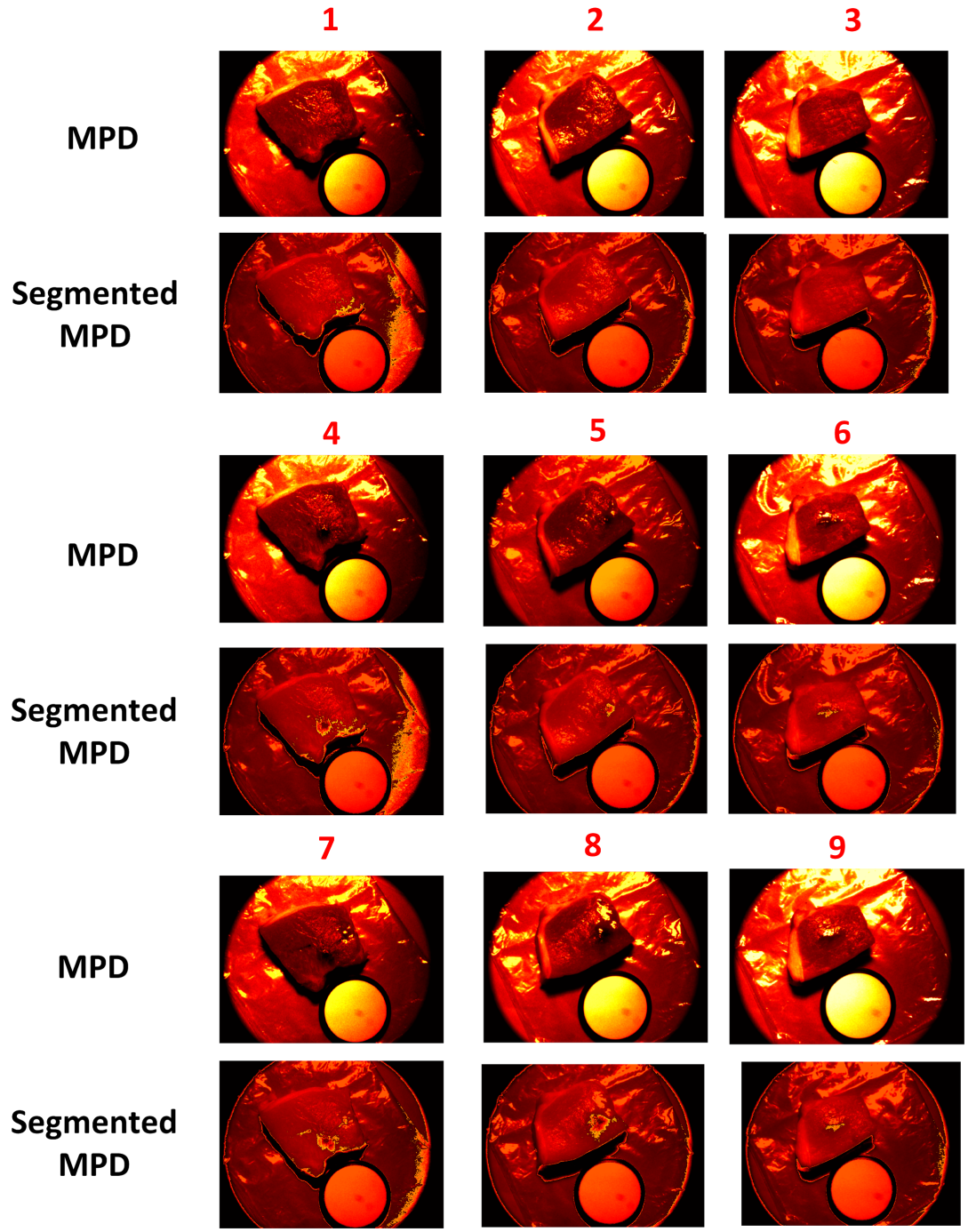

Figure 8.8: Multispectral Profile Diagrams and their segmentation for all of the experimental samples

CHAPTER 9

CONCLUSIONS AND FUTURE WORK

Here we will provide our conclusions for the dissertation proposal and will outline the plan for the future work.

9.1 Conclusions

In this dissertation proposal, we developed the bimodal imaging probe and its algorithms to characterize breast tissues with tumors and to estimate the individualized breast cancer risk.

We developed the bimodal imaging system and its calculation algorithms to capture the tactile and multispectral properties of breast tumors and tissues. We also proposed the Profile Diagrams method to efficiently capture, encode, and analyze tactile and multispectral imaging signals. In our preliminary experiments, we showed good classification accuracy in classifying tissues and tumors based on their depth, size, and stiffness using Tactile Profile Diagrams and Convolutional Neural Network. Lastly, we propose the method to calculate the individualized Malignancy Risk Score for patients based on the imaging data from TIP and MIP modalities, and the individual breast cancer risk.

9.2 Future Work

In this section, we outline the research plan for the dissertation work. The plan will be divided into four main sections, with the actions to meet them discussed. In this dissertation proposal, we presented the primary results for some of the objectives, and the rest will have to be completed. The following list describes the tasks needed to be completed for the dissertation.

1. **Develop the Tactile Imaging Probe (TIP) and its algorithms**

    (a) Complete simulations for the Tactile Imaging Probe's sensing element.

(b) Build the Tactile Imaging Probe prototype.

(c) Develop algorithms for tumor size and stiffness estimation.

(d) Suggest a method to represent tactile information from TIP data as Tactile Profile Diagrams.

(e) Propose a method to estimate tumor depth from Tactile Profile Diagrams using Convolutional Neural Network.

(f) Propose a method to estimate tumor size and stiffness from Tactile Profile Diagrams using Convolutional Neural Network.

(g) Develop a breast tissue and tumors mimicking phantom.

(h) Complete phantom validation experiments.

(i) Employ the algorithms on the phantom data, analyze the results.

(j) Complete a pilot in-vivo study and analyze the results.

2. **Develop Multispectral Imaging Probe (MIP) and its algorithms**

(a) Complete a literature review on the superficial breast tissue features attribute to cancer diagnosis, and how they can be imaged.

(b) Develop the sensing principle and build the Multispectral Imaging Probe.

(c) Suggest a method to represent superficial breast tissue information as Multispectral Profile Diagrams.

(d) Develop technique to characterize breast tissue color, texture, size of the affected region, and the extend of bilateral asymmetry.

(e) Develop optical properties tissue phantom as a part of the bimodal imaging phantom.

(f) Complete phantom validation experiments.

(g) Employ the algorithms on the phantom data, analyze the results.

3. **Develop Combined Malignancy Risk Score Method**

(a) Complete a literature review on the risk score calculation for cancer patients.

(b) Propose the method to calculate a malignancy index from TIP modality.

(c) Propose the method to calculate a malignancy index from MIP modality.

(d) Propose the method to include the individual malignancy risk assessment into the calculation.

(e) Develop the method of Combined Malignancy Risk Score calculation with the appropriate weights for the indexes.

(f) Initially validate the method by using the available patients data from the completed pilot study.

4. **Dissertation document writing and presentation**

(a) Write first draft and submit for the review.

(b) Correct and submit the dissertation document to the committee.

(c) Defend dissertation.

Figure 9.1 shows the Gantt chart for the dissertation research. Table 9.1 outlines the completion percentage and schedule for each section.

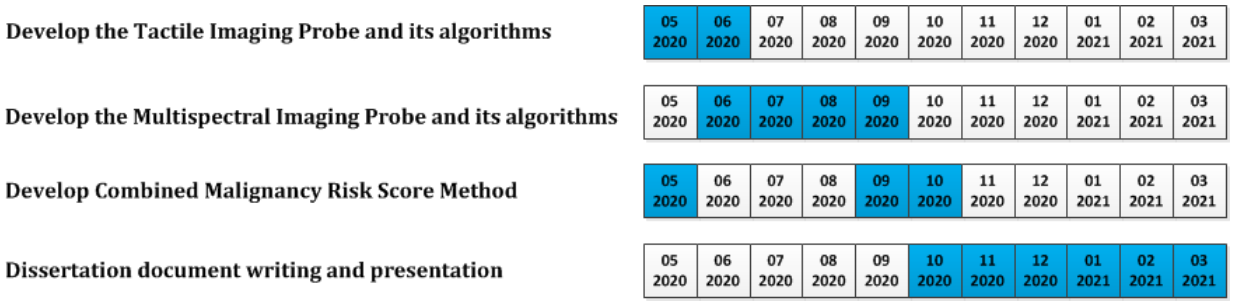

Figure 9.1: Dissertation research Gantt chart

Table 9.1: Dissertation completion schedule

Task	Start Date	End Date	Completed
Develop the Tactile Imaging Probe and its algorithms			
Complete simulations for the Tactile Imaging Probe's sensing element			100%
Build a Tactile Imaging Probe prototype			100%
Develop algorithms for tumor size and stiffness estimation			100%
Suggest a method to represent tactile information from TIP data as TPD			100%
Propose a method to estimate tumor depth from TPDs using CNN			100%
Propose a method to estimate tumor size and stiffness from TPDs using CNN			100%
Develop a breast tissue and tumors mimicking phantom			100%
Complete phantom validation experiments			100%
Employ the algorithms on the phantom data, analyze the results	05/11/20	05/22/20	75%
Complete a pilot in-vivo study and analyze the results	05/25/20	06/05/20	90%
Develop the Multispectral Imaging Probe and its algorithms			
Complete a literature review on the superficial breast tissue features attributed to cancer diagnosis and imaging	06/01/20	06/05/20	90%
Develop the sensing principle and build the Multispectral Imaging Probe	06/08/20	06/12/20	95%
Suggest a method to represent superficial breast tissue information as MPDs			100%
Develop technique to characterize breast tissue color, texture, size of the affected region, and the extend of bilateral asymmetry	06/01/20	06/19/20	50%
Develop optical properties tissue phantom as a part of the bimodal imaging phantom	06/08/20	08/07/20	15%
Complete phantom validation experiments	06/29/20	08/14/20	0%
Employ the algorithms on the phantom data, analyze the results	08/17/20	09/18/20	0%
Develop Combined Malignancy Risk Score Method			
Complete a literature review on the risk score calculation for cancer patients	05/11/20	05/22/20	75%
Propose the method to calculate a malignancy index from TIP modality	09/21/20	10/02/20	80%
Propose the method to calculate a malignancy index from MIP modality	09/14/20	10/02/20	70%
Propose the method to include the individual malignancy risk assessment into the calculation	09/28/20	10/02/20	95%
Develop the method of Combined Malignancy Risk Score calculation with the appropriate weights for the indexes	09/28/20	10/09/20	50%
Initially validate the method by using the available patients data from the pilot study	10/05/20	10/23/20	0%
Dissertation Document Writing and Presentation			
Write first draft and submit for the review	10/12/20	02/26/21	25%
Correct and submit the dissertation document to the committee	02/08/21	03/12/21	0%
Defend dissertation	03/08/21	03/19/21	0%

REFERENCES

(2006). Inflammatory breast cancer questions and answers. Fact sheet. https://www.cancer.gov/types/breast/ibc-fact-sheet{#}what-are-the-symptoms-of-inflammatory-breast-cancer.

American Cancer Society. Risk Factors for Breast Cancer. https://www.cancer.org/cancer/breast-cancer/risk-and-prevention.html.

Aydiner, A., Igci, A., and Soran, A. (2017). *Breast Disease. Diagnosis and Pathology*, volume 1. Springer.

Bicchi, A., Buss, M., Ernst, M. O., and Peer, A. (2008). *The sense of touch and its rendering. Progress in Haptics Research*. Springer Tracts in Advanced Robotics. Springer Berlin Heidelberg.

Boehm, T., Hochmuth, A., Malich, A., Reichenbach, J. R., Fleck, M., and Kaiser, W. A. (2001). Contrast-enhanced near-infrared laser mammography Contrast-Enhanced Near-Infrared Laser Mammography with a prototype breast scanner: Feasibility study with tissue phantoms and preliminary results of imaging experimental tumors. *Investigative Radiology*, 36(10):573–581.

Boisserie-Lacroix, M., Debled, M., Tunon De Lara, C., Hurtevent, G., Asad-Syed, M., and Ferron, S. (2012). The inflammatory breast: Management, decision-making algorithms, therapeutic principles. *Diagnostic and Interventional Imaging*, 93(2):126–136.

Calin, M. A., Parasca, S. V., Savastru, D., and Manea, D. (2014). Hyperspectral Imaging in the Medical Field: Present and Future. *Applied Spectroscopy Reviews*, 49(6):435–447.

Canny, J. (1986). A Computational Approach to Edge Detection. *IEEE Transactions on Pattern Analysis and Machine Intelligence*, PAMI-8(6):679–698.

Center for Plasticity of the Brain (2016). How Your Sense of Touch Works. https://www.plasticitybraincenters.com/media/how-your-sense-of-touch-works/. Retrieved on 09/24/2018.

Chen, A. I., Balter, M. L., Chen, M. I., Gross, D., Alam, S. K., Maguire, T. J., and Yarmush, M. L. (2016). Multilayered tissue mimicking skin and vessel phantoms with tunable mechanical, optical, and acoustic properties. *Med. Phys.*, 43(6):3117–3131.

Choe, R. (2005). *Diffuse optical tomography and spectroscopy of breast cancer and fetal brain*. Dissertation, University of Pennsylvania.

Claus, E. B., Risch, N., and Thompson, W. D. (1994). Autosomal dominant inheritance of early-onset breast cancer. Implications for risk prediction. *Cancer*, 73(3):641–651.

Clevert, D. A., Unterthiner, T., and Hochreiter, S. (2016). Fast and accurate deep network learning by exponential linear units (ELUs). *4th International Conference on Learning Representations, ICLR 2016 - Conference Track Proceedings*, pages 1–14.

Costantino, J. P., Gail, M. H., Pee, D., Anderson, S., Redmond, C. K., Benichou, J., and Wieand, H. S. (1999). Validation studies for models projecting the risk of invasive and total breast cancer incidence. *Journal of the National Cancer Institute*, 91(18):1541–1548.

Egorov, V., Kearney, T., Pollak, S. B., Rohatgi, C., Sarvazyan, N., Airapetian, S., Browning, S., and Sarvazyan, A. (2009). Differentiation of benign and malignant breast lesions by mechanical imaging. *Breast Cancer Research and Treatment*, 118(1):67–80.

Egorov, V. and Sarvazyan, A. P. (2008). Mechanical imaging of the breast. *IEEE Transactions on Medical Imaging*, 27(9):1275–1287.

Fiaschetti, G., Browne, J. E., Cavagnaro, M., Farina, L., and Ruvio, G. (2018). Tissue Mimicking Materials for Multi-Modality Breast Phantoms. *2018 2nd URSI Atlantic Radio Science Meeting, AT-RASC 2018*, (June).

Fukushima, K. (1980). Neocognitron: A self-organizing neural network model for a mechanism of pattern recognition unaffected by shift in position. *Biological Cybernetics*, 36(4):193–202.

Fulop, S. A. (2011). *Speech Spectrum Analysis*. Springer.

Gail, M. H., Brinton, L. A., Byar, D. P., Corle, D. K., Green, S. B., Schairer, C., and Mulvihill, J. J. (1989). Projecting individualized probabilities of developing breast cancer for white females who are being examined annually. *Journal of the National Cancer Institute*, 81(24):1879–1886.

Garg, P. (2014). Inflammatory breast cancer: a clinical diagnosis. *Singapore Medical Journal*, 55(03).

Garza-Salazar, J., Meneses-Garcia, A., and Arce-Salinas, C. (2013). *Inflammatory Breast Cancer*.

Giller, C. A., Liu, H., Gurnani, P., Victor, S., Yazdani, U., and German, D. C. (2003). Validation of a near-infrared probe for detection of thin intracranial white matter structures. *Journal of Neurosurgery*, 98(6):1299–1306.

Godavarty, A., Rodriguez, S., Jung, Y.-J., and Gonzalez, S. (2015). Optical imaging for breast cancer prescreening. *Breast cancer (Dove Medical Press)*, 7:193–209.

Gonzalez, R. and Woods, R. (2008). *Digital Image Processing. Upper Saddle River, N.J: Prentice Hall; 2002*. Pearson/Prentice Hall, third edition.

Goodfellow, I., Bengio, Y., and Courville, A. (2017). *Deep Learning*. MIT Press, Cambridge, Mass.

GP (2015). Education: Clinical review - Benign breast disease. (2015). GP, 35. https://link-gale-com.libproxy.temple.edu/apps/doc/A404439611/AONE?u=temple_main&sid=AONE&xid=6d53e597.

Grand, A. M. D., Lomnes, S. J., Lee, D. S., Pietrzykowski, M., Ohnishi, S., Morgan, T. G., Gogbashian, A., Laurence, R. G., and Frangioni, J. V. (2008). Tissue-Like Phantoms for Near-Infrared Fluorescence Imaging System Assessment and the Training of Surgeons. *J Biomed Opt*, 11(1):1–21.

Gulli, A. and Pal, S. (2017). *Deep Learning with Keras*. Packt Publishing, Birmingham.

Harris, J. R., Pine, Jonathan W., J., Goolsby, J., Moyer, E., Dougherty, B., and Mallon, T. (2014). *Diseases of the Breast*. Wolters Kluwer, Philadelphia, Pennsylvania, 5th edition.

Harvard Medical School (2010). Radiation risk from medical imaging. https://www.health.harvard.edu/cancer/radiation-risk-from-medical-imaging. Retrieved on 2020-03-30.

Hatami, N., Gavet, Y., and Debayle, J. (2017). Classification of Time-Series Images Using Deep Convolutional Neural Networks. In *The 10th International Conference on Machine Vision (ICMV 2017)*.

Hatami, N., Gavet, Y., and Debayle, J. (2018). Bag of recurrence patterns representation for time-series classification. *Pattern Analysis and Applications*, pages 1–11.

Hebden, J. C., Price, B. D., Gibson, A. P., and Royle, G. (2006). A soft deformable tissue-equivalent phantom for diffuse optical tomography. *Physics in Medicine and Biology*, 51(21):5581–5590.

Heinemann, F., Birk, G., and Stierstorfer, B. (2019). Deep learning enables pathologist-like scoring of NASH models. *Scientific Reports*, 9(1):1–10.

Hellawell, J. (2008). Breast Diseases.

Howard, D. M. and Murphy, D. T. (2007). *Voice science, acoustics and recording*. Plural Publishing, Inc., San Diego, California.

IDS Imaging Development Systems GmbH (2015). UI3240CP_NIR Datasheet. https://www.1stvision.com/cameras/IDS/dataman/UI3240CP-NIR-Datasheet.pdf. Retreived on 04/15/2020.

Imani, F., Daoud, M., Moradi, M., Abolmaesumi, P., and Mousavi, P. (2011). Tissue classification using depth-dependent ultrasound time series analysis: in-vitro animal study. *SPIE Medical Imaging*, 7968.

Jacques, S. L. (2013). Optical properties of biological tissues: a review. *Physics in Medicine and Biology*, 58(11):R37–R61.

Jiao, Z., Gao, X., Wang, Y., and Li, J. (2016). A deep feature based framework for breast masses classification. http://dx.doi.org/10.1016/j.neucom.2016.02.060.

Kallenberg, M., Petersen, K., Nielsen, M., Ng, A. Y., Diao, P., Igel, C., Vachon, C. M., Holland, K., Winkel, R. R., Karssemeijer, N., and Lillholm, M. (2016). Unsupervised Deep Learning Applied to Breast Density Segmentation and Mammographic Risk Scoring. *IEEE Transactions on Medical Imaging*, 35(5):1322–1331.

Kingma, D. P. and Ba, J. L. (2015). Adam: A method for stochastic optimization. *3rd International Conference on Learning Representations, ICLR 2015 - Conference Track Proceedings*, pages 1–15.

Krouskop, T., Wheeler, T., Kallel, F., Garra, B., and Hall, T. (1998). Elastic Moduli of Breast and Prostate Tissues Under Compression. *Ultrasonic Imaging*, 20(4):260–274.

Lamouche, G., Kennedy, B. F., Kennedy, K. M., Bisaillon, C.-E., Curatolo, A., Campbell, G., Pazos, V., and Sampson, D. D. (2012). Review of tissue simulating phantoms with controllable optical, mechanical and structural properties for use in optical coherence tomography. *Biomedical Optics Express*, 3(6):1381.

Lecun, Y. (1989). Generalization and network design strategies. Technical Report CRG-TR-89-4. Technical report, University of Toronto, Toronto.

Lee, J.-H. and Won, C. H. (2011). High Resolution Tactile Imaging Sensor using Total Internal Reflection and Non-Rigid Pattern Matching. *IEEE SENSORS JOURNAL*, 11(9):2084 – 2093.

Lee, J.-H. and Won, C.-H. (2013). The tactile sensation imaging system for embedded lesion characterization. *IEEE Journal of Biomedical and Health Informatics*, 17(2):452–458.

Lenat, D. B. and Guha, R. V. (1989). *Building Large knowledge-based systems; representation and inference in the Cyc project*. Addison-Wesley Longman Publishing Co., Inc.

Lu, G. and Fei, B. (2014). Medical hyperspectral imaging: a review. *Journal of biomedical optics*, 19(1):10901.

Mangano, E. (2014). Preloading, and How It Affects Your Mechanical Test. `https://www.instron.us/en-us/our-company/press-room/blog/2014/august/preloading-and-how-it-affects-your-mechanical-test`. Retreived on 07/18/2019.

MATLAB MathWorks (2019). Image Processing Toolbox Documentation. `https://www.mathworks.com/help/images/index.html?s{_}tid=CRUX{_}lftnav`. Retrieved on 13/06/2019.

Ming, C., Viassolo, V., Probst-Hensch, N., Chappuis, P. O., Dinov, I. D., and Katapodi, M. C. (2019). Machine learning techniques for personalized breast cancer risk prediction: Comparison with the BCRAT and BOADICEA models. *Breast Cancer Research*, 21(1):1–11.

Miranda, D. A., Cristiano, K. L., and Gutiérrez, J. C. (2013). Breast phantom for mammary tissue characterization by near infrared spectroscopy. *Journal of Physics: Conference Series*, 466(1):3–6.

Modersitzki, J. (2004). *Numerical Methods for Image Registration*. Oxford University Press, New York.

Moser, W. (2016). *Third generation tactile imaging system with new interface, calibration method and wear indication*. Ms thesis, Temple University.

Mourant, J. R., Fuselier, T., Boyer, J., Johnson, T. M., and Bigio, I. J. (1997). Predictions and measurements of scattering and absorption over broad wavelength ranges in tissue phantoms. *Applied Optics*, 36(4):949.

National Cancer Institute (1999). The Breast Cancer Risk Assessment Tool. `https://bcrisktool.cancer.gov/index.html`. Retreived on 04/15/2020.

Nioka, S. and Chance, B. (2005). NIR spectroscopic detection of breast cancer. *Technology in Cancer Research and Treatment*, 4(5):497–512.

Oleksyuk, V. (2019). Young's Modulus Estimation of PDMS Samples using Instron Material Testing Machine. Technical report, Temple University, Philadelphia PA :. Technical Report.

Oleksyuk, V., Rajan, R., Saleheen, F., Caroline, D., Pascarella, S., and Won, C. (2018). Risk Score Based Pre-screening of Breast Tumor Using Compression Induced Sensing System. *IEEE Sensors Journal*, 18(10):4038–4045.

Oleksyuk, V., Saleheen, F., Chen, Y., and Won, C. H. (2015). Tactile Imaging System for inclusion size and stiffness characterization. *2015 IEEE Signal Processing in Medicine and Biology Symposium - Proceedings*, pages 1–6.

Patel, K. (2019). MNIST Handwritten Digits Classi cation using a Convolutional Neural Network (CNN). `https://towardsdatascience.com/mnist-handwritten-digits-classification-using-a-convolutional-neural\-network-cnn-af5fafbc35e9`. Retrieved on 04/10/20.

Price, B. D., Gibson, a. P., Tan, L. T., and Royle, G. J. (2010). An elastically compressible phantom material with mechanical and x-ray attenuation properties equivalent to breast tissue. *Physics in medicine and biology*, 55(4):1177–1188.

QImaging (2014). Retiga EXi Camera Datasheet. `https://meyerinst.com/library/uploads/RetigaEXi{_}fast1394.pdf`. Retreived on 04/15/2020.

Qin, J., Chao, K., Kim, M. S., Lu, R., and Burks, T. F. (2013). Hyperspectral and multispectral imaging for evaluating food safety and quality. *Journal of Food Engineering*, 118(2):157–171.

Ricci, P., Maggini, E., Mancuso, E., Lodise, P., Cantisani, V., and Catalano, C. (2014). Clinical application of breast elastography: State of the art. *European Journal of Radiology*, 83(3):429–437.

Riley, M. D. (1989). *Speech Time-Frequency Representations*. Kluwer Academic Publisher, Boston.

Robertson, F. M., Bondy, M., Yang, W., Yamauchi, H., Wiggins, S., Kamrudin, S., Krishnamurthy, S., LeâĂŘPetross, H., Bidaut, L., Player, A. N., Barsky, S. H., Woodward, W. A., Buchholz, T., Lucci, A., Ueno, N. T., and Cristofanilli, M. (2010). Inflammatory Breast Cancer. *CA Cancer J Clin*, 60(6):351–375.

Sahu, A., Saleheen, F., Oleksyuk, V., McGoverin, C., Pleshko, N., Hossein Harati Nejad Torbati, A., Picone, J., Member, S., Sorenmo, K., and Won, C.-H. (2014). Characterization of Mammary Tumors Using Noninvasive Tactile and Hyperspectral Sensors. *IEEE SENSORS JOURNAL*, 14(10):3337 – 3344.

Sallaway, L., Magee, S., Shi, J., Lehmann, O., Quivira, F., Tgavalekos, K., Brooks, D. H., Muftu, S., Meleis, W., Moore, R. H., Kopans, D., and Wan, K. T. (2014). Detecting Solid Masses in Phantom Breast Using Mechanical Indentation. *Experimental Mechanics*, 54(6):935–942.

Smith, J. (2007). *Mathematics of the Discrete Fourier Transform (DFT) with Audio Applications*. W3K Publishing, second edition.

Spirou, G. M., Oraevsky, A. A., Alex Vitkin, I., and Whelan, W. M. (2005). Optical and acoustic properties at 1064 nm of polyvinyl chloride-plastisol for use as a tissue phantom in biomedical optoacoustics. *Physics in Medicine and Biology*, 50(14).

Tyrer, J., Duffy, S., and Cuzick, J. (2004). A breast cancer prediction model incorporating familial and personal risk factors. *Stat Med*, 23(7):1111–1130.

Uniyal, N., Eskandari, H., Abolmaesumi, P., Sojoudi, S., Gordon, P., Warren, L., Rohling, R., Salcudean, S., and Moradi, M. (2014). Ultrasound RF time series for classification of breast lesions. *IEEE transactions on medical imaging*, 34(2):652–661.

Walters, G. A. (2019). Max-pooling. `https://austingwalters.com/convolutional-neural-networks-cnn-to-classify-sentences/max-pooling/`. Retreived on 2020-12-04.

Wang, Z. and Oates, T. (2015). Imaging time-series to improve classification and imputation. *IJCAI International Joint Conference on Artificial Intelligence*, 2015-Janua:3939–3945.

Wellman, P., Dalton, E., and Krag, D. (2001). Tactile Imaging of Breast Masses. *Archives of Surgery*, 136(2):204–208.

Yadav, S., Hartkop, S., Cardenas, P. Y., Ladkany, R., Halalau, A., Shoichet, S., Maddens, M., and Zakalik, D. (2019). Utilization of a breast cancer risk assessment tool by internal medicine residents in a primary care clinic: Impact of an educational program. *BMC Cancer*, 19(1):1–7.

Yin-Kwee Ng, E. (2011). Breast imaging: A survey. *World J Clini Oncol*, 2(4):171–178. https://www.ncbi.nlm.nih.gov/pmc/articles/PMC3100484/pdf/WJCO-2-171.pdf.

Zhou, Y. T. and Chellappa, R. (1988). Computation of optical flow using a neural network. *IEEE 1988 International Conference on Neural Networks*, pages 71–78 vol.2.